ORDERED POROUS CARBON SUPPORTED NANO-PLATINUM ELECTROCATALYST FOR DIRECT METHANOL FUEL CELL APPLICATIONS

A project report

submitted in partial fulfilment of the requirements

for the award of the degree of

MASTER OF TECHNOLOGY

in

CHEMICAL ENGINEERING

SPECIALISATION : CATALYSIS TECHNOLOGY

by

K. DEVAKI

(CH09M001)

Under the guidance of
PROF. P. SELVAM

DEPARTMENT OF CHEMICAL ENGINEERING

INDIAN INSTITUTE OF TECHNOLOGY-MADRAS

CHENNAI 600 036

MAY 2011

I

CERTIFICATE

This is to certify that the project report entitled **"Ordered Porous Carbon Supported Nano-Platinum Electrocatalyst for Direct Methanol Fuel Cell Applications"** submitted by **Ms. K. DEVAKI (CH09M001)** to the Indian Institute of Technology-Madras for the award of the degree of Master of technology in Catalysis Technology (Chemical Engineering) is a *bona-fide* record of the work carried out by her under my supervision. The contents of the thesis, in full or parts have not been submitted to any other institute or university for the awards of any degree.

Guide
PROF. P. SELVAM
National Centre for Catalysis Research
IIT Madras.

Co Guide
DR. PREETI AGHALAYAM
Department of Chemical Engineering
IIT Madras

Place: Chennai

Date :

ACKNOWLEDGEMENTS

K. Devaki

ABSTRACT

KEYWORDS: Carbon materials, Microporous carbons, Nanocasting, Electro catalysts, Methanol oxidation, Fuel cell, DMFC

Fuel cells are considered as the future energy conversion device for wide variety of applications. Fuel cells can power almost any portable device or machine that uses batteries. Unlike a typical battery, which eventually goes dead, a fuel cell continues to produce energy as long as fuel and oxidant are supplied. Laptop, computers, cellular phones, video recorders, and hearing aids could be powered by portable fuel cells. Fuel cells have strong benefits over conventional combustion-based technologies currently used in many power plants and cars. They produce much smaller quantities of greenhouse gases and none of the air pollutants that create smog and cause health problems. If pure hydrogen is used as a fuel, fuel cells emit only heat and water as a byproduct. Hydrogen-powered fuel cells are also far more energy efficient than traditional combustion technologies.

Among the different types of fuel cells, the PEM (Polymer electrolyte membrane) fuel cells employing hydrogen as the fuel and the DMFC (Direct methanol fuel cell) employing methanol as the fuel are under development for successful commercialization. The commercialization of fuel cells is delayed mainly because of the high cost of the catalyst layer which needs expensive noble metal such as platinum and its alloys. The sluggish kinetics of oxygen reduction reaction in H_2 based PEMFC and both oxygen reduction and methanol oxidation reactions in DMFC, have caused concern. Even a slight enhancement in the activity and durability of these catalysts can bring down the cost significantly. The typical catalyst mostly used in fuel cell electrodes is Pt dispersed on carbon black support, for both anode and cathode electrodes.

Hydrogen is the most potential and promising fuel due to its high energy density and the maximum attainable voltage (E^o_{max} =1.15 V), which is closer to the theoretical value (E^o_{theor} = 1.23 V). But hydrogen fuel cell encounters challenges of hydrogen production, storage and transportation, whereas DMFC uses a liquid methanol as a fuel, which can be easily stored, handled and transported.

Carbon materials are the most widely used support for fuel cell electro catalyst due to its various properties. These properties include corrosion resistance, anisotropic electronic property, formation of intercalation compounds, strong covalent bond formation with variety of surface modifiers and adsorbing capacity of wide variety of materials.

The nature of the carbon determines the electrochemical performance of electrode catalysts. Interactions between the noble metal and the support may increase the catalyst performance. Carbon black, Vulcan XC-72 is the most common support material for fuel cell electro catalyst. But nowadays various carbon materials have been investigated as electro-catalyst support like carbon nanofibers, carbon nanotubes, carbon aerogels and ordered nanoporous carbon (micro and mesoporous carbon).

Micro porous carbons, having very high surface area are of great technological interest for the development of catalytic, electro catalytic and hydrogen storage systems. Ordered microporous carbons have been prepared by nanocasting method. i.e., CNI-1 and NCNI-1 have been synthesized by carbonization of furfuryl alcohol and pyrrole respectively within the pores of mordenite. The inorganic templates were then removed by HF treatment, followed by filtration, washing and drying to obtain the microporous carbons. All the carbon samples were systematically characterized by various analytical and spectroscopic techniques including, XRD, XPS, SEM and N_2 sorption measurements. Subsequently, 10 and 20 wt % Pt were loaded on the microporous carbons using $H_2PtCl_6.6H_2O$ acid. The prepared platinum catalysts were systematically characterized by XRD, XPS and TEM.

The prepared catalysts were evaluated for their catalytic activity for methanol electro oxidation reaction. Electrochemical oxidation of methanol over the microporous carbon supported platinum catalysts was studied by cyclic voltammetry at room temperature. The electrochemical measurements performed using 1 M H_2SO_4 + 1 M CH_3OH indicate that the prepared catalysts exhibit excellent electrochemical activity as well as better CO tolerance compare to commercial Pt catalyst. The stability of the catalysts was studied by chronoamperometry (CA) measurement. Prepared microporous carbon supported Pt catalysts showed better stability compare to commercial Pt catalyst. It is therefore, concluded that platinum supported on ordered microporous carbon catalysts are promising electrode materials for methanol fuel cell applications.

TABLE OF CONTENTS

Table of Contents (Contd.)   **Page No.**

CHAPTER 4   **ORDERED MICROPOROUS CARBONS (CNI-1 and NCNI-1)**

CHAPTER 5   **CNI-1 and NCNI-1 SUPPROTED PLATINUM AS**

                    ELECTRODES FOR DMFC APPLICATIONS

LIST OF FIGURES

LIST OF TABLES

ABBREVIATIONS

Au-Gold

Pd-Palladium

Pt-Platinum

Ru-Ruthenium

Bi-Bismuth

CV- Cyclic Voltammetry

CA - Chronoamperometry

DMFC-Direct Methanol Fuel Cell

EDX- Energy Dispersive X-ray Analysis

SCE-Standard Calomel Electrode

ORR-Oxygen Reduction Reaction

SEM –Scanning Electron Microscopy

TEM- Transmission Electron Microscopy

XRD- X-ray Diffraction

XPS- X-ray Photoelectron Spectroscopy

EAS- Electrochemical active surface area

MSA-Mass Specific Activity

SA-Specific Activity

EG- Ethylene Glycol

SB-Sodium Borohydride

WI- Wet Impregnation

AC-Activated Carbon

CNT-Carbon Nanotube

ONC-Ordered Microporous Carbon

OMC-Ordered Mesoporous Carbon

CNI-1- ONC from mordenite (template) and furfural alcohol (carbon precursor)

NCNI-1- ONC from mordenite (template) and pyrrole (carbon precursor)

CNI-9- ONC from mordenite (template) and sucrose (carbon precursor)

CNI-2- ONC from NaY (template) and furfural alcohol (carbon precursor)

CNI-8- ONC from NaY (template) and pyrrole (carbon precursor)

NOTATIONS

Å - Angstrom

θ - Angle

λ - Wavelength

h – hour

°C - Degree Celsius

T - Temperature

cm - centimeter

eV - Electron volt

mV - milli volt

mA - milli amphere

E – Potential (V)

I - Current

t - Time

β- Full width at half maximum

CHAPTER 1

INTRODUCTION

1.1 FUEL CELLS

Fuel cells are electrochemical devices that directly convert chemical energy of fuel and oxidant to electrical energy by the redox process with a high efficiency and zero emission. They consist of an anode, cathode, electrolyte, gas-diffusion layer and bipolar plates (Fig. 1.1). An anode facilitates the oxidation of the fuel, while a cathode promotes the reduction of oxidant. The electrodes should be both catalytically active and conductive in nature. The electrodes are used to provide the active sites, physical barrier which separates the bulk gas phase and the electrolyte and also to facilitate the ion transport away from or into the three-phase interface. The electrolyte also acts as a physical barrier between the fuel and oxidant.

Fuel cells are mainly classified based on electrolyte. The choice of the electrolyte medium decides the operating temperature of the fuel cell (Viswanathan and Scibioh, 2006; Ramani, 2006). The porous gas diffusion layers (GDLs) provide structural support for the electrodes and diffusion path through which the oxidant or fuel gases can reach the catalyst. GDLs are made of carbon paper or woven carbon cloth. Bipolar plates can be coated with dispersed carbon to provide corrosion resistance and good electrical conductivity. The bipolar plates used for the distribution of fuel and oxidant; heat and water management; separate the individual cells in the stack and to humidify the gases and also as a current collector (Dicks, 2006).

Fuel cells can be classified based on fuel (direct or indirect fuel), oxidant, electrolyte and temperature. The details are given in Table 1.1.
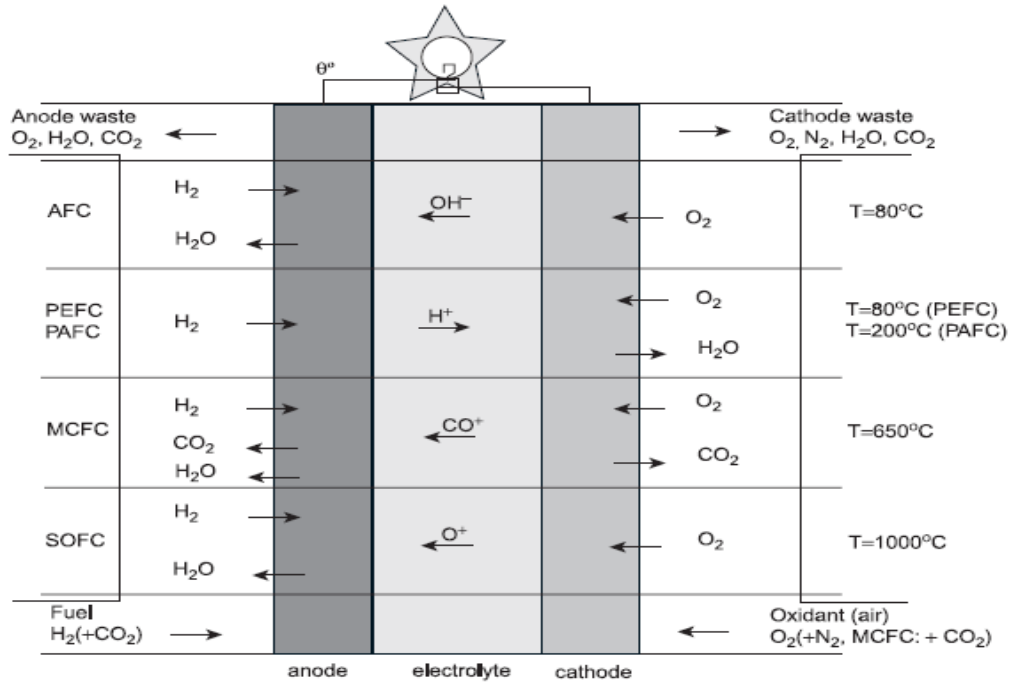
Figure 1.1: Schematic representation of a Fuel Cell (Viswanathan and Scibioh, 2006).

Table 1.1: Classification of Fuel cell.

Fuel		Oxidant	Electrolyte	Temperature
Direct	**Indirect**	**Oxidant**	**Electrolyte**	**Temperature**
Hydrogen	Methanol	Oxygen (pure)		Low (RT - 120°C)
			Solid polymer	Intermediate
Methanol	Ethanol	Air (oxygen)	electrolyte	(120 - 250 °C)
Ammonia	Hydrocarbon	H_2O_2	Aq. sulfuric acid	High (250 - 750 °C)
Hydrazine	Ammonia		Aq. phosphoric acid	Very high (> 750°C)
Formic acid	Hydride		Aq. KOH	
Ethanol	Coal		Aq. K_2CO_3	
Coal gas			Molten carbonate	
Coal			(Li_2CO_3-Na_2CO_3)	
			Solid oxide	
			(Yttrium-stabilized	
			Zirconia)	

The choice of the fuel depends on their chemical and catalytic activity. Table 1.2 shows the list of fuels that can be used in fuel cells.

Table 1.2: Chemical and electrochemical data of various fuels (Viswanathan and Scibioh, 2006).

Fuel	$-\Delta G^{\circ}$ (kcal/mol)	E°_{theor} (V)	E°_{max} (V)	Energy density (kWh/kg)
Hydrogen	56.69	1.23	1.15	32.67
Methanol	166.80	1.21	0.98	6.13
Ammonia	80.80	1.17	0.62	5.52
Hydrazine	143.90	1.56	1.28	5.22
Formaldehyde	124.70	1.35	1.15	4.82
Carbon monoxide	61.60	1.33	1.22	2.04
Formic acid	68.20	1.48	1.14	1.72
Methane	195.50	1.06	0.58	-
Propane	503.20	1.08	0.65	-

From the above table one can conclude that, hydrogen is the most potential and promising fuel due to its high energy density and the maximum attainable voltage which is closer to the theoretical value. But hydrogen fuel cell encounters challenges of hydrogen production, storage and transportation, whereas DMFC uses a liquid methanol as a fuel, which can be easily stored, handled and transported.

1.2 DIRECT METHANOL FUEL CELL (DMFC)

DMFC (Fig. 1.2) is considered as a promising candidate for clean and portable power sources, transportation applications and electric vehicles. Methanol is a liquid fuel, so it can be easily handled and stored. And also it is having high heating value and solubility in aqueous electrolytes. However, various limitations such as sluggish anode kinetics (six electron transfer process), methanol crossover (causes mixed potential at the cathode), high loading of noble metals, carbon monoxide poisoning, carbon dioxide removal at an anode are remain as major problems for commercialization of DMFC.
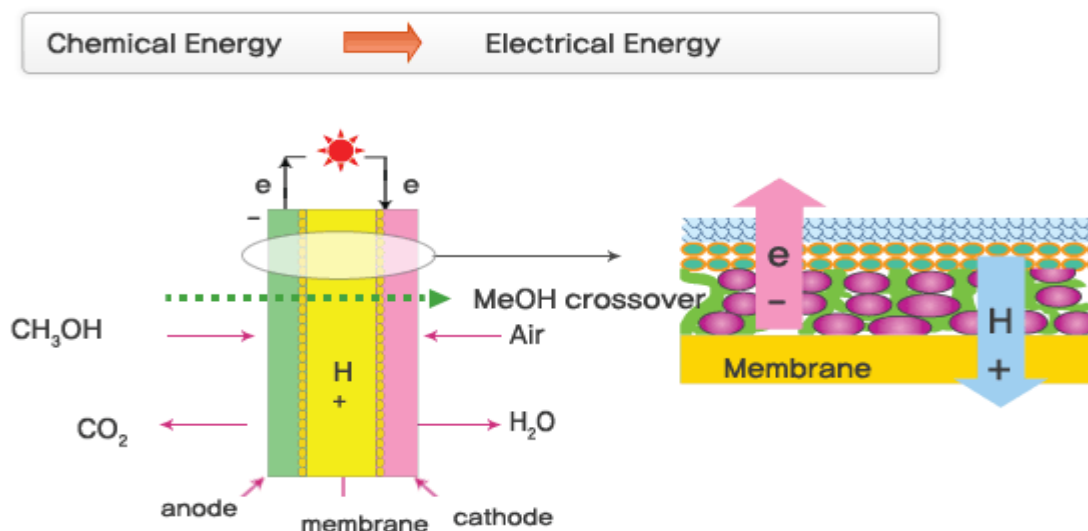
Figure 1.2: Schematic representation of a Direct Methanol Fuel Cell.

In the case of conventional platinum (Pt) catalyst, the adsorption of CO, one of the intermediates in methanol oxidation, block the active sites, resulting in prevention of further methanol adsorption. To reduce CO poisoning effect, CO tolerant electrocatalysts have been examined. In nano scale, gold (Au) is the active catalyst for CO oxidation at lower temperature. Au facilitates the removal of CO, thus poisoned sites can be regenerated by the presence of Au. On the other hand, various Pt-based alloys (bimetallics) such as Pt-Ru, Pt-Os, Pt-Sn, Pt-W, Pt-Mo, etc., have been examined. Since methanol oxidation is a demanding reaction, the atomic radii between two metals should be in a proper orientation, so that it will facilitate the CO oxidation reaction. And also second metal should be oxophilic in nature, so that it can provide active form of oxygen in order to oxidize the poisonous CO.

Ruthenium (Ru) has been the best metal to validate the above points. And also Ru will form an oxygenated species at lower potential compare to Pt. Therefore PtRu is the state-of-the-art anode catalyst. The increased activity of PtRu for methanol oxidation can be due to bi-functional mechanism (Pt promotes the dissociative chemisorption of methanol whereas ruthenium forms a surface oxy-hydroxide which is used to oxidizes the CO to CO_2) or by a ligand effect, the second metal modifies the electronic properties of the Pt in a such way, so that weakening the chemical bond between platinum and the surface intermediates is facile, (Hamnett, 1997). The catalytic

activity of the PtRu electrocatalyst depends on the composition, structure, morphology, particle size, particle size distribution, oxidation state of Pt and Ru and alloyed degree (Liu et al., 2006).

The maximum utilization, dispersion of electrocatalyst can be obtained by choosing the proper supporting material. The role of supporting material includes achieving high surface area, high dispersion, improved activity and stability. It also prevents the agglomeration of metal nanoparticles and decreases the mass transfer limitations. The ideal support material should have some specific characteristic like wide electrochemical potential window (Electrochemical properties), good corrosion resistance (Chemical properties), and high electrical conductivity (Electrical properties) and mechanical stability (Salgado et al., 2010).

Pt and Au are in cubic structure, whereas Ru has hexagonal structure. Platinum is most widely used as an anode because of its ability to remove the CO poisonous species at + 0.7 V, whereas Ru is able to remove CO poisonous species at a lower potential (less than + 0.7 V) by ligand effect. Therefore Pt-Ru bimetallic is the best electrocatalyst for the oxidation of methanol.

CHAPTER 2

LITERATURE SURVEY

2.1 ELECTROCATALYSTS FOR METHANOL OXIDATION

The common criteria for a high performance electrocatalysts are:

(i)   narrow nanoscale size distribution

(ii) uniform composition throughout the nanoparticles

(iii) fully alloyed degree

(iv) high dispersion on carbon support.

Salgado et al. (2010) reported the synthesis of Pt-Ru electrocatalysts supported on ordered mesoporous carbon (CMK-3) for DMFC by formic acid method. Methanol and carbon monoxide oxidation were studied by cyclic voltammetry, and current-time curves were reordered in a methanol solution to establish the activity under potentiostatic conditions. At 0.6 V, Pt-Ru/CMK-3 showed highest current density in both CV (223 $\mu A/cm^2$) and chronoamperometric (102 $\mu A/cm^2$) tests compare to Pt-Ru/ Vulcan (CV: 134 $\mu A/cm^2$ and CR: 91 $\mu A/cm^2$) and Pt-Ru/ C (E) (CV: 48 $\mu A/cm^2$ and CR: 74 $\mu A/cm^2$). This results show the effect of mesoporous carbon support. From these results, they have concluded that bimetallic Pt-Ru supported on ordered mesoporous is the most suitable electrocatalyst for methanol oxidation.

Guo et al. (2006) reported the synthesis of ceria (CeO_2) modified PtRu supported on carbon (Vulcan XC72) catalysts with different compositions of Ru and CeO_2 {$PtRu_{0.9}$ $(CeO_2)_{0.1}$/C, $PtRu_{0.7}(CeO_2)_{0.3}$/C, $PtRu_{0.5}(CeO_2)_{0.5}$/C and unmodified PtRu/C}by the sodium borohydride reduction method. They employed CeO_2 as a co-catalytic material along with Pt-Ru catalyst since CeO_2 has the higher oxygen storage capacity. So the oxygen atoms present in the CeO_2 lattice can be used for promoting bi-functional mechanism of methanol oxidation. They have found that $PtRu_{0.7}(CeO_2)_{0.3}$/C exhibited higher activity for methanol oxidation than the conventional Pt-Ru/C catalyst.

Liu et al. (2003) have reported the synthesis of nanosized Pt and Pt-Ru colloids by a microwave-assisted polyol process. This method involves a rapid microwave synthesis of Pt and Pt-Ru colloids in ethylene glycol followed by the transfer of the colloidal metal particles to toluene using decanethiol as the phase transfer catalyst. The thiol-encapsulated Pt and Pt-Ru colloids are then deposited on carbon and heat treated to produce carbon supported Pt and Pt-Ru catalysts. Due to bifunctional mechanism, binary catalyst was more active than the monometallic Pt and less receptive to methanolic residue deactivation.

Bensebaa et al. (2004) have reported the optimum thermal conditions to prepare the monometallic and alloyed bimetallic nanocatalysts using microwave heating. Alloyed Pt-Ru nanocatalyst have been prepared using microwave heating at a maximum heating temperature of 173 °C in less than 5 minutes. And also they have investigated the effects of preparation parameters to optimize the particles' composition and structure characteristics in the presence of ploy (N-vinyl-2-pyrrolidone) (PVP) and ethylene glycol (EG). In this method, EG was used both as a solvent and reducing agent whereas PVP was used as a protective layer against agglomeration. The resulting catalyst had uniform diameters of 2-3 nm for the PVP-coated samples. In the absence of PVP, agglomerated, inhomogeneous, larger nanocrystals were obtained with a Pt-rich core and a Ru-rich Shell.

Solla-Gullón et al. (2004) have reported electrochemical characterization of Pt-Ru nanoparticles which was prepared by water-in-oil microemulsion method. They have studied electrocatalytic properties of Pt-Ru nanoparticles through Co_{ads} oxidation and methanol oxidation reactions. The highest molar oxidation currents were obtained for $Pt_{80}Ru_{20}$. Pt-Ru nanoparticles with Pt ranging between 40 and 80 % show higher oxidation currents than pure Pt.

Xiong and Manthiram (2005) have synthesized the nanostructured Pt-Ru/C catalysts with different particle sizes by microemulsion method and reported that the samples prepared with water to surfactant molar ratio (W) of 10 attains the maximum mass activity with the least charge transfer resistance and particle size of around 5.3 nm. The better performance of the Pt-Ru/C prepared by microemulsion method can be attributed to a better control of particle size,

crystallinity and microstructure. By optimizing the synthesis and proceeding conditions, the further improvement in the performance of the catalyst can be achieved.

Xue et al. (2005) have reported the synthesis of highly dispersed Pt-Ru/C catalysts by a two-step spray pyrolysis (SP) method. This method is used for the synthesis of particles with controllable size since the properties of final product can be controlled through the precursor choice, solution concentration and operating conditions. In an SP process, the reaction temperature, composition of the carrier gas and the solution properties are the important variables. The catalyst prepared by SP process required 0.39 V to achieve 300 mA/cm², whereas commercial catalyst Pt-Ru/C (E-TEK) required 0.34 V to achieve the same. This result indicates that the electrocatalytic activity of the Pt-Ru/C (SP) catalyst for methanol oxidation is better than that of the Pt-Ru/C (E) catalyst. The high electrocatalytic activity of Pt-Ru/C (SP) can be attributed to the uniform distribution, small average particle size and high alloying degree of the Pt-Ru crystal particles.

Wu and Bo-Qing (2007) synthesized and compared the electrochemical performance of the Pt electrocatalyst supported on multi-walled (MWNT) and single-walled carbon nanotubes (SWNTs). They reported that Pt/SWNT exhibits high CO tolerance due to better supply of OH groups form the SWNT surface and a preferential exposure of Pt (111) plane in the crystal structure. And also for methanol oxidation reaction, it showed higher current density, lower onset potential and lower charge transfer potentials. Li and Xing (2007) have reported the electrochemical properties of PtRu nanoparticles supported on functionalized carbon nanotubes. Three different catalysts, namely $Pt_{53}Ru_{47}$, $Pt_{69}Ru_{31}$ and $Pt_{77}Ru_{23}$ were prepared for the evaluation of compositional effects. Sonochemically functionalized CNTs used for the preparation of highly dispersed PtRu with the size of less than 3.0 nm. From the electrochemical test, they have obtained highest current density and stability for $Pt_{53}Ru_{47}$. Li et al. (2010) have been synthesized PtBi/XC-72 with Pt solid-solution structure using sodium hypophosphite as a reducing agent. In the presence of phosphorus, the Pt-Bi formed an alloy with a Pt fcc solid-solution phase structure, and it showed a better electrocatalytic activity for methanol oxidation. The better electrocatalytic activity can be attributed to the combined effect of bifunctional mechanism and ligand effect.

One of the major challenges in DMFC is the fuel crossover from anode to cathode, causing the depletion of oxygen surface concentration, poisoning of the cathode catalyst and a reduction in fuel efficiency. Therefore, it is necessary to use a methanol tolerant cathode catalyst instead of conventional Pt catalyst. Xia et al. (2006) have synthesized ordered intermetallic $PtBi_2$ nanoparticles for methanol-tolerant catalyst for oxygen reduction reaction by co-reducing H_2PtCl_6 and $Bi(NO_3)_3$ with $NaBH_4$ in the presence of polyvinylpyrrolidone (PVP) as a capping agent. The methanol-tolerant property of $PtBi_2$ nanoparticles can be explained in two ways:

(i) The formation of the $PtBi_2$ phase result in a charge redistribution, which may affect the formation of oxygen-containing species from water dissociation

(ii) Pt-Pt distance in $PtBi_2$ is larger and may not be suitable for the formation of oxygen-containing species.

Luo et al. (2006) have explored the characterization of carbon-supported Au-Pt nanoparticles for electrocatalytic methanol oxidation reaction (Fig. 2.1). The characterization results showed the dependence of the morphology and the surface binding properties of the bimetallic nanoparticles on the temperature. The carbon supported Au-Pt nanoparticles catalysts with 65 % to 85 % Au and treated at 500 °C are shown to exhibit higher electrocatalytic activity in alkaline medium. The bifunctional properties could involve a combination of the following reactions,

$$MeOH + Pt \rightarrow Pt–CO_{ad} + CO_3^- \quad (1)$$
$$Pt–CO_{ad} + Au \rightarrow Au–CO_{ad} + Pt \quad (2)$$
$$Au + OH^- \rightarrow Au–OH_{ad} + e^- \quad (3)$$
$$Pt–CO_{ad} + Au–OH_{ad} \rightarrow CO_3^- + Pt + Au + e^- \quad (4)$$
$$Au–CO_{ad} + Au–OH_{ad} \rightarrow CO_3^- + Au + e^- \quad (5)$$
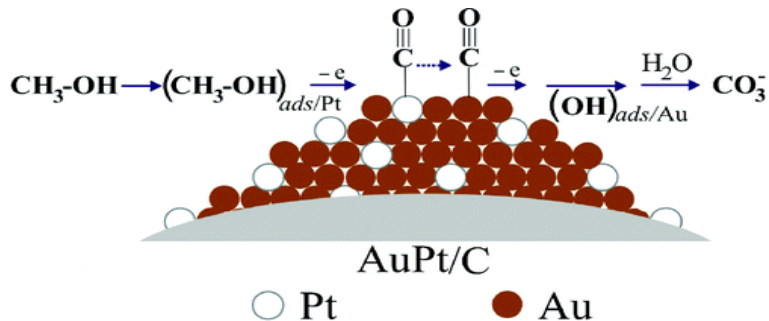
Figure 2.1: Schematic representation of MeOH oxidation by Au-Pt/C (Luo et al., 2006).

2.2 SUPPORT MATERIALS FOR ELECTROCATALYSTS

Carbon materials are the most widely used support for fuel cell electrocatalysts due to its various properties. These properties include corrosion resistance, anisotropic electronic property, formation of intercalation compounds, strong covalent bond formation with variety of surface modifiers and adsorbing capacity of wide variety of materials. The nature of the carbon determines the electrochemical performance of electrode catalysts. Interactions between the noble metal and the support may increase the catalyst performance. Carbon black, Vulcan XC-72 is the most common support material for fuel cell electrocatalysts. But nowadays various carbon materials have been investigated as electrocatalysts support like carbon nanofibers, carbon nanotubes, carbon aerogels and ordered nanoporous carbon (micro and mesoporous carbon).

2.2.1 Carbon Nanotubes (CNT)

CNTs are generally synthesized by template method (Fig. 2.2), carbon- arc discharge, laser ablation of carbon or chemical vapor deposition. Kyotani et al. (1995) successfully prepared carbon nanotubes by template method involving carbon deposition from propylene gas at 800 °C on the inner walls of the nano-sized channels of an anodic aluminum oxide film. Carbon deposition followed by dissociation of the aluminum oxide either by HF at room temperature or by NaOH aqueous solution at 150 °C. The surface functionalization of CNTs before metal deposition was important for achieving optimal interaction between the support and the catalyst precursor. Widely, nitric acid is used to modify the CNTs surface in order to create acid sites on the surface, which can act as a nucleation center for metal ions.
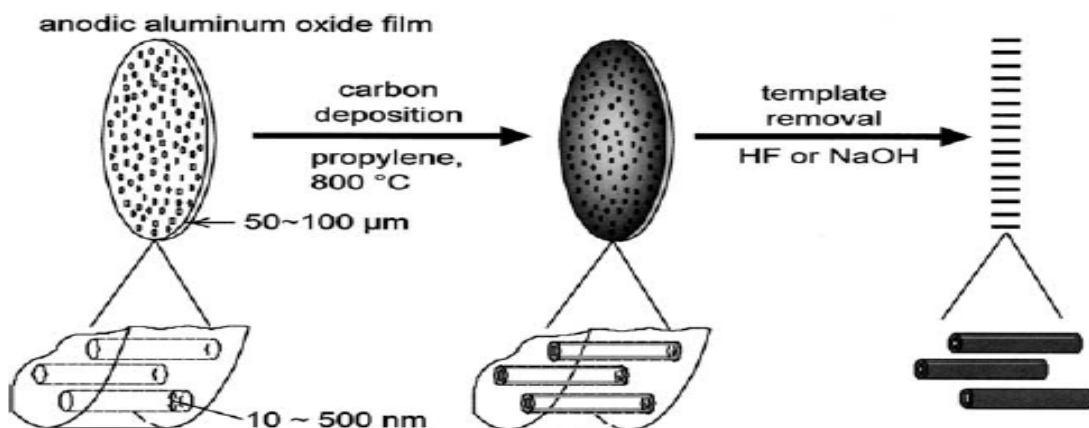
Figure 2.2: Preparation of CNT by a template carbonization technique (Kyotani et al., 1996).

2.2.2 Ordered Porous Carbons

International Union of Pure and Applied Chemistry (IUPAC) classified porous carbon materials based on their pore sizes: microporous < 2 nm, mesoporous 2-50 nm and macroporous > 50 nm. Ordered nanoporous carbons have been synthesized using various templates, including silica nanoparticles, zeolites, and anodic alumina membranes and mesoporous silica materials. The porous carbons are generally synthesized by nanocasting method. The synthesis procedure includes incorporation of the pores of the template with the appropriate carbon precursor, its carbonization and subsequent removal of the template (Lee et al., 2006).

Ordered Nanoporous Carbons (ONC): To synthesize microporous carbon materials with ordered pore structure, rigid inorganic templates are required (Fig. 2.3). Zeolites are highly crystalline aluminosilicate materials which possess uniform and ordered pore structure.
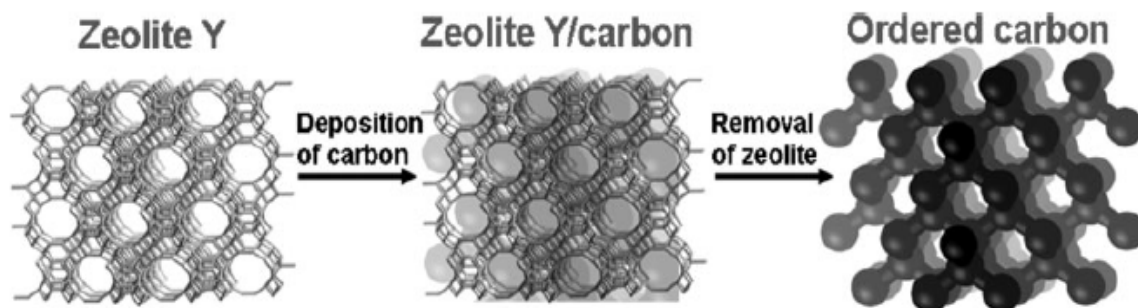
Figure 2.3: Schematic representation of synthesis of carbon from zeolite. (Lee et al., 2006).

Kyotani et al. (1988) have first synthesized highly ordered graphite from ployacrylonitrile (PAN) by a using 2D-space between montmorillonite lamellae. A MONT-PAN intercalation compound was prepared and heat treated at 700 °C to produce carbon from PAN between MONT lamellae. The carbon was then removed by acid treatment and heat treated at different temperature up to 2800 °C. Kyotani et al. (1997) reported the preparation of microporous carbons using zeolite Y as a template and acrylonitrile/ furfural alcohol/propylene as a carbon precursor. The resulting microporous carbons are having BET surface area of over 2000 m²/g. But they have failed to produce an ordered microporous carbon because while removing the template (by HF washing), carbon framework had been collapsed. The resulting carbon structure contained considerable amount of mesopores. In order to avoid the structural collapse of carbon framework, Ma et al.

(2000) have employed two- step carbonization method. In this method, ordered microporous carbon was prepared by filling as much as carbon precursors into the zeolite pores. Here additional incorporation of carbon precursor was achieved by chemical vapour deposition of propylene gas. In the first step, carbon precursor (Furfural alcohol) was incorporated into zeolite Y.

The mixture was stirred for more than 5 days, filtered and followed by washing with mesitylene to remove the carbon precursor from the external surface of the zeolite. The FA/zeolite was polymerized by heating at 150 °C under N_2 flow. The resultant composite was heat treated at 700 °C for 4 h to carbonize the polymer in the zeolite pores. After this temperature had been increased to 800 °C and propylene gas was passed for 4 h. In the second step, pyrolytic carbon was deposited into the remaining pores of the zeolite. After this, carbon/zeolite composite was washed with HF and HCl solution to remove the template framework. The carbon, so produced had almost no mesoporosity. This is confirmed by N_2-adsorption isotherm. XRD result showed some amorphous peak of carbon at 23°. This peak can be due to partial collapse of the carbon framework and/or due to the presence of graphitic domains deposited outside the zeolite pore system (Xia et al., 2010). Ma et al. (2001) improved the synthesis of ordered microporous carbon by additional heat treatment after the propylene gas CVD. The ordered microporous carbon prepared by this method exhibits BET surface area of 3600 m²/g.
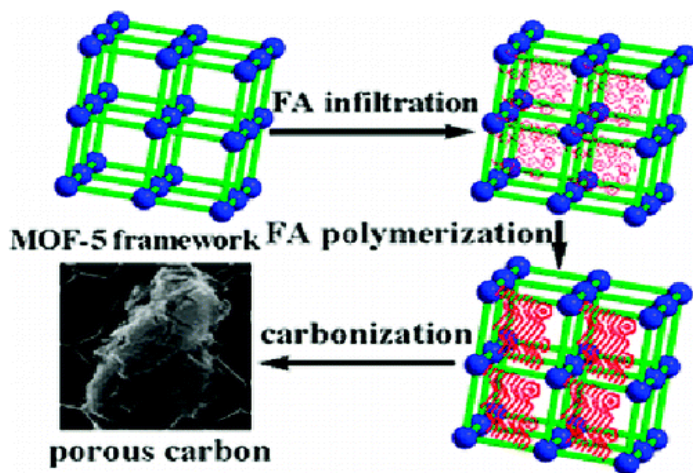
Figure 2.4: Schematic representation of nanoporous carbon from MOF-5 (Liu et al., 2008).

Apart from zeolite, metal organic framework (MOF) can also be used as a template for microporous carbon. Liu et al. (2008) have synthesized microporous carbon by heating the carbon

precursor within the pores of MOF-5 followed by carbonization and removal of template (Fig. 2.4). The MOF-5 templated carbon exhibits high BET surface area (2872 m²) and pore volume (2.06 cm³/g), but contained both micropores and mesopores. The presence of mesopores may be due to the void formation or partial filling of carbon precursor into the MOF-5. The MOF-5 templated carbon exhibits hydrogen uptake as well as excellent electrochemical properties as an electrode material.

Ordered Mesoporous Carbons (OMC): Ryoo et al. (1999) have first reported the synthesis of mesoporous carbon (Fig. 2.5). The synthesis was performed using sucrose as the carbon precursor and mesoporous silica molecular sieve (MCM-48) as a template with sucrose and sulfuric acid followed by polymerization, carbonization and the removal of the silica template. The resultant mesoporous carbon was named as CMK-1, which had different structural symmetry from that of the silica template. On the other hand, Hyeon's group (1999) used aluminium implanted MCM-48 as a template and phenol as the carbon precursor. The generated carbon was designated as SNU-1, which exhibited excellent performance as an electrochemical double layer capacitor (Lee at al., 1999).
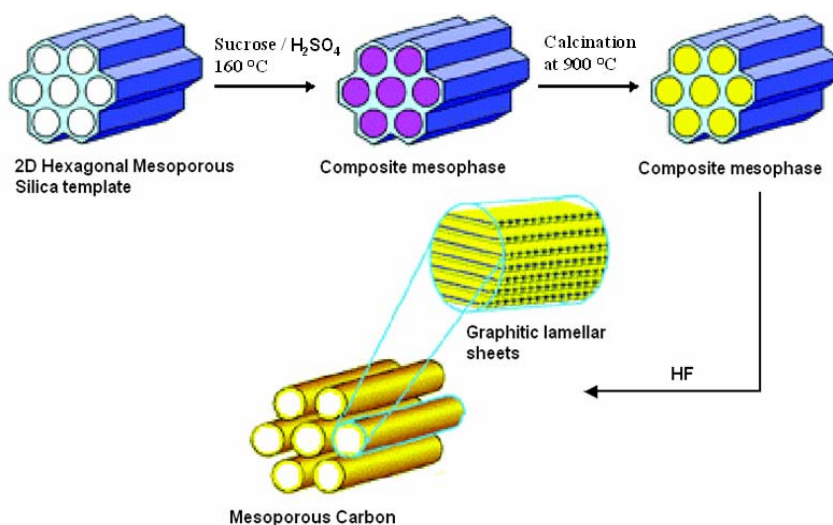
Figure 2.5: Schematic representation of synthesis of OMC from silica

Ryoo et al. (2000) have synthesized hexagonally ordered mesoporous carbon (CMK-3) by using ordered mesoporous silica molecular sieve SBA-15 as a template, sucrose as the carbon precursor and sulfuric acid as the carbonization catalyst. The structure of CMK-3 carbon is an inverse replica of silica template. Depending on the degree of pore filling of the carbon precursor into the hexagonal pores of SBA-15, different carbon structure can be obtained. If the pores of SBA-15 are completely filled, CMK-3 is generated, in which carbon nanorods are interconnected by spacers. On the other hand, if the pore system of SBA-15 is partially filled with carbon precursor, CMK-5 is obtained with an array of hollow carbon tubes (Lei et al., 2008). Table 2.1 summarizes the mesoporous cabons generated using nanocasing method.

Table 2.1: List of the reported ordered mesoporous carbons (Lu and Schüth, 2006).

OMC	Space group	Template	Space group	Precursor
CMK-1 (SNU-1)	$I4_1/a$ or lower	MCM-48	$Ia3d$	sucrose, phenol resin
CMK-2	Unknown cubic	SBA-1	$Pm3n$	sucrose
CMK-3	$p6mm$	SBA-15	$p6mm$	sucrose,
CMK-3 analogue	$p6mm$	HMS MSU-H SBA-3 MCM-41	$p6mm$	sucrose, phenol resin, furfuryl alcohol
CMK-4	$Ia3d$	MCM-48	$Ia3d$	acetylene
CMK-5	$p6mm$	SBA-15	$p6mm$	furfuryl alcohol
NCC-1	$p6mm$	SBA-15	$p6mm$	furfuryl alcohol
N-OMC	$p6mm$	SBA-15	$p6mm$	acrylonitrile, pyrrole
G-CMK-3	$p6mm$	SBA-15	$p6mm$	acenaphthene, benzene, mesophase pitches, pyrrole, poly(vinyl chloride)
OMC (cubic)	$Ia3d$	KIT-6, FDU-5	$Ia3d$	sucrose, furfuryl alcohol
OMC (cubic)	unknown	FDU-12	$Fm3m$	sucrose
OMC (cubic)	$Im3m$	SBA-16	$Im3m$	sucrose, furfuryl alcohol, acenaphthene

Lee et al. (2000) have reported the synthesis of new type of high surface area mesoporous carbon using hexagonal mesoporous silica (HMS) aluminosilicate as a template. The pores of HMS are 3D interconnected. HMS templated carbon was named as SNU-2. HMS template uses cheap primary alkyl amines as a structure directing agent. The advantages of using HMS as a template includes, a shorter synthesis time, no hydrothermal reaction and high silica recovery. Ryoo and co-workers (2005) synthesized ordered mesoporous carbons with cubic Im3m structure using sucrose, furfural alcohol and acenaphthene as the carbon precursor and mesoporous silica SBA-16 as a template. This study showed that, sucrose is not suitable for the formation of rigidly interconnected pores through cage-like silica SBA-16. When furfural alcohol was used as a carbon source, cubic Im3m structure can be retained in the resulting carbon (Kim et al., 2005). On the other hand, liquid crystalline mesophases can also be prepared in non-aqueous solution. This appears to be one of the most promising routes to the formation of non-silica mesoporous solids. Such soft-templating is defined as a process in which organic molecules serve as a 'mold' and around which a framework is built up (Fig. 2.6).
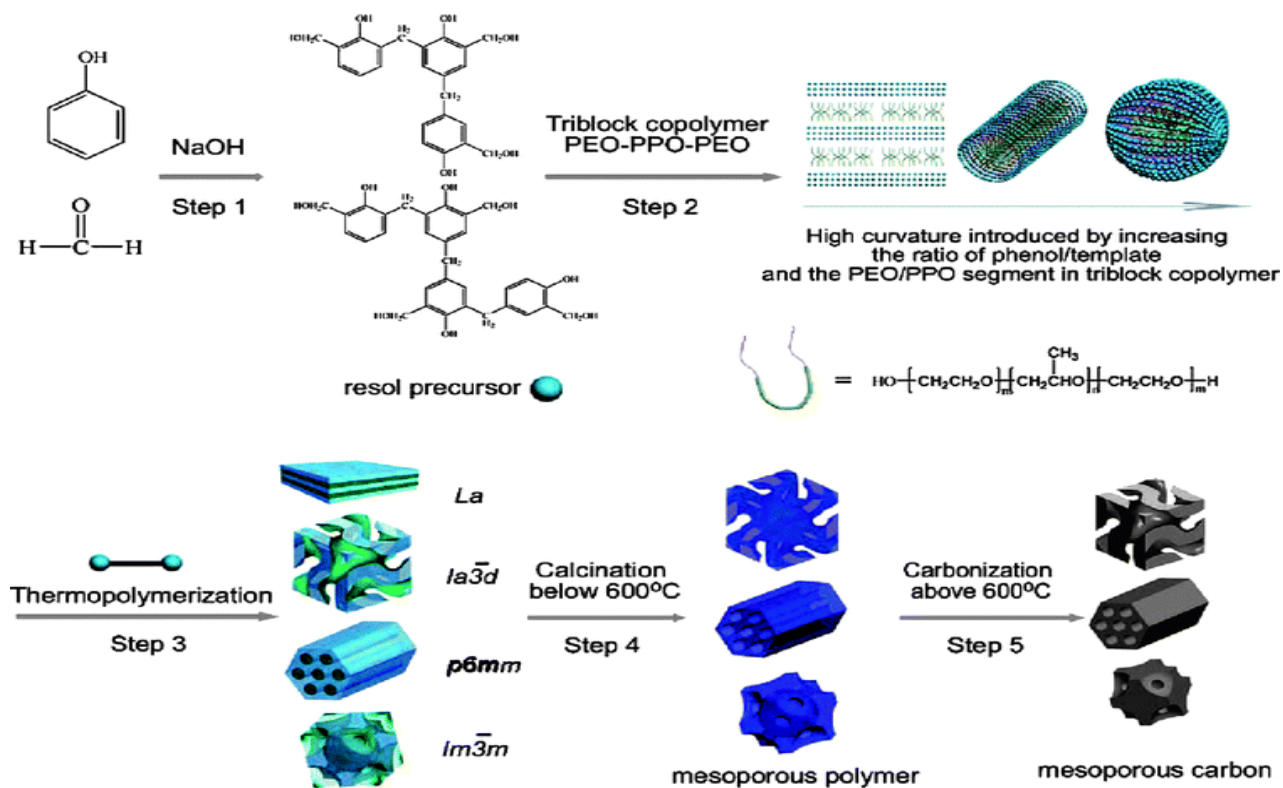
Figure 2.6: Schematic representation of the preparation of ordered mesoporous polymer resins and carbon frameworks (Meng et al., 2006).

2.2.3 Graphenes

In comparison with CNTs, graphene nanosheet (GNS) has not only contains similar stable physical properties, but also contains large surface area (2620 m²/g). It can be considered as a plat CNTs. GNS has been reported to have good dispersion stability and large surface area. GNS supported catalyst possesses larger electrochemical surface area (47.9 m²/g) than the Vulcan supported catalyst (28.3 m²/g) and it can be attributed to the size of PtRu particles well loaded on GNS. Preparation of GNS based catalyst is shown in Fig. 2.7. Normalized current density (considering electrochemical surface area at 700 mV) of PtRu/GNS and PtRu/VC are 0.113 and 0.0812 mA g/m² respectively. The increase in electrochemical activity of PtRu/GNS can be attributed to dispersed particle size effect and large electrochemical surface area (Bong et al., 2010).
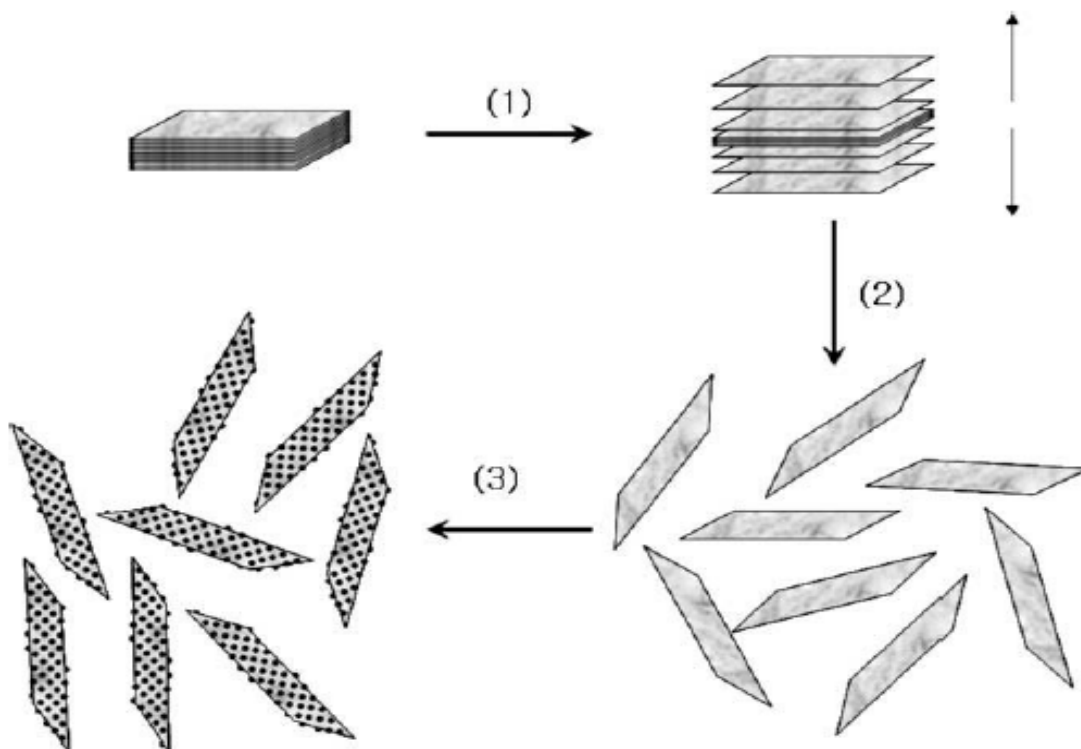
Figure 2.7: Schematic representation of synthesis of graphene nanosheet supported catalyst.
(1) Oxidation of graphite to graphite oxide with larger inter layer distance,
(2) exfoliation of graphite oxide by ultrasonication and
(3) preparation of GNS based catalyst by colloidal method (Bong et al., 2010).

2.2.4. Onion-like fullerenes (OLFs)

OLFs have been synthesized by chemical vapor deposition of ferrocene in a mixed stream of C_2H_2 and Ar at 1100 °C (Wang et al., 2006). Xu et al. (2006) have reported the onion-like fullerenes as a support material for direct methanol fuel cell. Pt/OLFs catalysts were synthesized by an impregnation-reduction method. The Pt metal supported on OLFs had 3.05 nm, whereas Pt supported on Vulcan carbon had 4.10 nm metal particle sizes. Pt/OLFs exhibit 20 % higher current density at 0.78 V compare to Pt/Vulcan XC-72. The higher catalytic activity of the Pt/OLFs can be attributed to smaller particle size.

2.3 OTHER APPLICATIONS OF POROUS CARBONS

2.3.1 Hydrogen Storage

Hydrogen has been considered as an alternative fuel and energy carrier. However, the storage and transportation have become the major limiting factors for hydrogen economy. Among all the available fuels, hydrogen is having high calorific value per unit weight. The US Department of Energy (DOE) has targeted 6.0 wt.% hydrogen storage by 2010 and 9 wt.% by 2015. An efficient and effective storage medium for hydrogen is required for the application of hydrogen in fuel cells and as an energy carrier (Viswanathan and Scibioh, 2006). The maximum value of hydrogen adsorption depends on the amount of hydrogen that can be accommodated in a monolayer. There are multiple ways to store hydrogen, including compressed gas, liquefaction, metal hydrides, complex hydrides and porous adsorbents. The most necessary requirements for a hydrogen storage system are, to pack hydrogen as close as possible and reversibility of uptake and release. But actually none of these techniques are capable of satisfying all the criteria of size, efficiency, cost, kinetics and safety required for the transport applications. The drawbacks of the high pressure storage method are relatively low hydrogen density and very high gas pressure. Liquefaction method requires large amount of energy.

Among them carbon materials have attracted lot of attention for hydrogen storage due to its adsorption ability, fast kinetics, complete reversibility, low cost and mainly high surface area, pore microstructure and low mass density. Textural parameters (surface area, pore volume and pore size) and surface properties (functionality) are determining the hydrogen storage capacity of

porous carbon. The hydrogen storage values are dependent on many parameters of the carbon nanotubes, including their structure, structure defects, pretreatment, purification, geometry (surface area, tube diameter and length), arrangement of tubes in bundles, storage pressure and temperature (Wang et al., 2009).

Activated carbon is extensively studied as a hydrogen storage medium due to its storage properties. The hydrogen storage capacity of activated carbon varies linearly with specific surface area of the activated carbon (Rzepka and Lamp, 1998). The nanostructured carbon materials like carbon nanotubes (CNT) and GNF (graphite nanofibers) exhibit high hydrogen storage capacity (HSC). Hydrogen molecules can be located inside the nanotubes or interstitially between them. The maximum possible HSC in CNTs is about 5-7 wt.% with all the necessary conditions (Hirscher et al., 2002). Some reports show greater than 7 wt.% storage capacities. But these results are not reproducible.

Hydrogen storage in CNTs can be measured by gravimetric method, volumetric method and thermal desorption spectroscopy. Gravimetric method measures the weight changes of the specimen due to absorption or desorption of hydrogen. Volumetric method measures the pressure drop due to hydrogen adsorption. Thermal desorption spectroscopy measures only the hydrogen desorption in high vacuum using mass spectrometry (Fan et al., 1999). Chambers et al. (1998) reported 67 wt.% of hydrogen storage using GNF herringbone and 54 wt.% by GNF platelet. GNF herringbone has higher storage capacity due to its geometric structure.

2.3.2 Capacitor

A capacitor is a device that stores electrical charge as well as potential energy. The amount of energy stored is equal to the work done to charge it. Capacitors have many electronic applications like storing electric potential energy, delaying voltage changes when coupled with resistors, filtering out unwanted frequency signals, forming resonant circuits and making frequency –dependent and independent voltage dividers when combined with resistors. On the basis of electrode material and storage mechanisms, electrochemical capacitors are as classified as electrochemical double-layer capacitors (EDLCs) that employ high surface area carbon and pesudocapacitors (supercapacitors) in which transition metal oxide or conducting polymers are

used as electrodes (Kim and Kim, 2006). EDLCs are one of the promising candidates for potential application in electric vehicles and other high power applications. Activated carbon is mostly explored as a capacitor. However, micropores in activated carbon can be easily accessed by the electrolyte and the exposed surface in micropores is not suitable for charge storage at high loading current density. Recently, highly ordered mesoporous carbons (HOMCs) have received much attention due to their well-defined structure and high surface area. Yuan et al. (2009) have reported synthesis of highly ordered mesoporous carbon via in situ template method for supercapacitors. They followed the one-step synthesis of HOMC using diluted sulfuric acid as cross-linked reagent, P123 and sucrose as the carbon precursor. The resulting ordered mesoporous carbon exhibits high surface area (1628 m²/g) and high specific capacitance (161 F/g) at low sweep rate of 5 mV/s. And this specific capacitance does not decay in the range from 1 to100 mV/s, specifies its capability of fast ion diffusion within the mesoporous structure.

Chen et al., (2009) have reported the synthesis of mesoporous carbon spheres (MCSs) via a hydrothermal route. Monodisperse carbon spheres (CSs) have been synthesized via a hydrothermal method using glucose as the carbon precursor without any catalysts. The CSs with high surface area obtained with large number of hydrophilic groups by treatment with molten KOH. Single electrode of MCs has higher specific capacitance of 253 F/g. This value increases by 20 % after the introduction of Pt nanoparticles. 10 wt.% Pt loading on MCs has been shown higher specific capacitance of 302 F/g. Chen et al. (2010) have demonstrated the usage of graphene oxide supported needle-like MnO_2 nanocomposites (GO-MnO_2) as supercapacitors.

Graphene is having monolayer arrangement of carbon atoms in a honeycomb network and it can be considered as an unrolled CNT. They have fabricated GO-MnO_2 composite through a simple chemical route (in a water–isopropyl alcohol system) without the usage of templates or surfactants. Intercalation and adsorption of manganese oxide into the GO sheets is followed by the nucleation and growth of the crystal species in a double solvent system, which results in exfoliation of GO sheets. Electrochemical properties can be enhanced by the chemical interaction between GO and $MnO_{2.}$ The GO-MnO_2 composite exhibits good electrochemical behaviors and that can be used as supercapacitor.

EXPERIMENTAL METHODS

3.1 STARTING MATERIALS

Hexachloroplatinic acid (Sigma) and 5 wt.% Nafion solution (Sigma) were used for the electrocatalyst and electrode preparation, respectively. Mordenite and Zeolite Y (NaY) (Sud-Chemie) were used as template materials. Analytical grade of sulphuric acid (98%; Merck) was used as electrolyte for CV analysis. Analytical grades of solvents like acetone, ethanol and methanol were purchased from (SISCO). High pure N_2, O_2 and H_2 gases were used for heat treatment, ORR and reduction processes (99.95 %; Indian Oxygen).

3.2 CHARACTERIZATION TECHNIQUES

3.2.1 X-ray diffraction (XRD)

XRD patterns of the samples were recorded on Rigaku miniflex (II) X-ray diffractometer using Cu K_α (λ= 1.5405 Å). The crystallite size was calculated by X-ray line broadening method using Debye-Schrrer equation (Cullity, 1978),

$$d = K\lambda / (\beta \cos\theta) \tag{3.1}$$

where, d is the crystallite size in nm, K is the numerical constant, 0.86, λ is the wavelength of radiation used, β is full width at half maximum in radians and θ is the Bragg diffraction angle in degrees, at the peak maximum. The XRD patterns were recorded at the scan rate of 3°/min, sampling width of 0.02° for the 2θ range of 5-90°.

3.2.2 BET surface area measurements

Nitrogen adsorption/desorption studies were carried out with Micromeritics ASAP2020. Surface area of the sample was calculated using BET equation. Degassing of the sample was done at 373 K for 2 h and at 423 K for 3 h.

3.2.3 Scanning electron microscopy (SEM)

Scanning electron micrographs were recorded using FEI, Quanta 200F (30 kV). The samples in the powder form were taken on the carbon tape and mounted on the SEM sample holder and images were recorded.

3.2.4 Transmission electron microscopy (TEM)

Transmission electron micrographs were recorded on a Philips CM20 model (200 kV). Few milligrams of the samples (1-2 mg) were dispersed in few mL (1-2 mL) of ethanol by ultrasonication for 15 minutes and a drop of the dispersion was placed on a carbon coated copper grid and allowed to dry in air at room temperature.

3.2.5 X-ray photoelectron spectroscopy (XPS)

The X-ray photoelectron spectroscopic studies were performed using Omicron Nanotechnology instrument using Mg Kα radiation. The base pressure of the analysis chamber during the scan was $2*10^{-10}$ milli bar. The pass energies for individual scan and survey are 20 and 100 eV, respectively. The spectrums were recorded with step width of 0.05 eV.

3.2.6 Electrochemical measurements

BAS Epsilon Potentiostat was used for the electrochemical studies. All the electrochemical measurements were performed with three electrode cell assembly, consists of electrocatalyst coated glassy carbon disk (dia. = 0.3 cm, geometrical surface area = 0.07 cm^2) as the working electrode, Pt foil (1.5 cm^2) as the counter electrode and SCE as the reference electrode. Cyclic voltammetric studies for hydrogen adsorption/desorption charge determinations were conducted in 1M H_2SO_4. CV and chronopotentiometric studies were carried out in 1M methanol and 1M sulphuric acid. The working electrode was fabricated by dispersing 10 mg of the catalyst in 1 mL of distilled water by ultrasonication for 15 min. 10 μL of the dispersion was placed on 0.07 cm^2 of the glassy carbon electrode, and dried in an oven at 80 °C for a few minutes. Then, the resulting dried catalyst ink was coated with 5 μL of 5 wt.% Nafion solution followed by drying in an oven for a few minutes.

Determination of Electrochemical Active Surface Area (EAS): Cyclic voltammetry was employed to obtain electro-active surface area of the electrode materials in order to account for the higher current response in methanol oxidation. Figure 3.1 depicts a model cyclic voltammogram obtained in 1M H_2SO_4 between -0.2 V and + 1.0 V Vs SCE at a scan rate of 50 mV/s. All the prepared Pt catalysts exhibits the hydrogen adsorption and hydrogen desorption peaks between -0.2 V and + 1.0 V. The active Pt surface area of the electrodes was evaluated from the columbic charge for hydrogen desorption (Q_H) of the electrode. The value of Q_H was calculated as the mean value between the amounts of charges exchanged during the electro adsorption and desorption of hydrogen on Pt sites. The electrochemical active surface area of the Pt/C catalyst was determined from the charge for hydrogen adsorption/desorption using equation 3.2. A model calculation for EAS is given in the subsequent section.

Electrochemical active surface area (EAS) (m^2/g)

$$= \quad QH/ ([Pt] \times 0.21) \quad\quad\quad …………..\text{ (3.2)}$$

Q_H – Average charge for hydrogen adsorption/desorption in mC/cm^2
[Pt] – loading of platinum in mg/cm^2
0.21 – charge (in mC) required to oxidize one monolayer of hydrogen from 1 cm^2
     of platinum black (Ralph *et al.*, 1997; Pozio *et al.*, 2002).
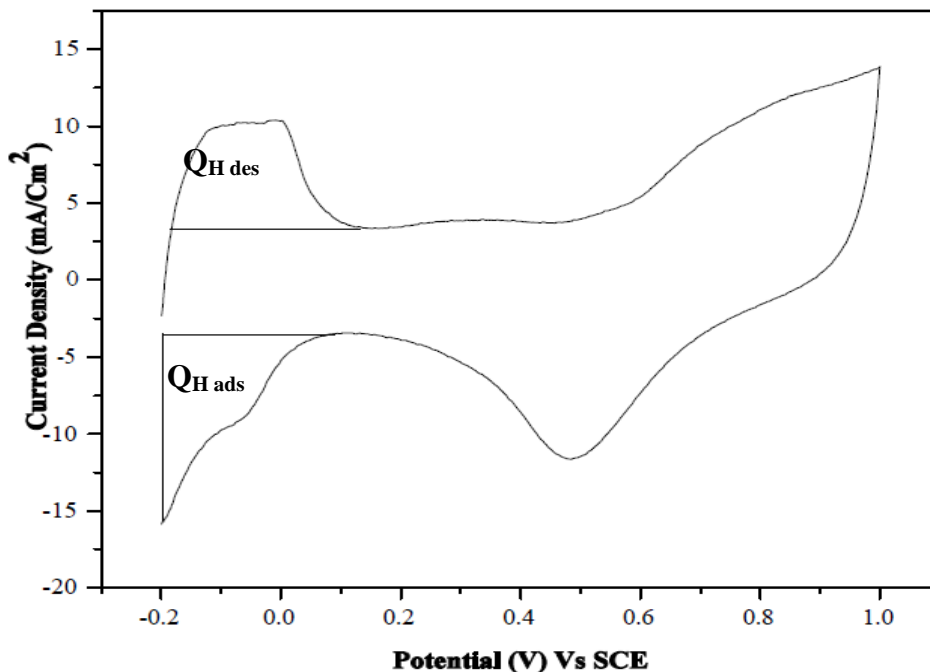
Figure 3.1: A model Cyclic Voltammogram of Pt/C catalyst in 1M H_2SO_4 at 50 mV/s.

Calculation of [Pt] - Pt Loading

100 mg catalyst contains 20 mg Pt

10 mg catalyst contains = (10/100) x 20 = 2 mg of Pt

2 mg of Pt is dispersed in 1 ml (1000 μl) of distilled H_2O, and 10 μL of the dispersion is dispensed on 0.07 cm^2 area of glassy carbon electrode.

10 μL contains = (2 mg/1000) x 10 μL = 0.02 mg Pt

Pt loading (mg /cm^2) = (0.02/0.07) = 0.286

Charge calculation for hydrogen desorption

No. of square units during hydrogen desorption = 122

Area of each square unit = 122 x 8.33 x 0.123 (mA/cm^2) x mV

$$= 125 \ (mA/cm^2) \ x \ mV$$

Charge during hydrogen desorption = [125 (mA/cm^2)x mV] / 25 mVs^{-1}

$$= 2.5 \ (mA/cm^2)s$$

$$= [2.5 \ (mA/cm^2)s]/3600$$

$$= 6.94 \ x \ 10^{-4} \ mA.h/cm^2$$

26.8 Ah = 96500 C

Charge (mC/cm^2) = [(6.94 x 10^{-4} mA.h/cm^2) x 96500]/ 26.8

$$= 2.5 \ mC/cm^2$$

Charge calculation for hydrogen adsorption

No. of square units during hydrogen adsorption = 302

Area of each square unit = 302 x8.33 x 0.123 (mA/cm^2) x mV

$$= 309.4 \ (mA/cm2)x \ mV$$

Charge during during hydrogen adsorption = [309.4 (mA/cm^2)x mV] / 50 mVs^{-1}

$$= 6.19 \ (mA/cm^2)s$$

$$= [6.19 \ (mA/cm^2)s]/3600$$

$$= 1.72 \ x \ 10^{-3} \ mA.h/cm^2$$

26.8 Ah = 96500 C

Charge (mC/cm^2) = [(1.72 x 10^{-3} mA.h/cm^2) x 96500]/ 26.8

$$= 6.19 \ mC/cm^2$$

Average Q_H = [2.5 + 6.19]/2 = 4.345 mC/cm^2

[Pt] = 0.286 mg/cm^2

EAS = 4.345/[0.286 x 0.21] = 72.34 (mC/cm^2)/[mg/cm^2 x mC/cm^2]

$$= 72.34 \text{ cm}^2/\text{mg} = 72.34 \times 10^{-4} \text{ m}^2/10^{-3}\text{g}$$

EAS = 7.23 m^2/g

Determination of Mass Specific Activity: Mass Specific Activity of the Pt/C catalyst was determined using equation 3.3. The current density (forward peak current density) for methanol oxidation is obtained from the cyclic voltammogram of the catalyst in 1M methanol and 1M H_2SO_4.

Mass Specific Activity (mA/ mg) = current density (mA/cm^2)/ Pt loading (mg/cm²)...............(3.3)

Determination of Specific Activity:

Specific activity was determined using equation 3.4.

Specific Activity (A/m^2 of Pt) = Mass Specific Activity (A/g)/EAS (m^2/g)…………………..(3.4)

ORDERED MICROPOROUS CARBONS
(CNI-1 and NCNI-1)

4.1 INTRODUCTION

Porous materials have both continuous skeletons and voids that can be randomly arranged (disordered pore system) or highly regular (ordered pore system) with large surface areas. According to the definition of IUPAC (International Union of Pure and Applied Chemistry), porous materials can be divided into microporous (with pore diameter < 2 nm), mesoporous (pore size in the range of 2-50 nm) and macroporous materials (pore size >50 nm). Porous carbon materials form a large and important class of porous materials, which have been widely used for gas separation, water purification, catalyst supports, shape-selective catalysis, chemical separations and electrodes for electrochemical double layer capacitors and fuel cells (Lee et al., 2006; Lu et al., 2010).

Porous carbon materials constitute a very flexible set of supports for the preparation of heterogeneous catalysts. Their physical and chemical surface properties can easily be tailored to develop a large surface area to disperse the active phases, the proper pore size distribution to facilitate the diffusion of reactants and products to and from the surface, and the acid–base character needed for obtaining the best performance. The use of carbon as a catalyst support depends primarily on the relative inertness of its surface, which facilitates the interaction between active phases or between active phases and promoters, thus enhancing the catalytic behavior. This makes porous carbons an excellent choice as catalyst support in a great number of reactions.

Carbon materials are the most widely used support for fuel cell electrocatalysts due to its various properties. These properties include corrosion resistance, anisotropic electronic property, formation of intercalation compounds, strong covalent bond formation with variety of surface modifiers and adsorbing capacity of wide variety of materials. The nature of the carbon determines the electrochemical performance of electrocatalysts (Serp and Figueiredo, 2009). Interactions between the noble metal and the support may increase the catalyst performance. Carbon material

has a strong influence on the properties of the supported noble metal catalysts, such as metal particle size, morphology, size distribution, degree of alloying, stability and dispersion. Carbon supports also affect the performance of supported catalysts in fuel cells, such as mass transport, catalyst layer electronic conductivity, electrochemical active surface area, and metal nanoparticle stability during the operation. Hence, the optimization of carbon supports is very important in DMFC development.

For a fuel cell to operate efficiently, carbon materials must provide high dispersion of nanoparticles, be chemically inert and corrosion resistant, should have high electron conductance, should contain adequate porosity for the efficient mass transport of reactants and products and provide optimum water management. Carbon black, Vulcan XC-72 is the most common support material for fuel cell electrocatalyst. But nowadays various carbon materials have been investigated as electrocatalyst support like carbon nanofibers, carbon nanotubes, carbon aerogels and ordered nanoporous carbon (micro and mesoporous carbon).

Microporous carbons are widely used for gas and liquid separation, which are conventionally carried out by controlled pyrolysis of a carbon precursor or by post-modification of the existing pores. In comparison with zeolites, microporous carbons have several attractive features such as excellent shape selectivity for planar molecules, high hydrophobicity, heat resistance and high corrosion-resistance. Thus, microporous carbons can be used in many fields where zeolites are not suitable. For preparing microporous carbons, the most important parameter is finding an efficient method to control their pore size. Microporous carbons can be prepared with well-defined pore structures through the nanocasting process.

4.2 PREPARATION METHODS

Conventionally, there are three major methods for preparing porous carbons, including: 1) activation of carbon-containing precursors to prepare porous carbons (both physical and chemical); 2) carbonization of carbon-containing precursors to prepare porous carbons; 3) combination of sol-gel processes and carbonization to synthesize porous carbons; 4) the nanocasting approach to replicate porous carbons, which is a newly developed and method. Although the above methods are useful for the preparation of porous carbon materials, the synthesis of uniform porous carbon

materials has been very challenging. Among the above methods, nanocasting method has been widely used for preparing micro and meso structured materials.

4.3 NANOCASTING

Nanocasting is a process used to infiltrate a fluid (liquid, or even gas) precursor into the nanometer-sized pore channels of the hard templates, to convert the precursor by the nanostructure confinement into a target nanomaterial that duplicates the morphology and structure of the template, and finally to remove the template. Various inorganic materials, including silica nanoparticles (silica sol), zeolites, anodic alumina membranes, and mesoporous silica materials, have been used as templates (Lu and Schuth, 2010).
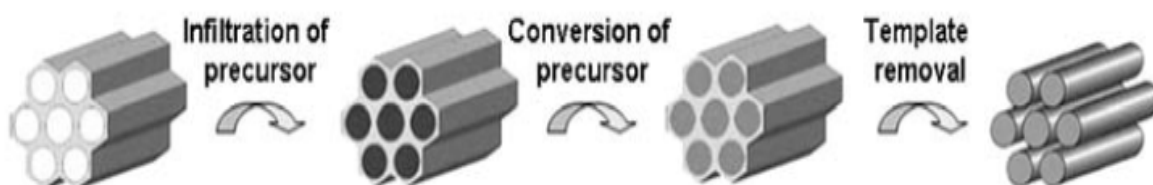
Figure 4.1: Schematic representation of nanocasting pathway, showing the change of the mesostructure during the process. The process mainly includes three steps: (i) precursor infiltration inside mesochannels of the silica template; (ii) conversion of the precursor in the nanochannals; (iii) removal of mesoporous silica template (Lu et al., 2010).

4.3.1 Use of furfural alcohol as carbon precursor

1 g of template (Mordenite) was impregnated with 4 ml of furfural alcohol and stirred for overnight. And then the suspension was filtered and washed with mesitylene to remove the carbon from the external surface of the template. Then the filtered sample was dried at 80 °C for 24 h and polymerized at 150 °C for 8 h. The polymerized sample was heat treated in the N_2 atmosphere at 700 °C for 3 h at the rate of 5 °C/min. After the heat treatment, the acquired sample was HF treated to remove the template and dried at 120 °C. The obtained ordered microporous carbon was designated as CNI-1. Then the prepared CNI-1 was characterized by XRD, BET, SEM and XPS.

4.3.2 Use of pyrrole as carbon/nitrogen precursor

Nitrogen can be introduced in carbons essentially in two ways, either by carbonizing nitrogen-containing organic compounds or mixtures of nitrogen containing precursors with nitrogen-free materials, or by treatment of carbon materials at high temperatures with nitrogen-containing gases which decompose at these temperatures with generation of highly reactive radicals. Here, carbonization of nitrogen-containing organic compounds had been followed for the preparation of nitrogen containing microporous carbon.

1 g of template (Mordenite) was impregnated with 4 ml of pyrrole and stirred for overnight. And then the suspension was dried at 80 °C for 3 h in an oven and then 3 h in vacuum oven for polymerization. The polymerized sample was heat treated in the N_2 atmosphere at 700 ° C for 3 h at the rate of 5 °C/min. After the heat treatment, the acquired sample was HF treated to remove the template and dried at 120 °C. The obtained nitrogen containing ordered microporous carbon was designated as NCNI-1. Then the prepared NCNI-1 was characterized by XRD, SEM, XPS and BET. The presence of nitrogen atoms in the carbon framework generates specific surface properties including the enhanced polarity, basicity and heterogeneity in terms of hydrophilic sites. The presence of nitrogen functional groups in the carbon framework also has a substantial effect on their catalytic activity.

4.4 CHARACTERIZATION

4.4.1 XRD

XRD patterns of the CNI-1 samples are shown in Fig. 4.2. Both furfural alcohol/mordenite composite and heat treated sample retained the ordered structure of the mordenite. During the HF treatment, CNI-1 from template can collapse and form an amorphous like structure due to insufficient impregnation of the precursor. Therefore, template removal process has to be optimized to get an ordered carbon structure. In this case, HF treatment had been optimized for 2 and 5 % of HF. And also different time duration had been employed like 3, 6 and 9 h. From XRD patterns, we can conclude that, different time duration was not making significant variations in the morphology of the prepared CNI-1.
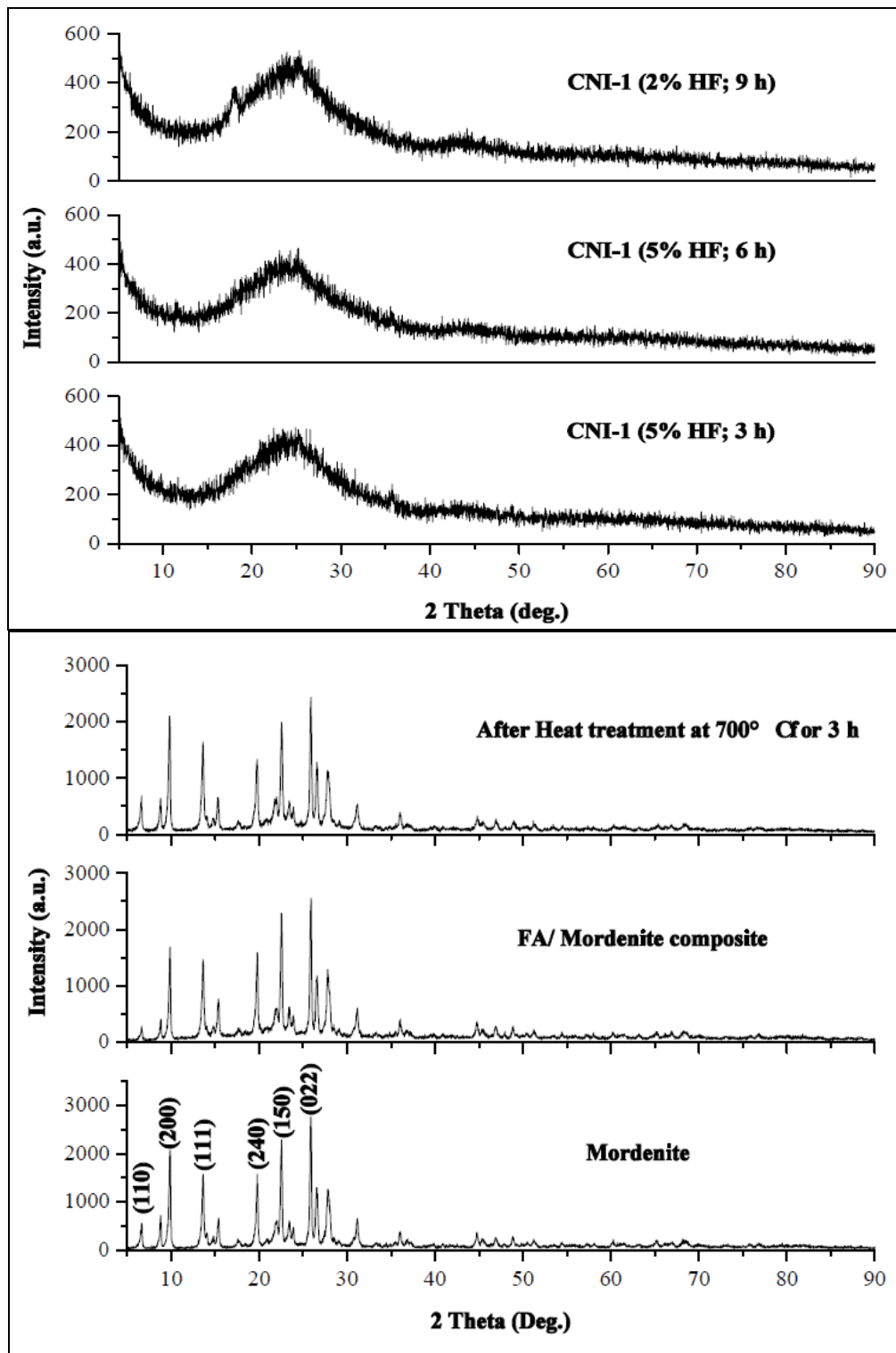
Figure 4.2: XRD pattern of CNI-1
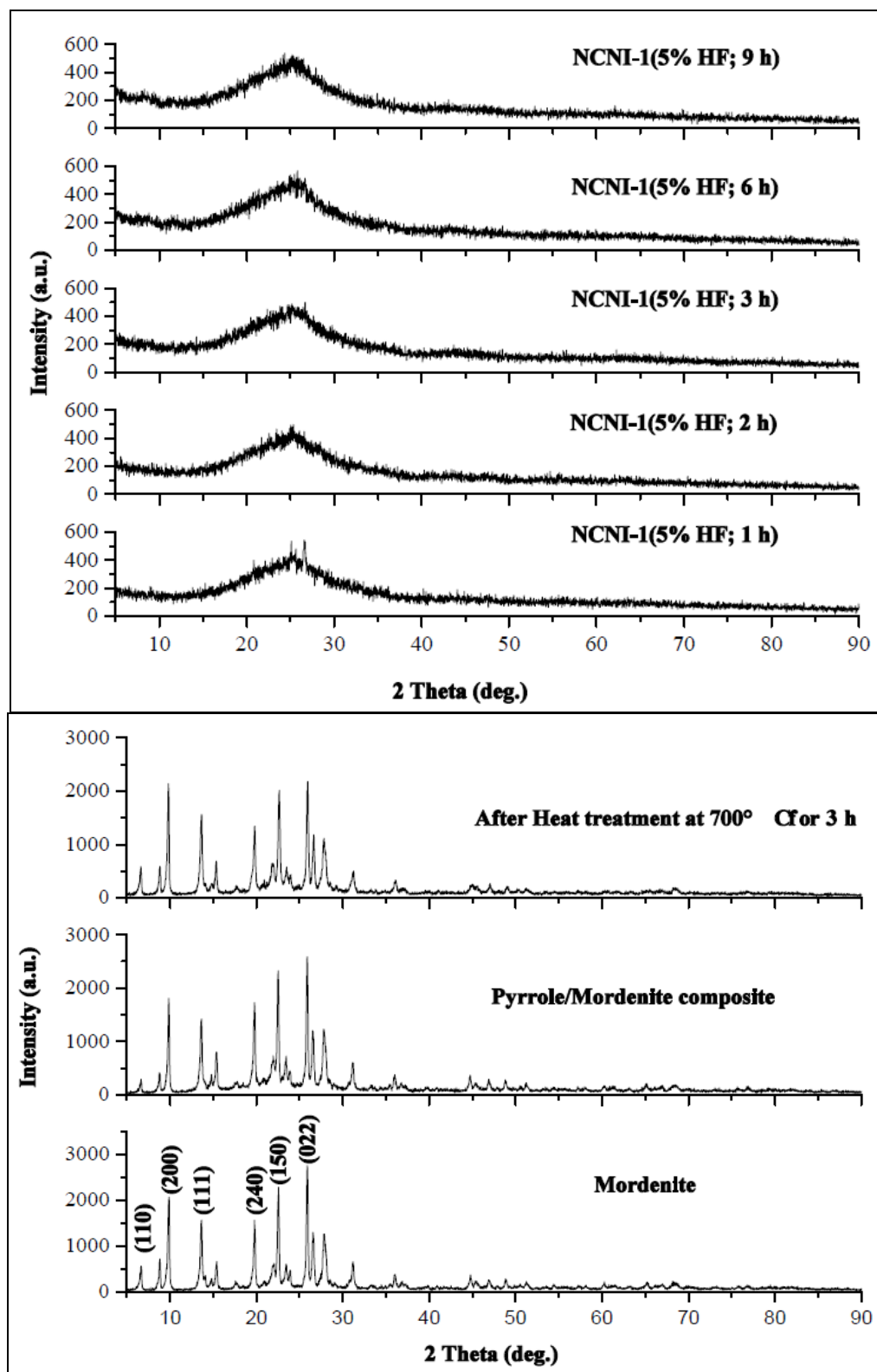
Figure 4.3: XRD pattern of NCNI-1

XRD patterns of the NCNI-1 samples are shown in Fig. 4.3. Both pyrrole/mordenite composite and heat treated sample retained the ordered structure of the mordenite. During the HF treatment, NCNI-1 from template can collapse and form an amorphous like structure due to insufficient impregnation of the precursor. Therefore, template removal process has to be optimized to get an ordered carbon structure. In this case, HF treatment had been optimized for 5 % of HF. And also different time duration had been employed like 1- 9 h. From XRD patterns, we can conclude that, different time duration was not making significant variations in the morphology of the prepared NCNI-1.

4.4.2 Textural properties

Nitrogen adsorption/desorption isotherms and pore size distributions of the CNI-1 and NCNI-1 are shown in Fig. 4.4 and 4.5 respectively. Textural properties of CNI-1 and NCNI-1 are given in Table 4.1. It is reported that the higher the degree of activation of the carbon sample, the higher is the decrease in surface area and pore volume, as increase in the degree of activation makes the pore walls thinner and thus are easily destroyed.
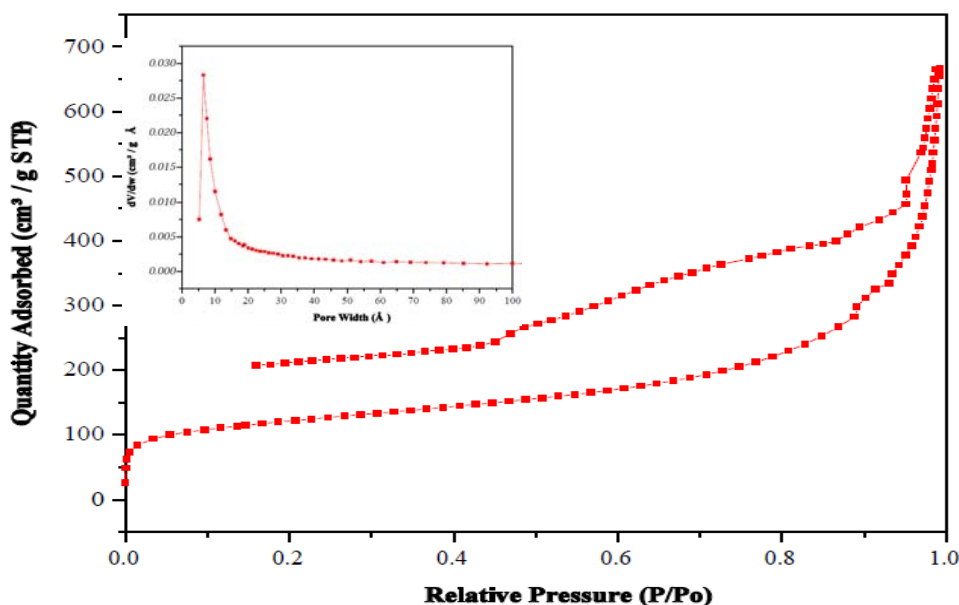
Figure 4.4: N_2 sorption isotherm of CNI-1. Inset: Pore size distribution of CNI-1.
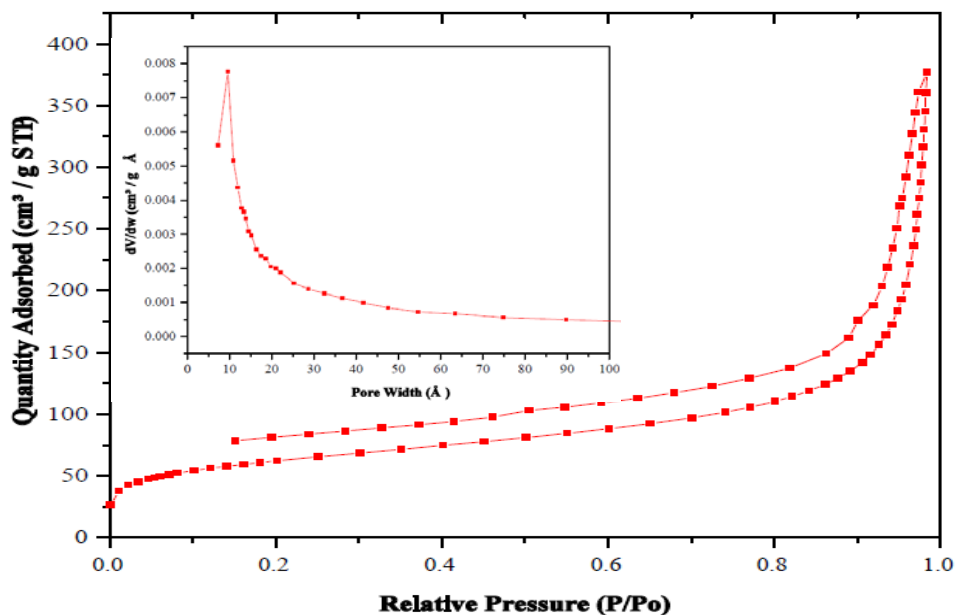
Figure 4.5: N$_2$ sorption isotherm of NCNI-1. Inset: Pore size distribution of NCNI-1.

N$_2$ adsorption/desorption isotherm of CNI-1 and NCNI-1 showed both type-I and type-IV isotherms (Fig. 4.4 and 4.5). Therefore, both the microporous carbons contained micropores as well as mesopores. And also, they had narrow pore size distribution unlike the amorphous carbon. From N$_2$ adsorption and pore size distribution plots, we can conclude that, carbon contained ordered pore structure. Horvath-Kawazoe differential pore volume plot was used for the pore size distribution plot.

Table 4.1: Textural properties of CNI-1 and NCNI-1

ONC	BET surface area (m²/g)	Pore volume (cm³/g)	Avg. Pore size (Å)
CNI-1	409	0.80	6.58
NCNI-1	218	0.56	9.58

4.4.3 Scanning Electron Microscopy
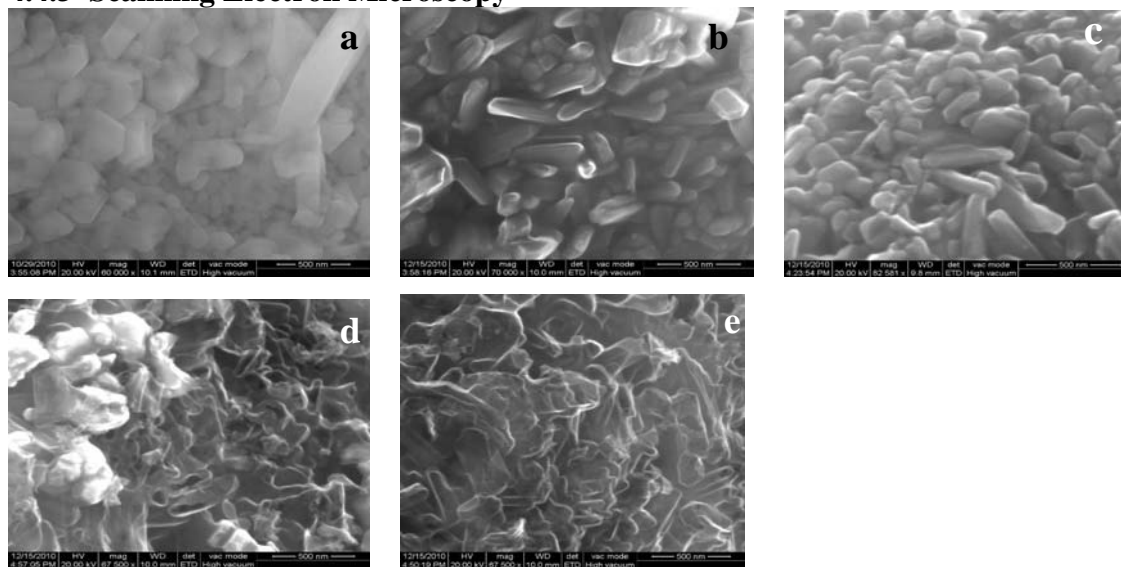
Figure 4.6: SEM of: (a) Mordenite; (b) FA/Mordenite composite; (c) Heat treated sample; (d) CNI-1(2 % HF; 9 h); (e) CNI-1 (5 % HF; 3 h); (f) CNI-1 (5 % HF; 6 h).
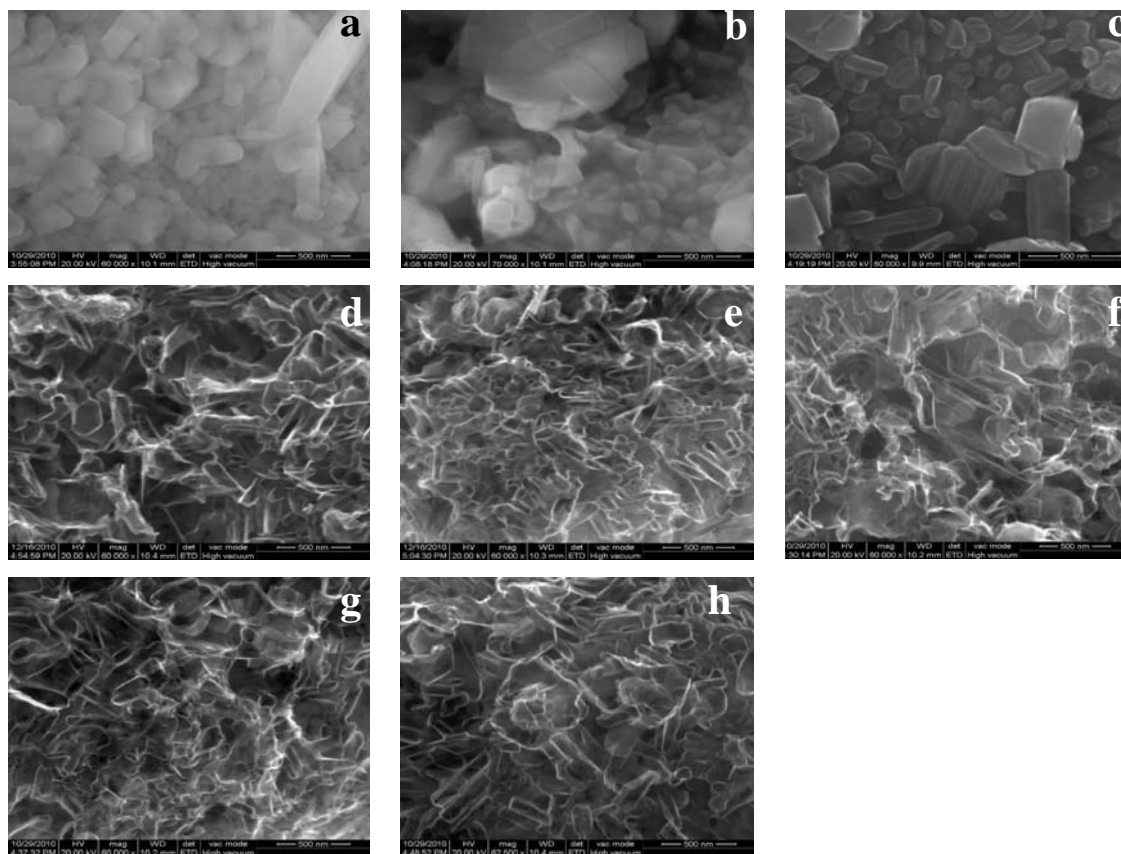
Figure 4.7: SEM of (a) Mordenite; (b) Pyrrole/Mordenite composite; (c) Heat treated sample; (d) NCNI-1 (5 % HF; 1 h); (e) NCNI-1 (5 % HF; 2 h); (f) NCNI-1 (5 % HF; 3 h); (g) NCNI-1 (5 % HF; 6 h); (h) NCNI-1 (5 % HF; 9 h);

Table 4.2: Elemental analysis results of CNC-1

Samples	Composition (atom %)			
	C	O	Al	Si
Mordenite	39.98	51.78	0.48	7.76
FA/Mordenite composite	32.43	53.33	0.55	13.69
Heat treated sample	23.61	54.71	00.7	20.97
CNI-1 (2 % HF; 9 h)	87.77	11.61	0.01	0.61
CNI-1 (5 % HF; 3 h)	88.12	11.85	0.01	0.02
CNI-1 (5 % HF; 6 h)	90.18	09.74	0.03	0.05

Table 4.3: Elemental analysis results of NCNI-1

Samples	Composition (atom %)			
	C	O	Al	Si
Mordenite	39.98	51.78	0.48	07.76
Pyrrole/Mordenite composite	43.35	44.31	0.57	11.78
Heat treated sample	47.28	43.06	0.30	09.36
NCNI-1 (5 % HF; 1 h)	92.82	07.06	0.04	00.08
NCNI-1 (5 % HF; 2 h)	90.07	09.88	0.02	00.03
NCNI-1 (5 % HF; 3 h)	90.22	09.65	0.03	00.10
NCNI-1 (5 % HF; 6 h)	91.11	08.81	0.05	00.03
NCNI-1 (5 % HF; 9 h)	89.45	10.47	0.04	00.05

Even though XRD patterns of CNI-1 (Fig. 4.2) and NCNI-1 (Fig. 4.3) showed an amorphous structure, from SEM images (Fig 4.6 and 4.7) and pore size distributions (Fig. 4.4 and 4.5) we can conclude that, the prepared microporous carbons were partially amorphous and partially ordered. Both the composites and heat treated samples retained the morphology of the mordenite template. After the HF treatment, carbon samples started forming the amorphous kind of structure. Elemental analysis of mordenite, composites and heat treated samples showed large amount of Al and Si content. HF treatment was required to remove the template. In the case of CNI-1 (2 % HF; 9 h), template was not completely removed. It was validated by both SEM image

and EDAX. But 5 % HF treatment was completely removing the template, leaving the required CNI-1. Finally we can conclude that, (5% HF; 3 h) can remove Si and Al completely. EDAX spectra of that corresponding carbon, CNI-1 (5% HF; 3 h) showed almost negligible amount of Si and Al. The elemental results of CNI-1 were tabulated (Table 4.2). And the EDX spectrums of CNI-1 were shown in Fig. A.1.

In case of NCNI-1, 5% HF treatment was done for different time durations to verify the effect of time for 5 % HF treatment. After the first hour only traces of Al and Si were there in NCNI-1. Those traces of Al and Si have also been removed in the second hour. After the second hour, HF treatment gives almost the similar kind of NCNI-1. These conclusions have been validated by the EDAX results. The elemental results of NCNI-1 were tabulated (Table 4.3). And the EDX spectrums of NCNI-1 were shown in Fig. A.2.

4.4.4 XPS
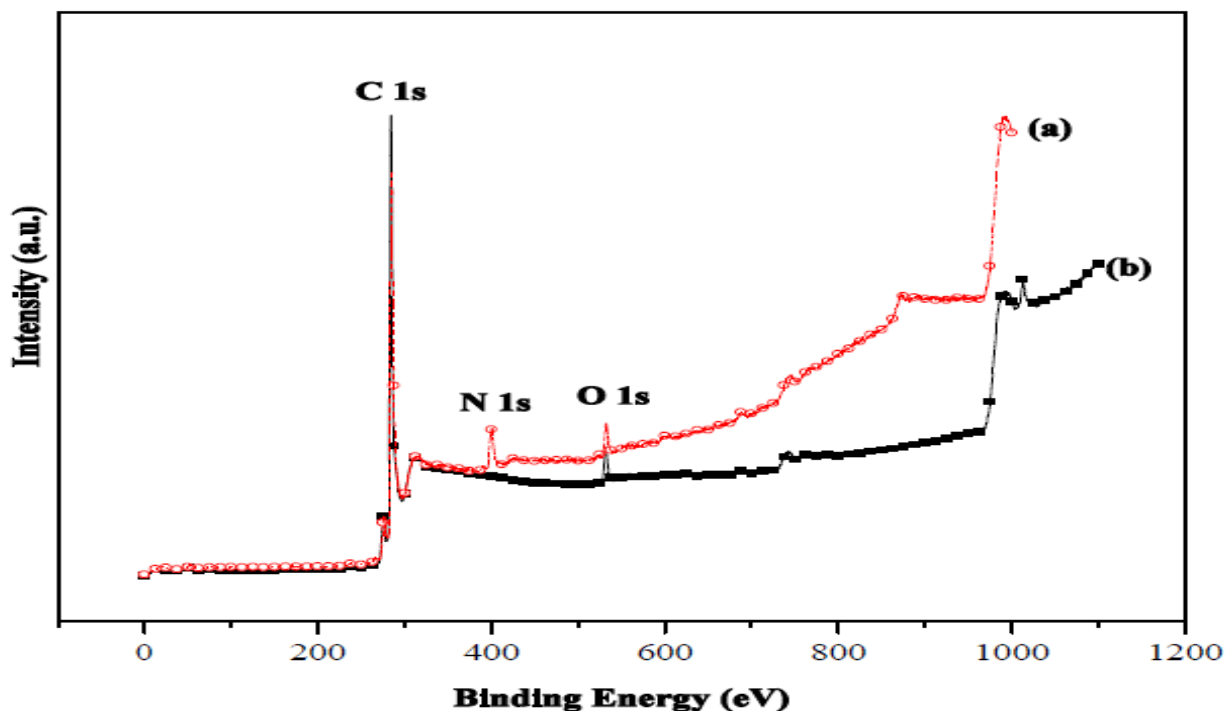
Figure 4.8: Survey XPS spectra of (a) NCNI-1 and (b) CNI-1

35

Fig. 4.8 shows survey spectra of CNI-1 and NCNI-1 by XPS. In the survey spectra, there are peaks of C 1s and O 1s in CNI-1 is common with NCNI-1. Anyhow, N 1s peak (399.6 eV) in survey XPS spectrum showed the presence of nitrogen only in the NCNI-1 and not in CNI-1. This obvious difference is due to the presence of nitrogen in the NCNI-1 matrix.
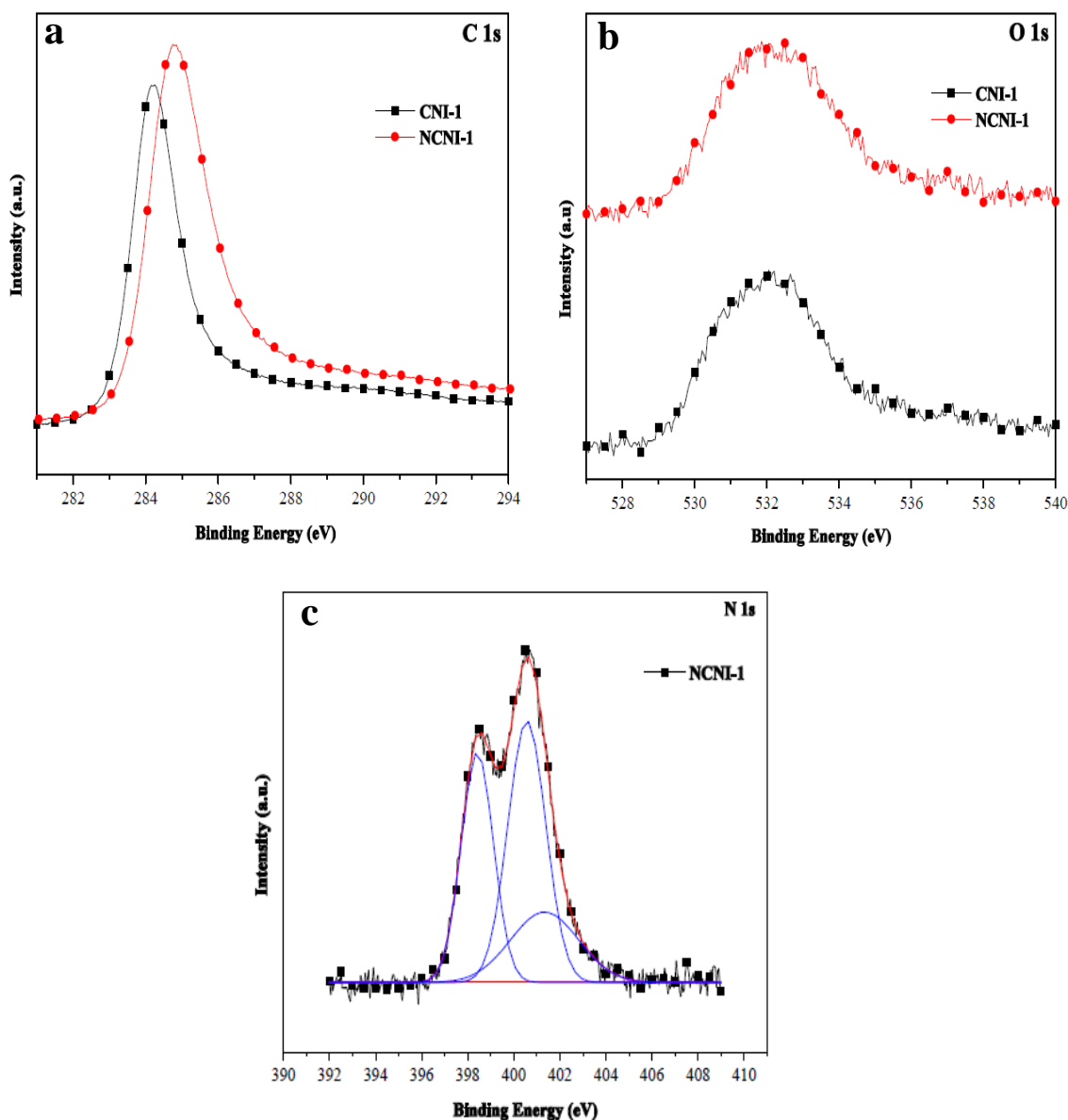
Figure 4.9: XP spectra of CNI-1 and NCNI-1(a) C (1s); (b) O (1s); (c) N (1s).

C 1s spectra for CNI-1 and NCNI-1 are shown in Fig. 4.9a. C 1s peak of nitrogen containing carbon material was slightly shifted to higher binding energy and suggested that this phenomenon occurred as a result of coordination between carbon and nitrogen. Therefore the

presence of C-N bond in NCNI-1 had been confirmed by XPS analysis. O 1s peak of nitrogen containing carbon material was also shifted to higher binding energy and suggested that this phenomenon occurred as a result of coordination between oxygen and nitrogen. N 1s spectrum was deconvoluted with three types of nitrogen. Peaks at 398.5, 400.5, and 401.4 eV were attributed to pyridinic, pyrrolic, and quaternary kind of nitrogen, respectively. Peak of pyrrolic nitrogen showed the highest proportion among the deconvoluted peaks. Possible types of nitrogen in carbon materials are given in Fig. 4.10.
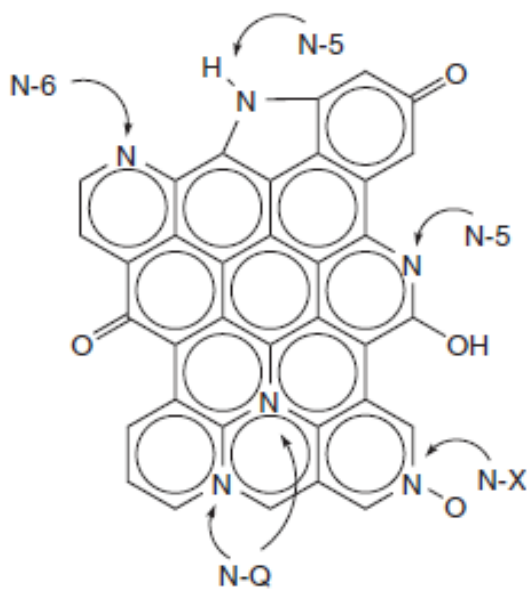
Figure 4.10: Model of a carbon layer with nitrogen atoms bonded differently (Kapteijn et al., 1999).

In XPS, the nitrogen 1s electron binding energy distribution is analyzed by deconvolution. Globally four or five types of nitrogen can be distinguished in carbonaceous materials by XPS: N-6 (398.7±0.3 eV), N-5 (400.3±0.3 eV), N-Q (401.4±0.5 eV), N-X1 and N-X2 (402–405 eV). A schematic picture of nitrogen in carbon materials is given in Fig. 4.10. N-6 corresponds to pyridinic nitrogen. N-5 to pyrrolic nitrogen and to pyridinic nitrogen in association with oxygen functionality, the so-called pyridones exhibit a shift relative to pyridinic nitrogen due to some charge distribution. N-Q in carbon is represented by nitrogen which substitutes for carbon in the aromatic graphene structure. Nitrogen oxide and nitrate structures represent the two N-X types (-CN and –NH$_2$) that are generally found in the deconvolution of the spectra (Kapteijn et al., 1999).

CHAPTER 5

CNI-1 and NCNI-1 SUPPROTED PLATINUM AS ELECTRODES FOR DMFC APPLICATIONS

5.1 ELECTRODE MATERIALS FOR METHANOL OXIDATION

Pt is the only element found to give atleast appreciable methanol oxidation current density and also could sustain the acidic condition of the fuel cell. It is due to its good adsorption capacity for methanol and its stability under oxidative conditions. The direct methanol fuel cell (DMFC) shown in Fig 1.2, consists of an anode at which methanol is oxidized to CO_2 through the following reaction (Hamnett, 1997),

$$CH_3OH \ + \ H_2O \quad \rightarrow \quad CO_2 \ + \ 6\,H^+ \ + \ 6\,e^- \quad E_0 = 0.016 \text{ V Vs SHE} \quad (1)$$
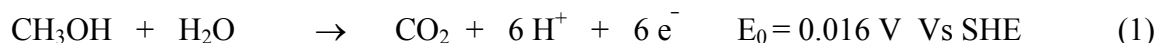
And a cathode at which oxygen (usually as air) is reduced to water or steam.

$$1.5\,O_2 \ + 6\,H^+ + 6\,e^- \ \rightarrow \ 3\,H_2O \qquad E_0 = 1.229 \text{ V Vs SHE} \quad (2)$$

With the over all reaction of,

$$CH_3OH + 1.5\,O_2 \quad \rightarrow \quad CO_2 + 2\,H_2O \qquad E_{cell} = 1.213 \text{ V Vs SHE} \quad (3)$$

The basic mechanism for methanol oxidation was reviewed by Parsons and VanderNoot, 1988, and can be summarized in terms of two basic functionalities: (a) Electrosorption of methanol onto the substrate. (b) Addition of oxygen to adsorbed carbon containing intermediates to generate CO_2. Very few electrode materials are capable of adsorption of methanol; only platinum and platinum based catalysts have been found to show both sensible activity and stability in acidic condition of fuel cells. The mechanism of oxidation of methanol is supposed to follow the sequence of steps as below (Viswanathan and Scibioh., 2006);

$$Pt(s) + CH_3OH \qquad \rightarrow \quad Pt - CH_2OH + H^+ + e^- \qquad (1)$$

$$Pt - CH_2OH + Pt(s) \qquad \rightarrow \quad Pt_2 - CHOH + H^+ + e^- \qquad (2)$$

$$\text{Pt}_2\text{–CHOH} + \text{Pt(s)} \quad\longrightarrow\quad \text{Pt}_3\text{–COH} + \text{H}^+ + \text{e}^- \tag{3}$$

$$\text{Pt}_3\text{–COH} \quad\longrightarrow\quad \text{Pt–CO} + 2\,\text{Pt(s)} + \text{H}^+ + \text{e}^- \tag{4}$$

$$\text{Pt(s)} + \text{H}_2\text{O} \quad\longrightarrow\quad \text{Pt–OH} + \text{H}^+ + \text{e}^- \tag{5a}$$

$$\text{Pt–OH} + \text{Pt-CO} \quad\longrightarrow\quad 2\,\text{Pt} + \text{CO}_2 + \text{H}^+ + \text{e}^- \quad \text{(or)} \tag{6}$$
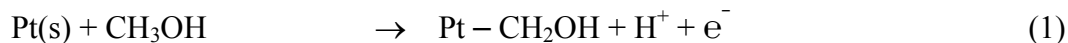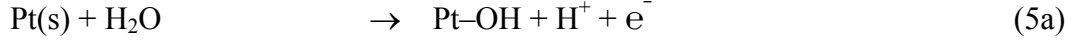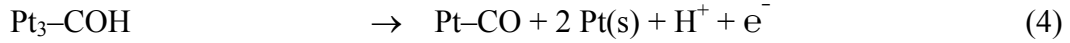
The formation of OH by water activation on the Pt surface (5a), which is a necessary step for the oxidative removal of adsorbed CO, requires a high potential. In terms of methanol oxidation at anode, such a high potential will limit the fuel cell application of a pure platinum catalyst. Therefore a second metal that can provide oxygenated species at lower potentials for oxidative removal of adsorbed CO is visualized. Binary Pt-based alloys, such as PtRu, PtOs, PtSn, PtW and PtMo have been investigated in order to improve the electro-oxidation activities of methanol. Among them, the Pt–Ru alloy has been found to be the most active binary catalyst. The enhanced activity of the Pt–Ru catalyst when compared with Pt for methanol oxidation has been attributed to both a bi-functional mechanism and a ligand (electronic) effect. The bi-functional mechanism involves the adsorption of oxygen containing species on Ru atoms at lower potentials thereby promoting the oxidation of CO to CO_2, which can be summarized as follows:

$$\text{Pt} + \text{CH}_3\text{OH} \rightarrow \text{Pt-CO}_{ads} + 4\text{H}^+ + 4\text{e}^- \tag{7}$$

$$\text{Ru} + \text{H}_2\text{O} \rightarrow \text{Ru(OH)}_{ads} + \text{H}^+ + \text{e}^- \tag{8}$$

$$\text{Pt-CO}_{ads} + \text{Ru(OH)}_{ads} \rightarrow \text{CO}_2 + \text{Pt} + \text{Ru} + \text{H}^+ + \text{e}^- \tag{5b}$$
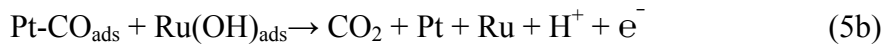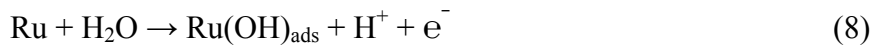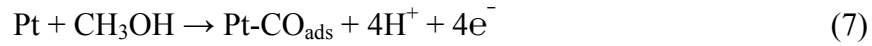
The catalytic activity of the Pt–Ru catalyst is strongly dependent on the composition, structure, morphology, particle size and degree of alloying. The current consensus is that the optimal Pt/Ru ratio is 1:1, and the particle sizes are better brought down to the nanoscale in order to improve the catalyst utilization. Alloying and nanoparticle supporting strategies could dramatically reduce the Pt content in the catalysts without performance compromise. The other strategy is support modification. Rapid development of nanotechnology, especially in the area of the synthesis of carbon nano-materials, expected to create more stable and active supported catalysts.

5.2 PREPARATION OF Pt/CNI-1 and Pt/NCNI-1

Due to its simplicity, impregnation method is often used for the preparation of catalysts. Catalyst preparation by impregnation is carried out by contacting the support with a solution containing the precursors of the active phases. Two different modes of impregnation are practiced: wet impregnation and incipient-wetness impregnation. In wet impregnation the support material is brought into contact with a large excess of solution containing the metal precursors; after filtration and reduction, the final catalyst is obtained. In general, wet impregnation results in large particles since the majority of the metal precursor is present in the solution outside the pore system of the support. During drying the metal precursors often deposit on the outer surface of the support particles, resulting in large crystals. This method does not permit precise control of the amount of catalyst precursor loaded on the support. Thus, it is likely that some of the catalyst precursor will remain in the liquid phase after filtration.

To make effective use of the pore structure of the support, incipient-wetness impregnation can be performed in which the metal precursor is dissolved in just enough solvent to fill the pores of the support. In that case, closer contact is achieved between the metal precursor and the support, which in general results in smaller particles if reduction is executed carefully. Two major factors govern the final dispersion of the active phase: precursor–support interaction and pore structure. Micropores in the carbon support might be beneficial for metal dispersion. However, during the catalysis reaction these micropores might give rise to diffusion limitations (Serp and Figueiredo, 2009).

5.2.1 Sol deposition Method

NaBH$_4$ (SB) reduction: 50 mM H$_2$PtCl$_6$.6H$_2$O and 4 mL 50 mM sodium citrate were mixed with 120 mL de-ionized water in a 250 ml beaker. 2 mL 0.5 M NaBH$_4$ was added dropwise under vigorous stirring at room temperature. NaBH$_4$ was used in excess for the complete reduction of Pt^{4+} to the elemental state. Stirring continued for 6 h, after that appropriate amount of carbon was added to the Pt sol. The mixture was then ultra-sonicated for 1 h followed by overnight stirring to allow for the equilibrium adsorption of Pt sol on carbon. The solid phase was then recovered by filtration, and washed copiously with water. The recovered solid was then dried at 80 °C overnight (Zeng et al., 2007). CNI-1, NCNI-1 and activated carbon (AC) were used as a support material for

the preparation of NaBH$_4$ reduced Pt catalysts. The obtained carbon supported Pt catalysts were designated as X wt.% Pt/CNI-1 (SB), X wt.% Pt/NCNI-1 (SB), and X wt.% Pt/AC (SB) respectively. Then the prepared catalysts were characterized by XRD, XPS, TEM and CV.

Ethylene Glycol (EG) reduction: 50 mM H$_2$PtCl$_6$.6H$_2$O and 4 mL 50 mM sodium citrate were mixed with 60 mL of ethylene glycol (EG) in a 100 ml beaker. Ethylene glycol was used in excess for the complete reduction of Pt^{4+} to the elemental state. Stirring continued at 120 °C for 4 h in an oil bath. After the reduction, appropriate amount of carbon was added to the Pt sol. The mixture was then ultra-sonicated for 1 h followed by overnight stirring to allow for the equilibrium adsorption of Pt sol on carbon. The solid phase was then recovered by filtration, and washed copiously with water. The recovered solid was then dried at 80 °C overnight. CNI-1, NCNI-1 and AC were used as a support material for the preparation of ethylene glycol reduced Pt catalysts. The obtained carbon supported Pt catalysts were designated as X wt.% Pt/CNI-1 (EG), X wt.% Pt/NCNI-1 (EG), and X wt.% Pt/AC (EG) respectively. Then the prepared catalysts were characterized by XRD, XPS, TEM and CV.

5.2.2 Wet impregnation method

50 mM H$_2$PtCl$_6$.6H$_2$O and 4 mL 50 mM sodium citrate were mixed with 120 mL de-ionized water containing appropriate amount of carbon. After 30 min of sonication, 2 mL 0.5 M of NaBH$_4$ was introduced dropwise to the carbon suspension with vigorous stirring at room temperature. The mixture was then stirred for overnight. The solid phase was recovered by filtration, and washed copiously with water. The recovered solid was then dried at 80 °C overnight (Zeng et al., 2007). Then the prepared catalysts were characterized by XRD.

5.2.3 Incipient-wetness impregnation method

50 mM H$_2$PtCl$_6$.6H$_2$O was mixed with 10 mL de-ionized water containing appropriate amount of carbon. The suspension was evaporated slowly under stirring. Finally solid phase was recovered and reduced under H$_2$ atmosphere at 450° C for 8 h. Then the prepared catalysts were characterized by XRD.

5.3 CHARACTERIZATION

5.3.1 XRD

Fig. 5.1 shows XRD patterns of 10 wt.% Pt/AC prepared by different methods. Fig. 5.2 shows XRD patterns of 10 wt.% Pt/(CNI-1/NCNI-1) prepared by sol method using SB as a reducing agent. 10 wt.% Pt supported on activated carbon and CNI-1/NCNI-1 had been done for the optimization process. The broad diffraction peak observed on carbon supported Pt catalysts at around 25° was corresponding to the carbon. The diffraction peaks at about 39°, 46°, 67° and 81° were from the Pt (1 1 1), (2 0 0), (2 2 0) and (3 1 1) planes, respectively (JCPDS file No. 87-0647). The crystallite sizes of Pt, calculated from the Pt (1 1 1) diffraction peak by means of Scherrer equation, for 10 wt.% Pt/AC prepared by incipient-wetness, wet impregnation and sol methods were 11.8, 4.5 and 4.6 nm, respectively (Table 5.1).
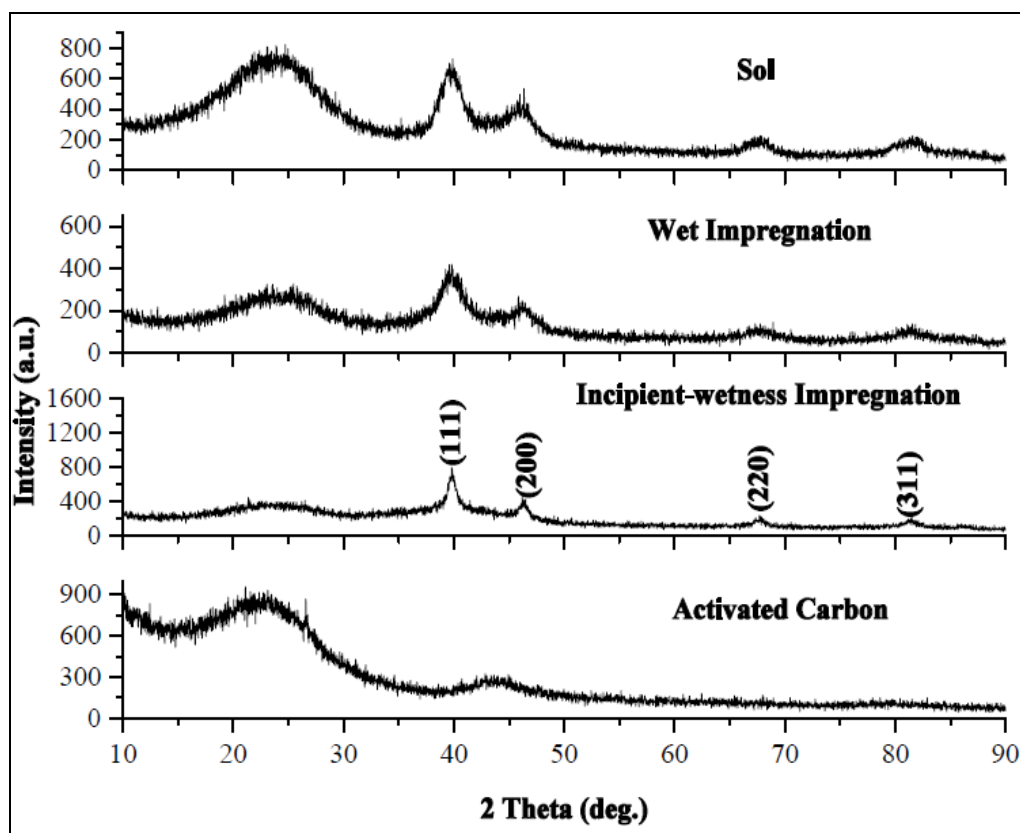
Figure 5.1: XRD patterns of 10 wt.% Pt/AC prepared by different methods.
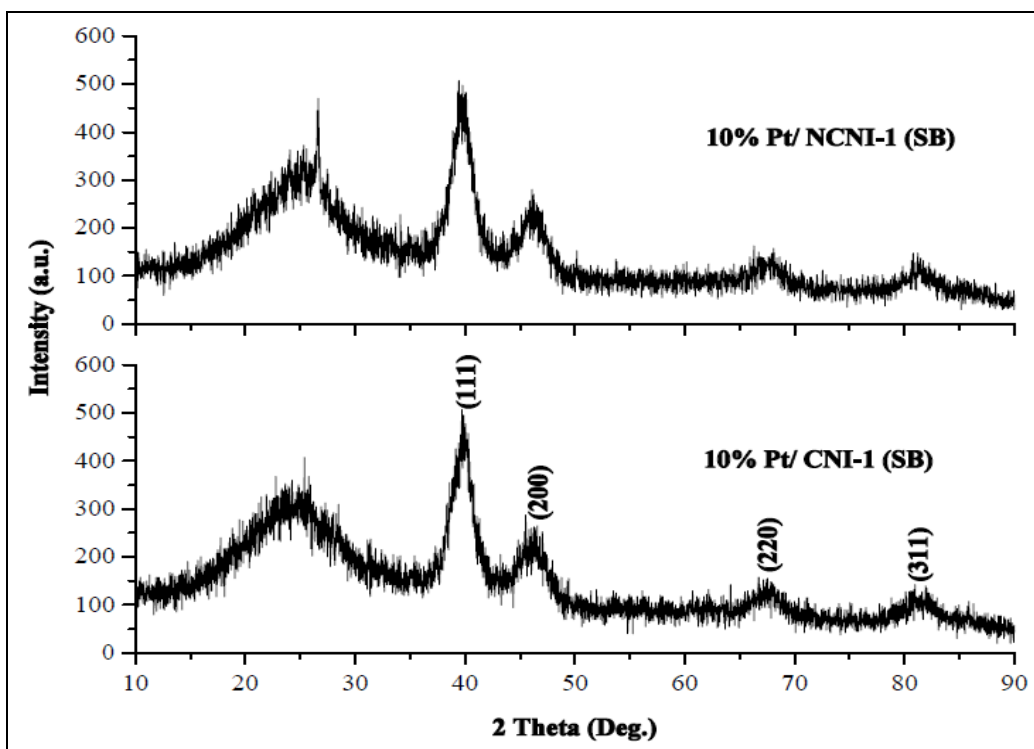
Figure 5.2: XRD patterns of 10 wt.%Pt/ (CNI-1/NCNI-1) prepared by sol method using SB as a reducing agent.

The carbon supported Pt catalyst prepared by incipient-wetness method showed the higher crystallite size because of high temperature reduction process. Therefore, we can conclude that the incipient-wetness was not a suitable method for the preparation of carbon supported Pt catalyst. Even though, Pt catalysts prepared by both the wet impregnation and sol method resulted the similar crystallite size, we preferred sol as a best method. Because in the latter case, size of the sol controls the crystallite size, while in the former case, precipitation capacity of the Pt nanoparticles plays the major role in controlling the crystallite size. The crystallite sizes of Pt, for 10 wt.% Pt/CNI-1 (SB) and 10 wt.% Pt/NCNI-1 (SB) prepared by sol method were 4.3 and 4.5 nm, respectively (Table 5.2). The lattice constant value of ~ 0.39 nm correlates well with the *fcc* lattice of Pt metal supported on carbon materials (JCPDS file No. 87-0647). The lattice constant value of Pt metal is (0.3923 nm) (Liu et al., 2004).
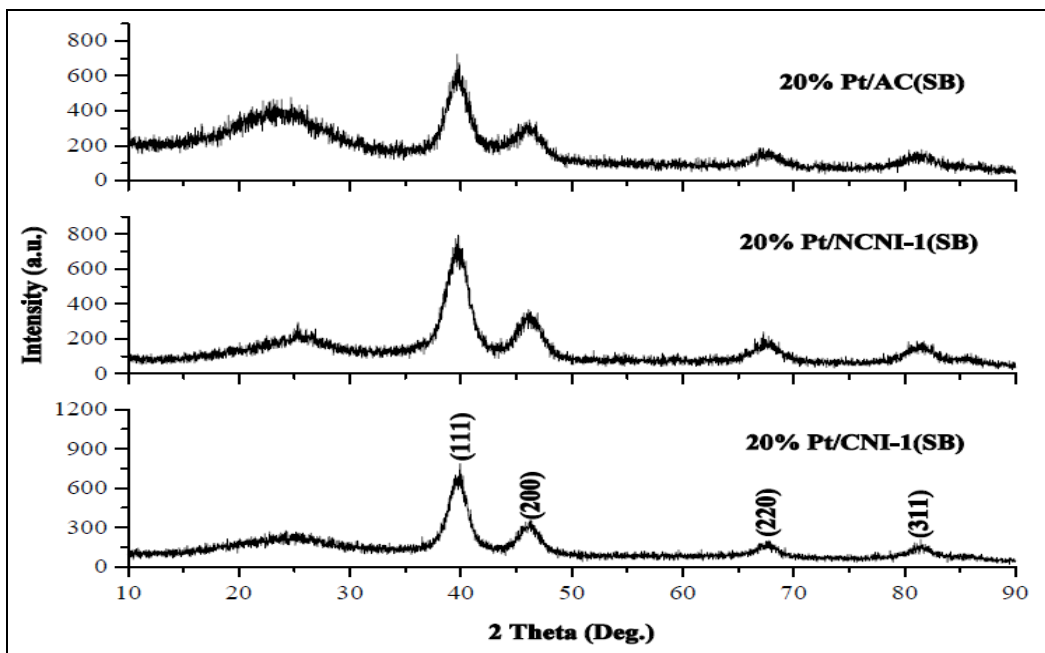
Figure 5.3: XRD patterns of 20 wt.% Pt supported on CNI-1, NCNI-1 and AC prepared by sol method using SB as a reducing agent.
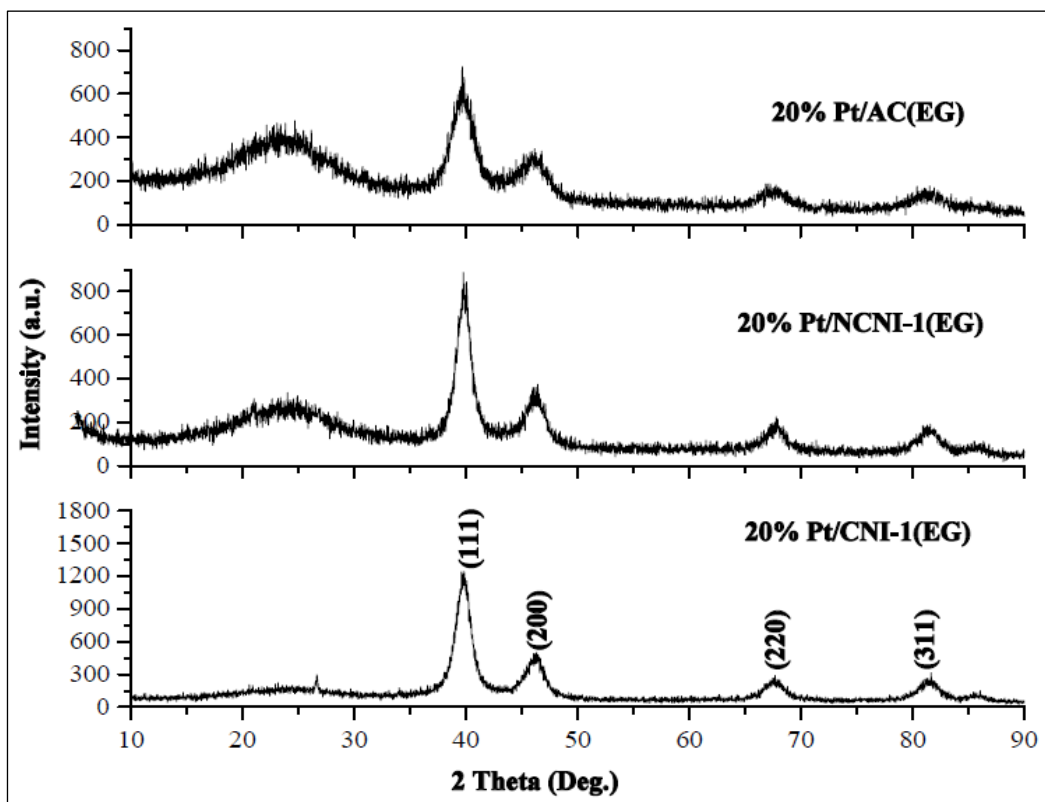
Figure 5.4: XRD patterns of 20 wt.% Pt supported on CNI-1, NCNI-1 and AC prepared by sol method using EG as a reducing agent.

Fig. 5.3 and 5.4 shows XRD patterns of 20 wt.% Pt supported on various carbons (CNI-1, NCNI-1 and AC) prepared by sol method using SB and EG as reducing agent, respectively. The broad diffraction peak observed on carbon supported Pt catalysts at around 25° was corresponding to the carbon. The diffraction peaks at about 39°, 46°, 67° and 81° were from the Pt (1 1 1), (2 0 0), (2 2 0) and (3 1 1) planes, respectively (JCPDS file No. 87-0647). The crystallite sizes of carbon supported Pt catalysts were calculated from the Pt (1 1 1) diffraction peak by means of Scherrer equation. The crystallite size values of those catalysts were tabulated (Table 5.2).

Table 5.1: Effect of preparation method on the crystallite size of the activated carbon supported Pt.

10 wt.% Pt/AC Preparation methods	Reducing Medium	Pt Lattice Constant (nm)	Pt Crystallite Size (nm)
Incipient-Wetness Impregnation	H_2	0.3911	11.8
Wet Impregnation	$NaBH_4$	0.3916	4.5
Sol	$NaBH_4$	0.3912	4.6

Table 5.2: Effect of reducing agent and platinum loading on the crystallite size of the carbon supported.

Catalysts	Pt Lattice Constant (nm)	Pt Crystallite Size (nm)
20 wt.% Pt/CNI-1 (SB)	0.3918	4.8
20 wt.% Pt/NCNI-1 (SB)	0.3923	4.0
20 wt.% Pt/AC (SB)	0.3919	4.4
20 wt.% Pt/CNI-1 (EG)	0.3919	6.0
20 wt.% Pt/NCNI-1 (EG)	0.3907	6.2
20 wt.% Pt/AC (EG)	0.3918	6.4
10 wt.% Pt/CNI-1 (SB)	0.3910	4.3
10 wt.% Pt/NCNI-1 (SB)	0.3917	4.5
40 wt.% Pt/E-TEK	0.3909	3.9

SB reduced Pt catalysts showed lower crystallite size (~ 4 nm) compare to EG reduced Pt catalysts (~ 6 nm) (Table 5.2). In the case of EG reduced Pt catalysts, nature of the carbon support was not showing any significant difference in the crystallite size.

5.3.2 TEM

Fig. 5.5 shows the TEM, Electron diffraction images and Fig. 5.6 shows the particle size distribution of CNI-1/NCNI-1 supported Pt catalysts. Fig 5.5a and 5.6a show that the Pt nanoparticles in the 10 wt.% Pt/NCNI-1 (SB) had an average particle size of 3.9 nm ($\sigma = 0.6$ nm), and were lightly agglomerated despite electrostatic stabilization by the adsorbed citrate ions due to presence of nitrogen in the NCNI-1 matrix.
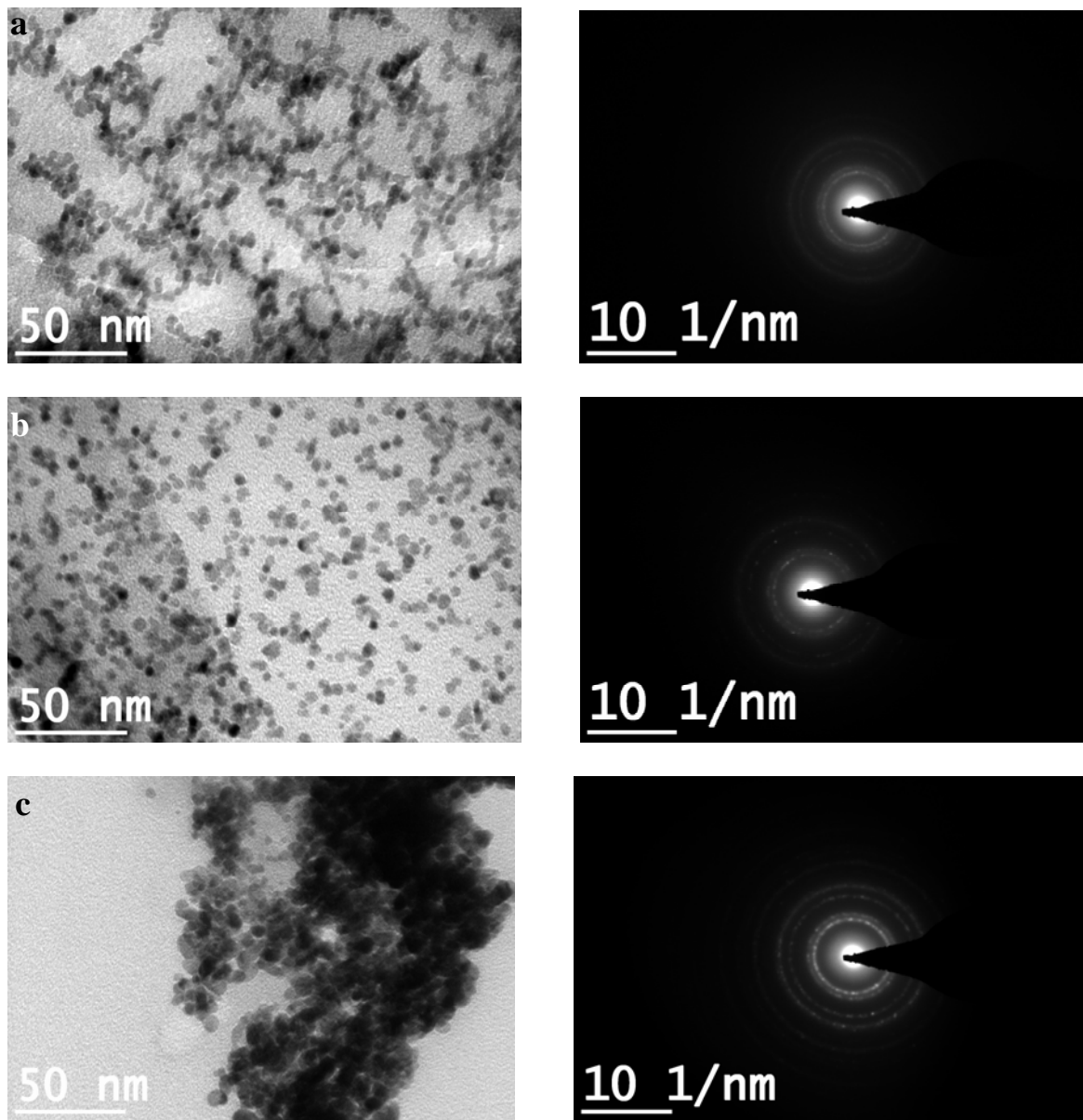
Figure 5.5: TEM and ED of: (a) 10 wt.% Pt/NCNI-1 (SB); (b) 20 wt.% Pt/CNI-1 (SB); (c) 20 wt.% Pt/CNI-1 (EG).

Fig 5.5b and 5.6b show that the Pt nanoparticles in the 20 wt.% Pt/CNI-1 (SB) had an average particle size of 4.39 nm ($\sigma = 0.86$ nm), and were highly dispersed. Fig 5.5c shows the TEM image of Pt nanoparticles in the 20 wt.% Pt/CNI-1 (EG), and were highly agglomerated compare to SB reduced catalysts. EG reduced catalyst was having higher particle size compare to SB reduced catalysts. This is also validating the XRD results.
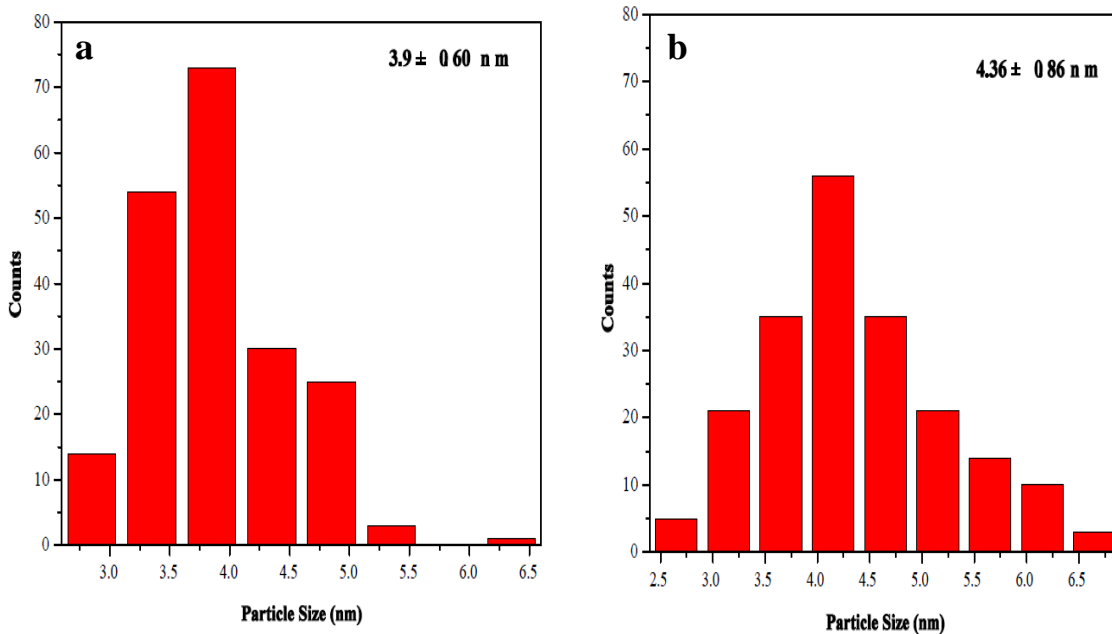
Figure 5.6: Histogram of the Pt nanoparticles supported on carbon catalysts
(a) 10 wt.% Pt/NCNI-1 (SB); (b) 20 wt.% Pt/CNI-1 (SB)

5.3.3 XPS

Fig 5.7 shows survey spectra of (a) 20 wt.% Pt/AC (EG) (b) 20 wt.% Pt/CNI-1 (SB) in XPS. In the survey spectra, there are peaks of Pt 4f, C 1s, Pt 4d, Pt 4p, and O 1s are common in all the carbon supported Pt catalysts.
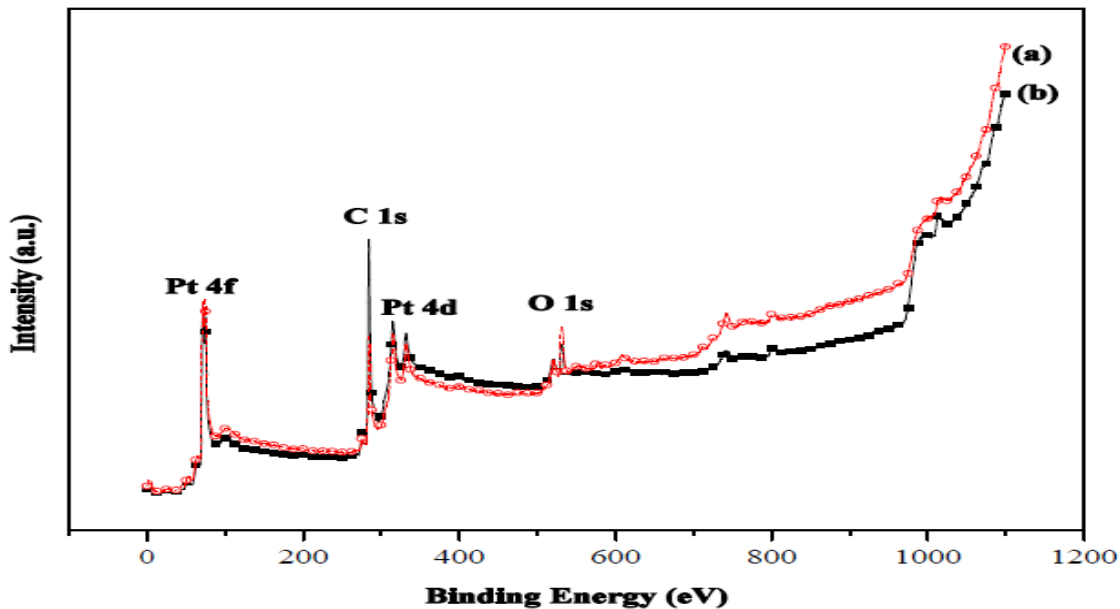
Figure 5.7: Survey XPS spectra of (a) 20 wt.% Pt/AC (EG) (b) 20 wt.% Pt/CNI-1 (SB)

Fig. 5.8 shows survey spectra of (a) 10 wt.% Pt/NCNI-1 (SB) (b) 10 wt.% Pt/CNI-1 (SB) in XPS. In the survey spectra, there are peaks of Pt 4f, C 1s, Pt 4d and O 1s are common in all the carbon supported Pt catalysts. Anyhow, N 1s peak (399.8 eV) in survey XPS spectrum showed the presence of nitrogen only in the 10 wt. %Pt/NCNI-1 (SB) and not in10 wt.% Pt/CNI-1 (SB). This obvious difference was due to the presence of nitrogen in the NCNI-1 matrix.
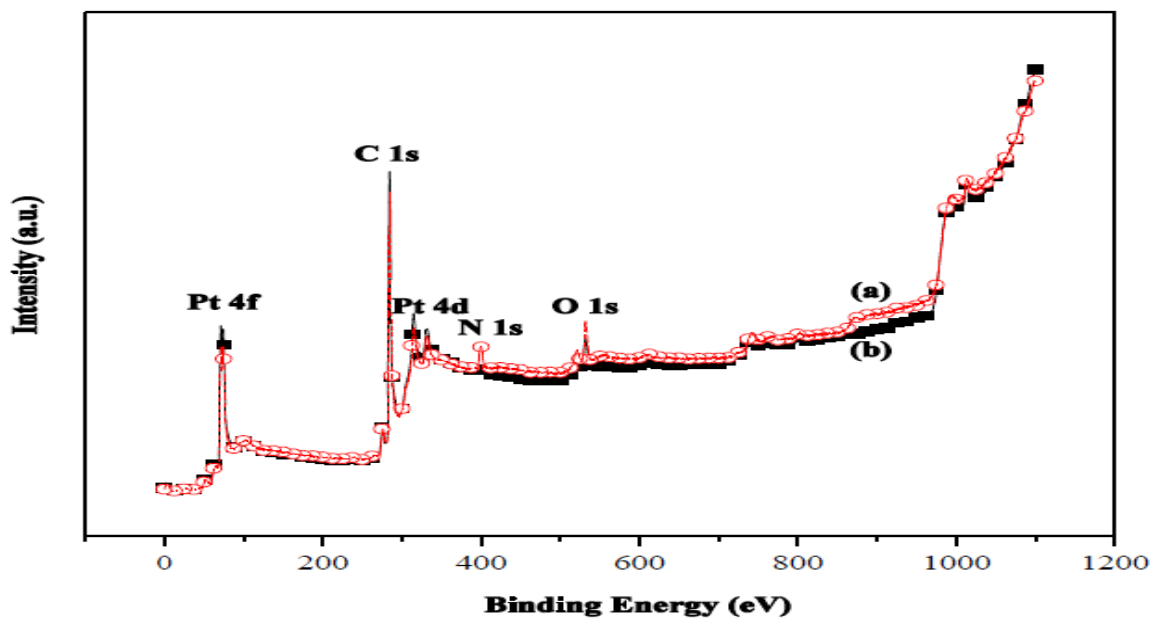
Figure 5.8: Survey XPS spectra of (a) 10 wt.% Pt/NCNI-1 (SB) (b) 10 wt.% Pt/CNI-1 (SB).
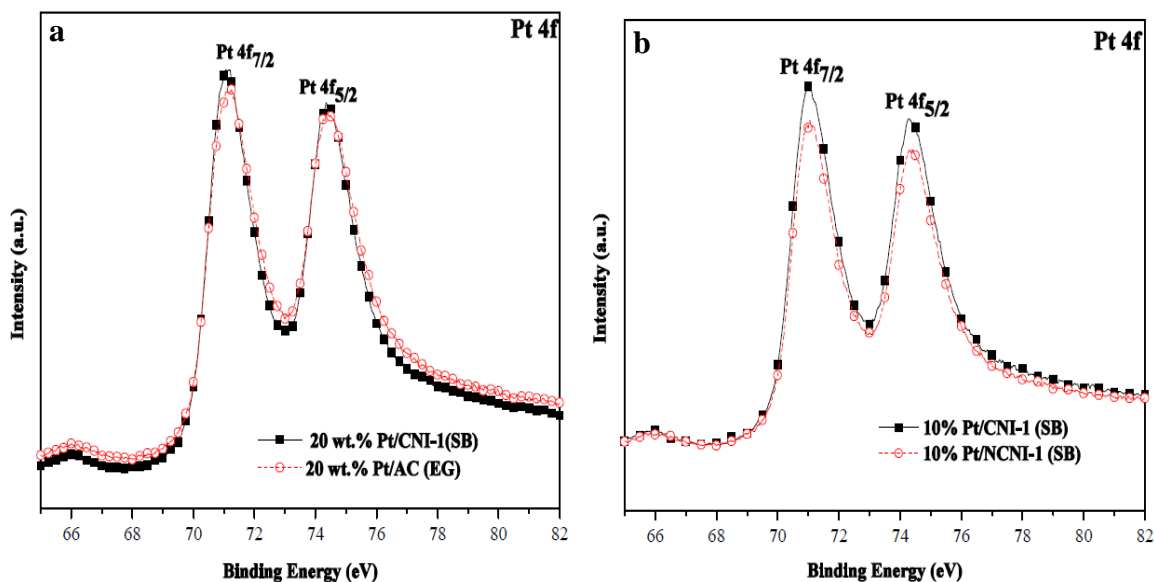
Figure 5.9: XPS spectra of Pt 4f of (a) 20 wt.% Pt/C (b) 10 wt.% Pt/C

Fig 5.9a and 5.9b show the XPS of Pt 4f spectrum for the 20 wt.% Pt/C and 10 wt.% Pt/C prepared by sol method, respectively. The Pt 4f spectrum shows a doublet containing a low-energy band (Pt 4f $_{7/2}$) and a high energy band (Pt 4f $_{5/2}$) at 71.2 and 74.6 eV, respectively. These binding energy values are in good agreement with the literature data for Pt (Hufner and Wertheim, 1975). These peaks indicated that Pt is present in metallic state, Pt (0).
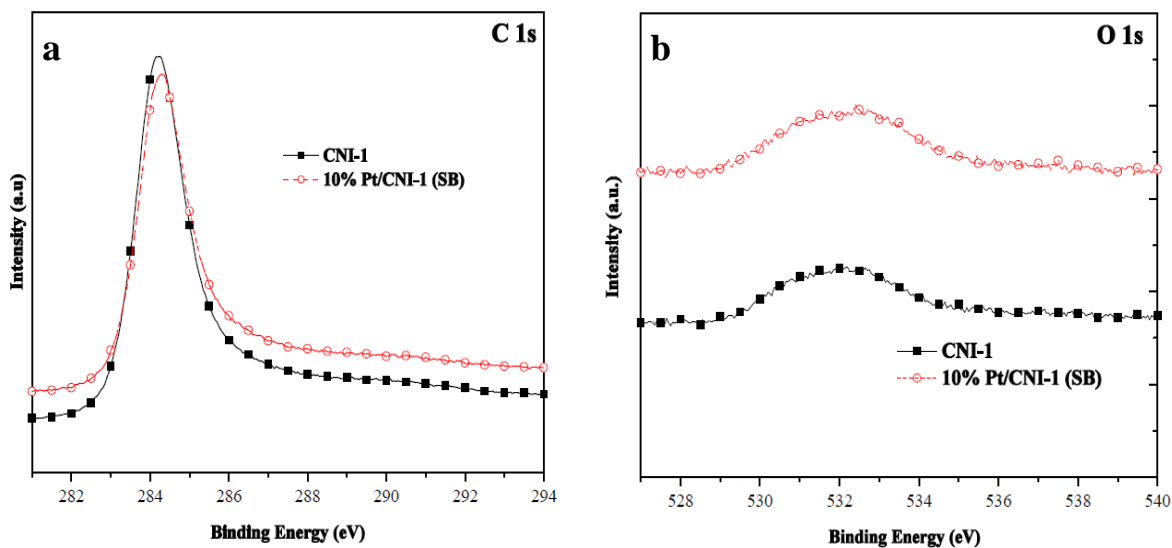
Figure 5.10: XPS spectra of CNI-1 and 10 wt.% Pt/CNI-1 (SB) (a) C (1s); (b) O (1s)

49

Both C 1s spectra and O 1s spectra of 10 wt.% Pt/CNI-1 (SB) had a more positive binding energy value compared to CNI-1 (Fig. 5.10a and 5.10b). The peak position of C 1s for CNI-1 and 10 wt.% Pt/CNI-1 (SB) were 284.2 and 284.3 eV, respectively. The peak position of O 1s for CNI-1 and 10 wt.% Pt/CNI-1 (SB) were 532.0 and 532.5 eV, respectively.
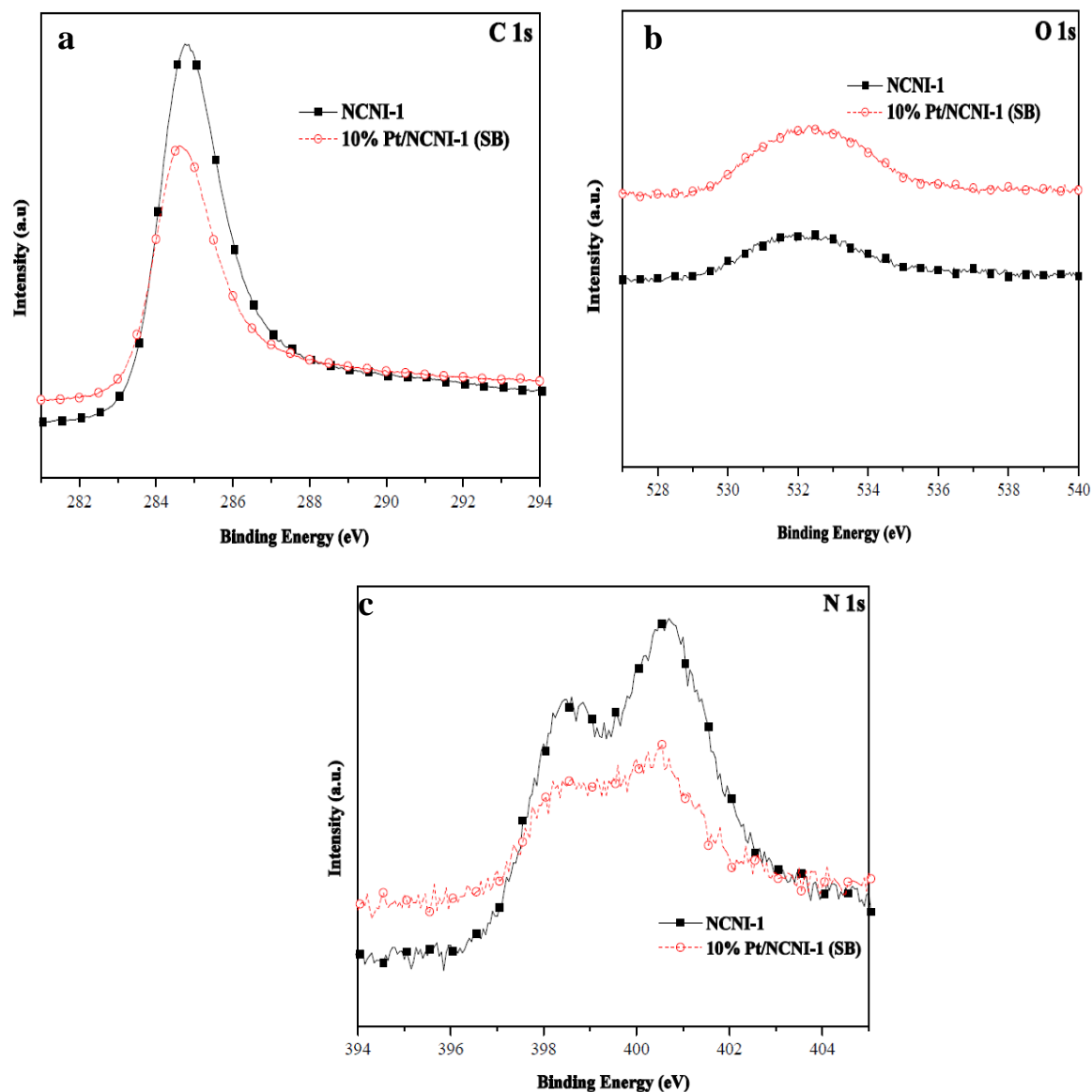
Figure 5.11: XPS spectra of NCNI-1 and 10 wt.% Pt/NCNI-1 (SB) (a) C (1s); (b) O (1s); (c) N (1s)

C 1s spectra of 10 wt.% Pt/NCNI-1 (SB) have a more negative binding energy value compared to NCNI-1 in Fig 5.11a. The main peak position of C 1s is 284.8 eV, 284.6 eV at the NCNI-1 and 10 wt.%Pt/NCNI-1 (SB), respectively. The shift in the C 1s peak is mainly due to the C-N coordination. O 1s spectra of 10 wt.% Pt/NCNI-1 (SB) have a more positive binding energy value compared to NCNI-1 in Fig 5.11b. The main peak position of O 1s is 532.1 eV, 532.4 eV at the NCNI-1 and 10 wt.% Pt/NCNI-1 (SB), respectively. N 1s spectra of 10 wt.% Pt/NCNI-1 (SB) have a more negative binding energy value compared to NCNI-1(Fig. 5.11c). N 1s spectrum was deconvoluted with three types of nitrogen. Peaks at 398.5, 400.5, and 401.4 eV were attributed to pyridinic, pyrrolic, and quaternary nitrogen, respectively. Peak of pyrrolic kind of nitrogen showed the highest proportion among the deconvoluted peaks (Fig. 4.11). And it can be reason for the higher activity and EAS of nitrogen containing carbon (NCNI-1) supported Pt electrocatalysts.

5.3.4 Electro oxidation of methanol - Cyclic Voltammetry
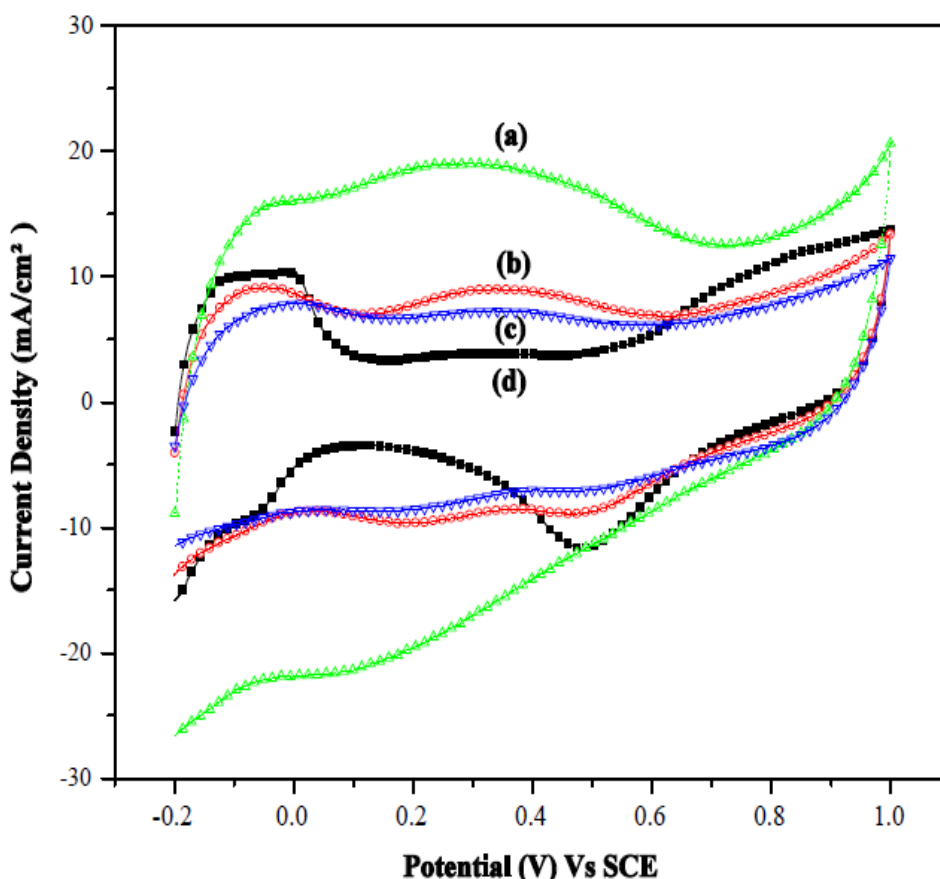
Figure 5.12: Cyclic voltammograms of (a) 20 wt.% Pt/NCNI-1 (SB); (b) 20 wt.% Pt/CNI-1 (SB); (c) 20 wt.% Pt/AC (SB); (d) 40 wt.% Pt/E-TEK measured at a scan rate of 50 mV/s in 1 M H_2SO_4 electrolyte.
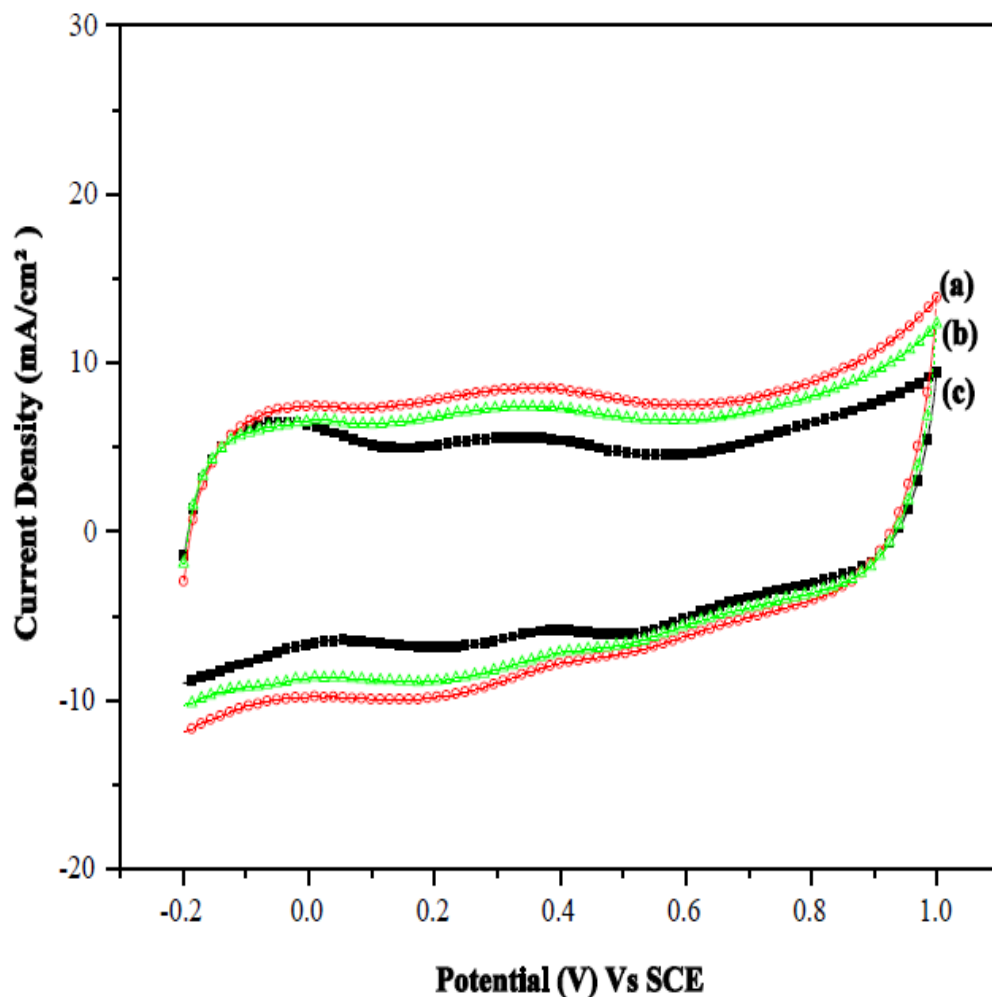
Figure 5.13: Cyclic voltammograms of (a) 20 wt.% Pt/NCNI-1 (EG) (b) 20 wt.% Pt/AC (EG) (c) 20 wt.% Pt/CNI-1 (EG) measured at a scan rate of 50 mV s^{-1} in 1 M H$_2$SO$_4$ electrolyte.

The cyclic voltammograms (CV) for the carbon (Activated Carbon, CNI-1, NCNI-1 and E-TEK) supported Pt catalysts, in 1 M H$_2$SO$_4$ are shown in Fig. 5.12-5.14. The redox couple (+ 0.4 V in the forward scan and + 0.26 V in the backward scan) in the CV of the supported platinum catalysts could arise from surface species on the carbon support. The peak in the reverse scan at + 0.55 V belonged most likely to Pt oxide reduction. The peak potential was the same for all the catalysts indicating that the Pt particles on the carbon support had similar physiochemical attributes (size and composition), validating the XRD measurements. The calculation of electrochemically active surface areas, which is often carried out by integrating the well-resolved peaks in the hydrogen adsorption region, was evaluated. EAS values for all the prepared catalysts were shown in Table 5.6.
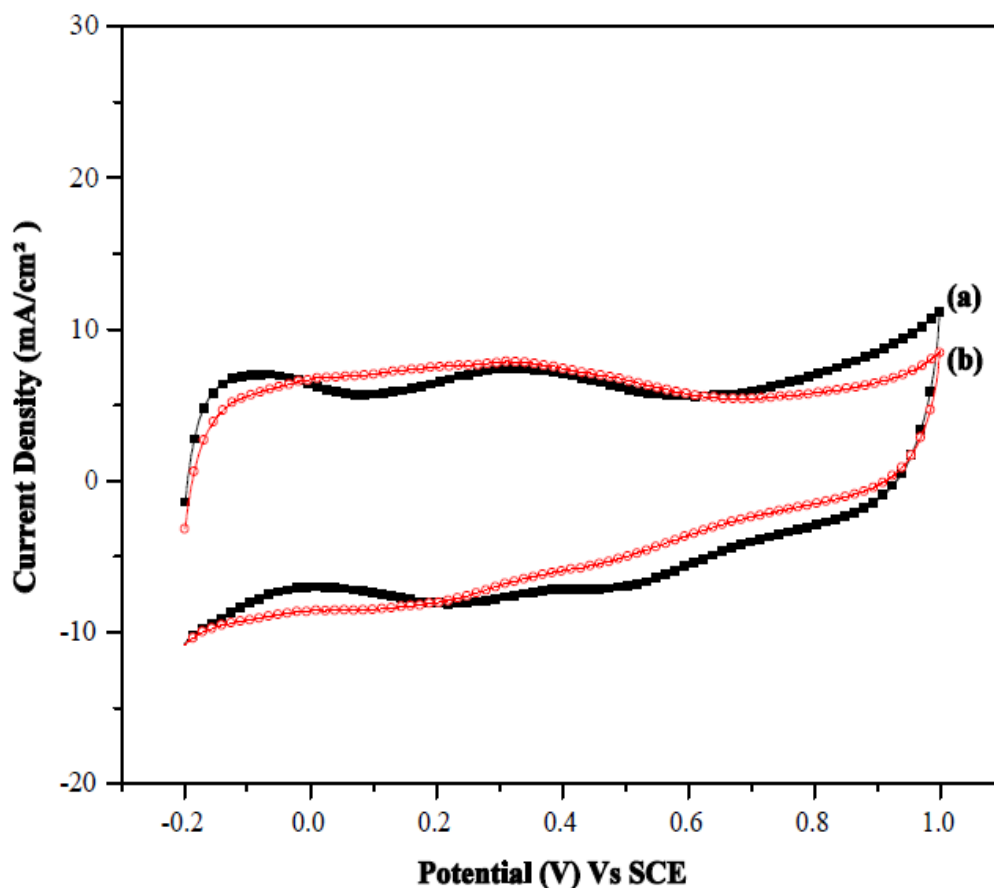
Figure 5.14: Cyclic voltammograms of (a) 10 wt.% Pt/CNI-1 (SB) (b) 10 wt.% Pt/NCNI-1 (SB) measured at a scan rate of 50 mV s^{-1} in 1 M H$_2$SO$_4$ electrolyte.

5.3.5 Evaluation of Mass Specific Activity (MSA) of the prepared catalysts

The cyclic voltammograms recorded with electrodes fabricated using 10 and 20 wt. % Pt supported on carbon material CNI-1, NCNI-1 and AC in 1M H$_2$SO$_4$ and 1M CH$_3$OH are shown in Fig. 5.15-5.17. The feature common to all the cyclic voltammograms is that one anodic peak is observed in the forward scan and another in the reverse scan. The anodic peak in the forward scan is attributed to oxidation of methanol. The anodic peak in the reverse scan is attributed to the removal of the incompletely oxidized carbonaceous species (mostly in the form of linearly bonded Pt=C=O) formed in the forward scan. The critical parameter that determines the usefulness of an electrode is the onset potential. A less positive value of the onset potential is preferred. A lower onset (less positive potential) potential value implies the requirement of lower energy for the

methanol oxidation reaction to take place (Sobkowski *et al*., 1992). The onset potential value is related to the breaking of the C-H bond of methanol which is the primary step involved in the mechanism of oxidation of methanol (Wu *et al*., 2007).
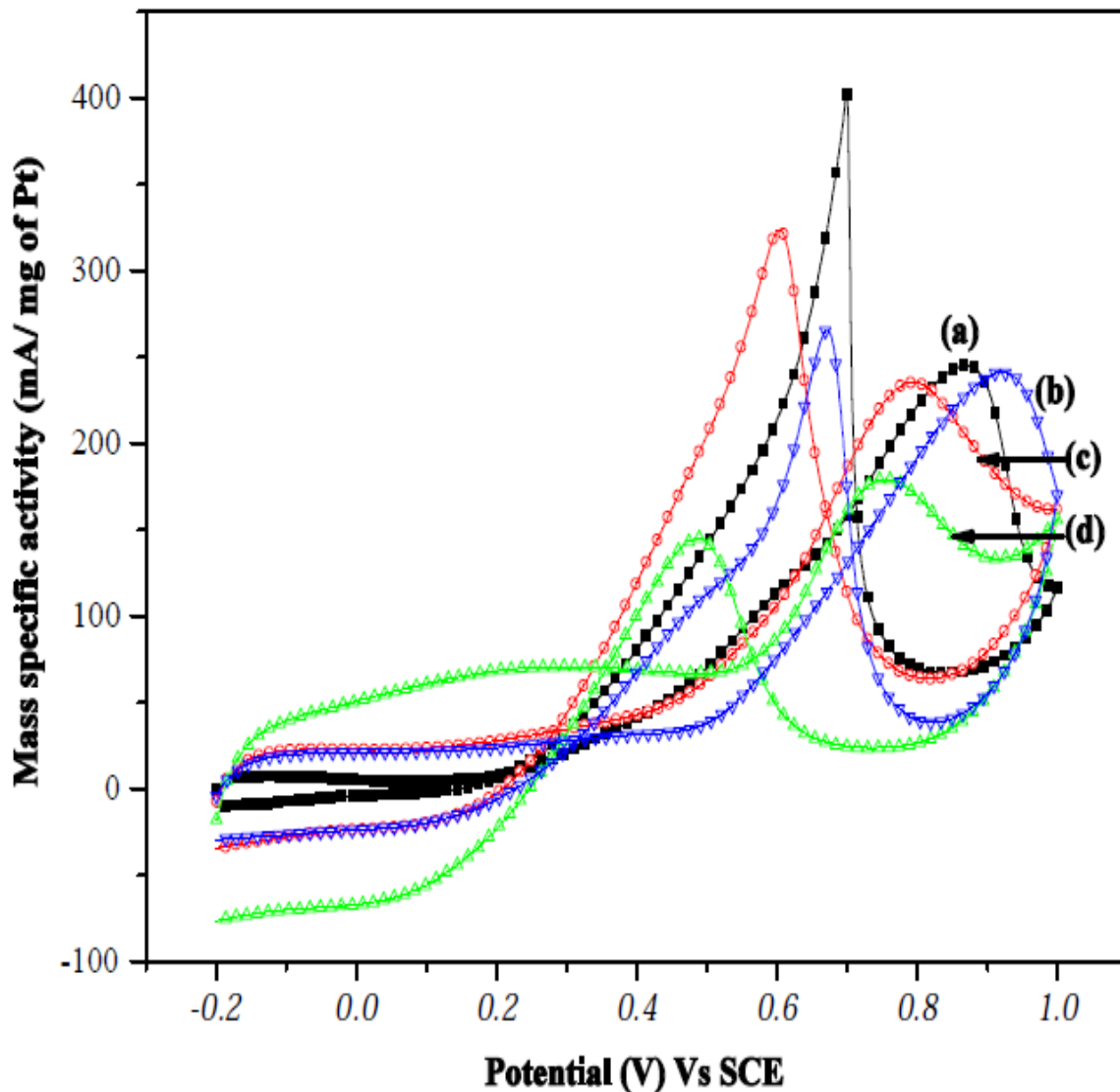
Figure 5.15: MSA of (a) 40 wt.% Pt/E-TEK; (b) 20 wt.% Pt/AC (SB); (c)20 wt.% Pt/CNI-1(SB); (d) 20 wt.% Pt/NCNI-1 (SB) for methanol oxidation reaction.
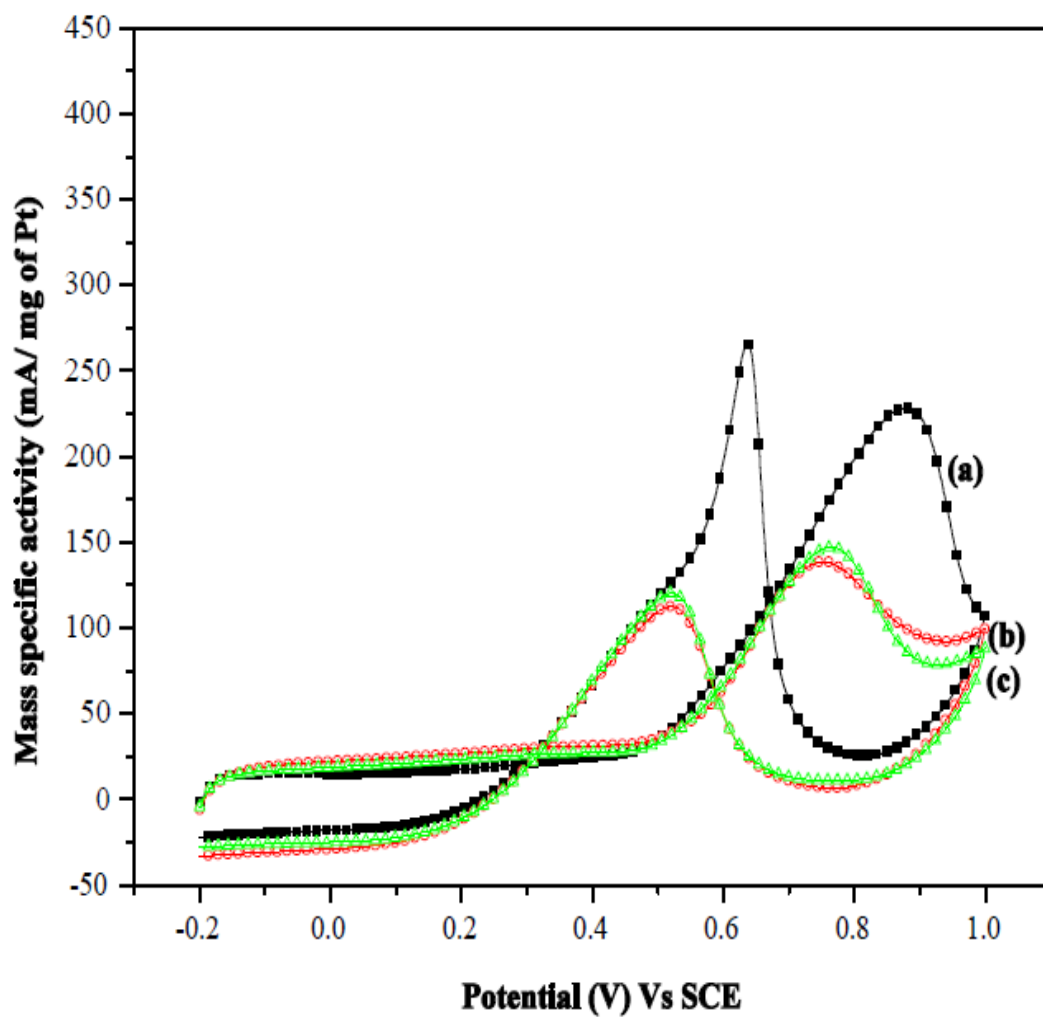
Figure 5.16: MSA of (a) 20 wt.% Pt/CNI-1 (EG); (b) 20 wt.% Pt/NCNI-1 (EG); (c) 20 wt.% Pt/AC (EG) for methanol oxidation reaction in 1 M CH_3OH + 1 M H_2SO_4 at room temperature (scan rate = 50 mV s^{-1}).
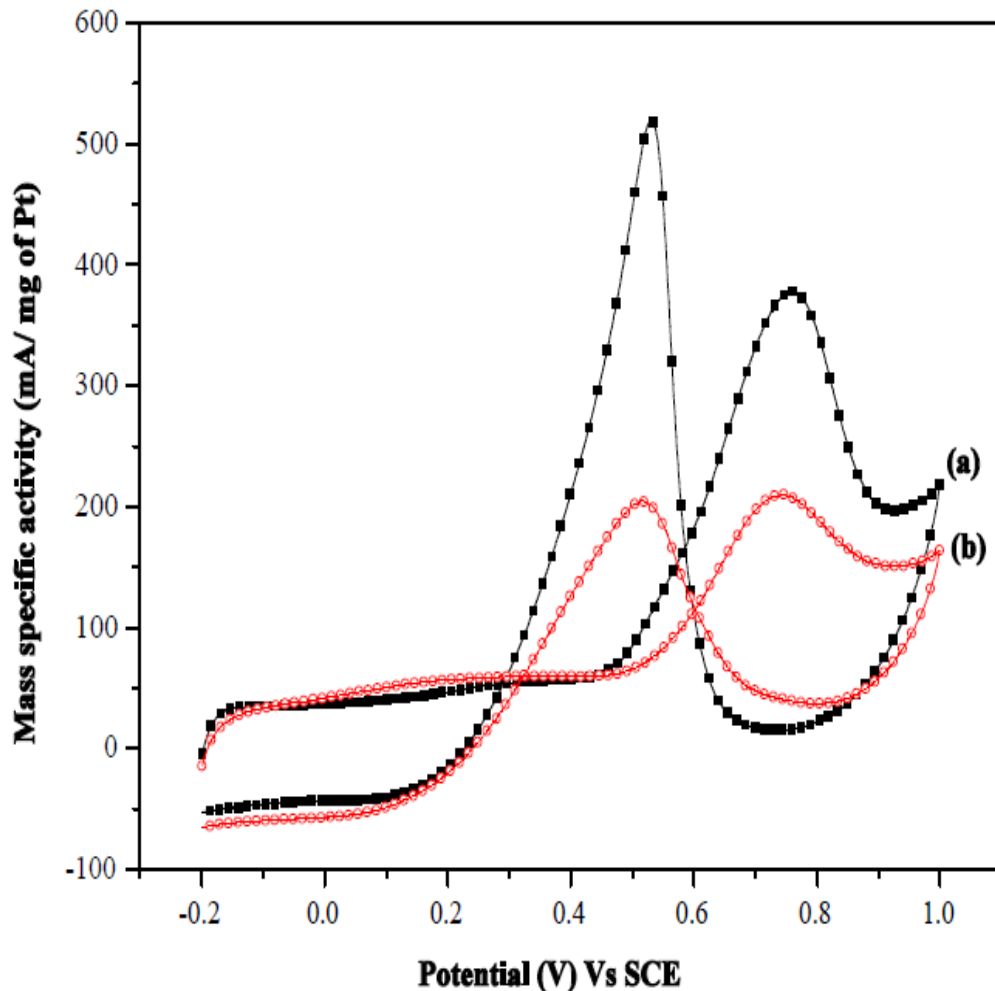
Figure 5.17: MSA of (a) 10 wt.% Pt/CNI-1 (SB); (b) 10 wt.% Pt/NCNI-1 (SB) for methanol oxidation reaction in 1 M CH$_3$OH + 1 M H$_2$SO$_4$ at room temperature (scan rate = 50 mV s^{-1}).

The onset potential values for the electro oxidation of methanol deduced from the cyclic voltammograms obtained over different electrodes, along with peak potential and current values corresponding to the methanol oxidation (anodic peak in the forward sweep) as well as the oxidation of the intermediate species formed during the oxidation of methanol (anodic peak in the reverse sweep) are summarized in Table 5.5. Liu *et al.*, (2004) have reported the onset potential values of 0.27 V and 0.28 V, respectively, on Pt/Vulcan XC 72 R and Pt/CNTs for the electro oxidation of methanol in 1 M H$_2$SO$_4$ and 2 M CH$_3$OH at a scan rate of 50 mV/sec. Kuppan et al., (2011) have reported the onset potential and i$_f$/i$_b$ values of 0.33 V and 0.72, respectively for 20 wt.% Pt/E-TEK (Table 5.3). 20 wt.% Pt/CNI-1 (SB) exhibited lower onset potential and higher i$_f$/i$_b$, compare to commercial E-TEK catalyst. Mass specific activity and specific activity values of

all the prepared Pt catalysts at + 0.7 V were tabulated (Table 5.6). 20 wt.% Pt/CNI-1 (SB) catalyst showed lower onset potential (0.20 V) than the commercial 40 wt.% Pt/E-TEK(0.23 V). And also, it showed a higher MSA which is an indication of higher electrochemical catalytic activity. Such a high MSA value derivable from the modest wt.% loading of Pt is an indication of the effective utilization of Pt over the CNI-1 support. The improved performance of the electrocatalyst, 20 wt.% Pt/CNI-1 (SB) can be attributed to the smaller Pt nano crystallites (4.36 nm) finely dispersed over the carbon support and higher EAS. The ratio of the anodic peak current densities in the forward (i_f) and reverse (i_b) scans too gives a measure of the catalytic performance. A higher i_f/i_b ratio indicates superior oxidation activity of methanol during the anodic scan and less accumulation of carbonaceous species on the nano catalyst surface and thus an indication of better CO tolerance. All the prepared Pt catalysts show higher i_f/i_b compared to commercial Pt catalysts (Table 5.3). For comparison, Lei *et al*., (2009) have evaluated the performance of 20 wt. % Pt/Vulcan XC 72 under identical conditions and observed an i_f/i_b value of 0.89.

Table 5.3: Effect of Pt loading and the nature of the carbon support on the electrocatalytic activity of methanol oxidation of Pt/CNI-1, Pt/NCNI-1 and Pt/AC.

Catalysts	Onset Potential, V	i_f/i_b	Activity*			
			Forward sweep		Reverse sweep	
			I (mA/cm²)	E (V)	I (mA/cm²)	E (V)
20 wt.% Pt/CNI-1 (SB)	0.20	0.73	67.29	0.80	92.29	0.61
20 wt.% Pt/NCNI-1 (SB)	0.35	1.24	51.43	0.76	41.43	0.49
20 wt.% Pt/AC (SB)	0.34	0.91	68.86	0.92	75.86	0.67
20 wt.% Pt/CNI-1 (EG)	0.32	0.86	65.43	0.88	75.86	0.64
20 wt.% Pt/NCNI-1 (EG)	0.37	1.23	39.57	0.74	32.14	0.52
20 wt.% Pt/AC (EG)	0.39	1.23	42.00	0.76	34.29	0.53
10 wt.% Pt/CNI-1 (SB)	0.38	0.73	54.00	0.76	74.29	0.53
10 wt.% Pt/NCNI-1 (SB)	0.34	1.02	30.00	0.74	29.29	0.52
20% Pt/E-TEK	0.33	0.72	36.57	0.78	50.00	0.72
40% Pt/E-TEK	0.23	0.61	140.00	0.87	229.86	0.70

*Activity evaluated in 1 M H_2SO_4 and 1 M CH_3OH, at a scan rate of 50 mV/sec between -0.2 to + 1.0 V Vs SCE.

Table 5.4: Effect of Pt loading and the nature of the carbon support on the EAS, MSA and SA of methanol oxidation of Pt/CNI-1, Pt/NCNI-1 and Pt/AC at +0.7 V.

Catalysts	EAS (m^2/g)	MSA (mA/mg of Pt) at 0.7 V	SA (A/m² of Pt) at 0.7 V
20 wt.% Pt/CNI-1 (SB)	98.2	186.01	1.89
20 wt.% Pt/NCNI-1 (SB)	191.9	161.01	0.84
20 wt.% Pt/AC (SB)	88.3	131.01	1.48
20 wt.% Pt/CNI-1 (EG)	71.8	133.51	1.86
20 wt.% Pt/NCNI-1 (EG)	94.3	125.51	1.33
20 wt.% Pt/AC (EG)	79.4	126.51	1.59
10 wt.% Pt/CNI-1 (SB)	159.1	331.9	2.09
10 wt.% Pt/NCNI-1 (SB)	111.3	196.94	1.77
40 wt.% Pt/E-TEK	42.6	158.26	3.72

5.3.6 Methanol Electro Oxidation – Effect of Scan Rate

The effect of scan rate on the electrochemical performance (current out put) of different electrodes, at the scan rates of 25, 50, 75 and 100 mV/sec in 1 M H_2SO_4 and 1 M CH_3OH between − 0.2 to + 1.0 V Vs SCE was evaluated.
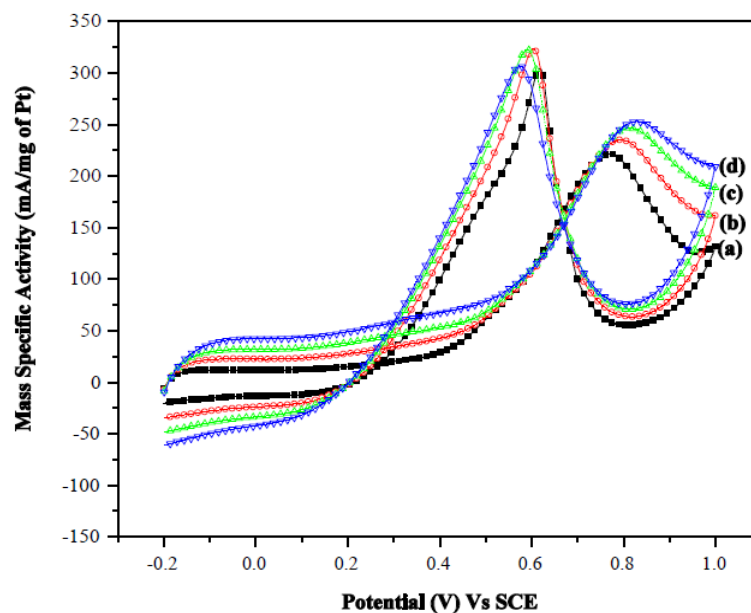

Figure 5.18: Cyclic voltammograms of 20 wt.% Pt/CNI-1 (SB) at different scan rates ((a) 25 mV/s; (b)50 mV/s; (c) 75 mV/s; (d) 100 mV/s) in 1 M CH_3OH and 1 M H_2SO_4.

58
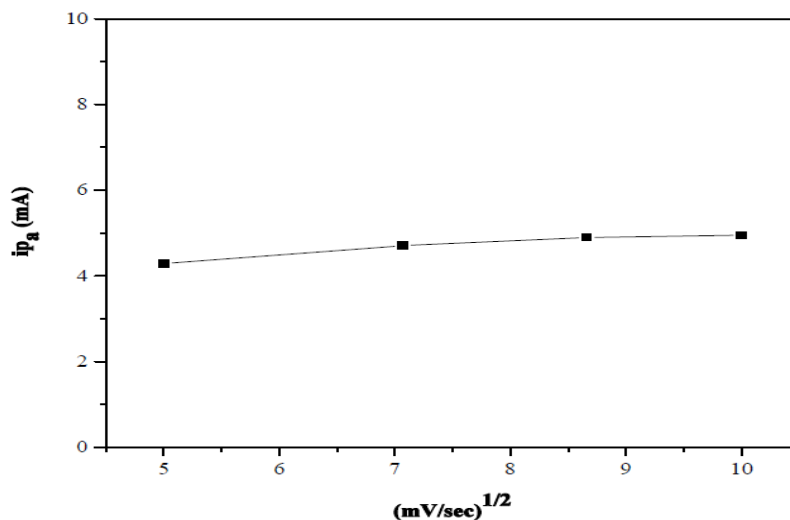
Figure 5.19: Dependence of the peak currents on the square root of scan rates for 20 wt.% Pt/CNI-1 (SB).

It was observed that the MSA values due to the methanol oxidation increased as the scan rate increased from 25 to 100 mV/s. A small increment in the peak potential with an increase in the scan rate was also observed (Fig. 5.18). The peak currents were found to be linearly proportional to the square root of scan rates as shown in Fig. 5.19. Such a linear proportionality relationship between the current response and square root of scan rate indicates that the oxidation process of methanol is controlled by diffusion (Wang *et al*., 2006). For all other electrocatalysts the effect of scan rate on the MSA and dependence of the peak currents on the square root of scan rates, figures were shown in appendix D.

5.3.7 Evaluation of stability of the electrodes for Methanol oxidation by Chronoamperometry

The stability of the electrode under potentiostatic conditions is essential for oxidation of methanol for the possible application in DMFC. The stability of the fabricated electrodes was evaluated by chronoamperometric studies carried out for a duration of 0.5 h with the electrode being polarized at + 0.7 V Vs SCE in 1 M H_2SO_4 and 1 M CH_3OH. The MSA Vs time plots derived from the fabricated electrodes are shown in Fig. 5.17-5.19. There was a constant decay in the mass specific activity with respect to time, possibly suggesting the poisoning of the electrodes by CO. The initial and final (after 0.5 h) MSA values derivable from the electrodes fabricated from 20 wt.% Pt/C (SB), 20 wt.% Pt/C (EG) and 10 wt.% Pt/TMC (SB) catalysts are summarized in

Table 5.4. The percentage decrease of the activity of the aforementioned electrodes after 0.5 h was also shown in Table 5.4.

Figure 5.20: Chronoamperometry of (a) 40 wt.% Pt/E-TEK; (b) 20 wt.% Pt/CNI-1 (SB); (c) 20 wt.% Pt/AC (SB); (d) 20 wt.% Pt/NCNI-1 (SB) for methanol oxidation reaction in 1 M CH$_3$OH + 1 M H$_2$SO$_4$ at room temperature.

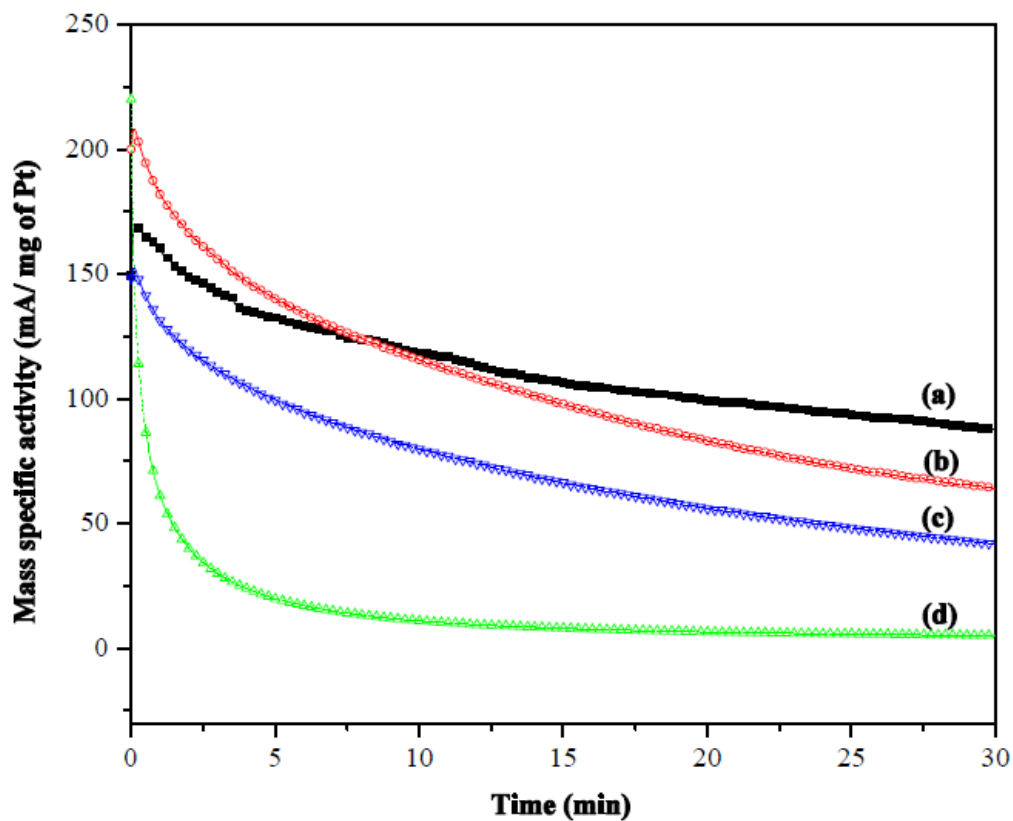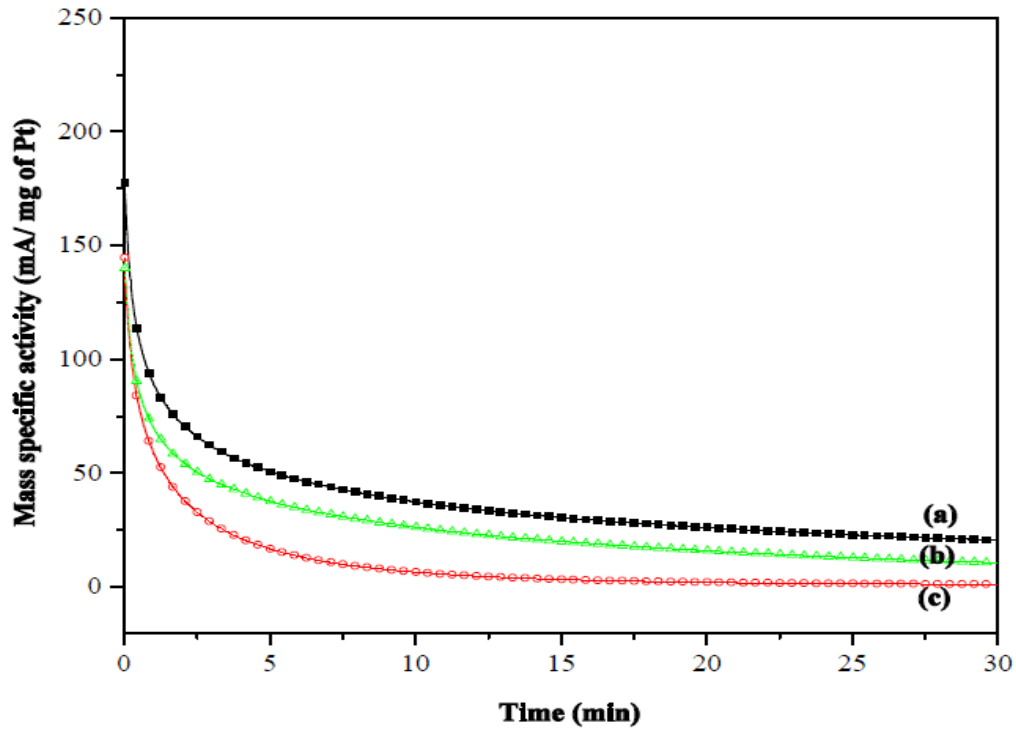**Figure 5.21:** Chronoamperometry of (a) 20 wt.% Pt/CNI-1 (EG); (b) 20 wt.% Pt/AC (EG); (c) 20 wt.% Pt/NCNI-1 (EG) for methanol oxidation reaction in 1 M CH$_3$OH + 1 M H$_2$SO$_4$ at room temperature.
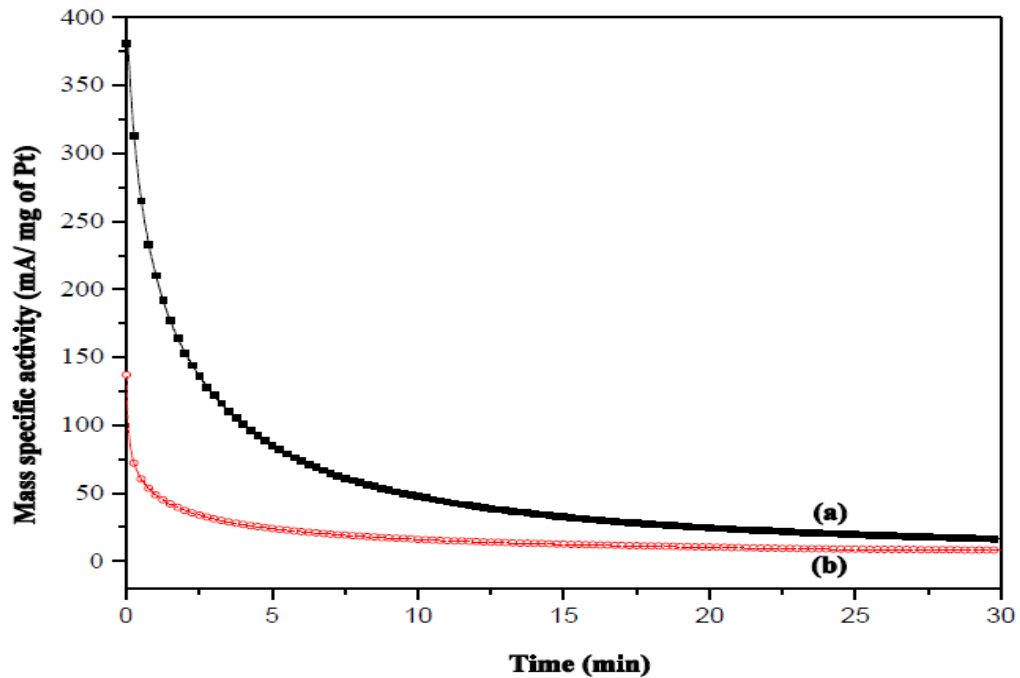
Figure 5.22: Chronoamperometry of (a) 10 wt.% Pt/CNI-1 (SB) (b) 10 wt.% Pt/NCNI-1 (SB) for methanol oxidation reaction in 1 M CH$_3$OH + 1 M H$_2$SO$_4$ at room temperature.

Table 5.5: Effect of Pt loading and the nature of the carbon support on the catalytic stability for methanol oxidation of Pt/CNI-1, Pt/NCNI-1 and Pt/AC by chronoamperometry.

Catalysts	MSA*		% Decrease in activity after 0.5 h + 0.7 V
	Initial (I), mA/mg of Pt	Final (I), mA/mg of Pt	
20 wt.% Pt/CNI-1 (SB)	200.01	64.00	68
20 wt.% Pt/NCNI-1 (SB)	220.01	05.13	98
20 wt.% Pt/AC (SB)	148.51	41.83	72
20 wt.% Pt/CNI-1 (EG)	177.51	20.47	88
20 wt.% Pt/NCNI-1 (EG)	144.51	01.16	99
20 wt.% Pt/AC (EG)	140.01	10.70	92
10 wt.% Pt/CNI-1 (SB)	380.89	16.15	96
10 wt.% Pt/NCNI-1 (SB)	136.96	07.88	94
40 wt.% Pt/E-TEK	149.26	87.75	41

* MSA evaluated in 1 M H_2SO_4 and 1 M CH_3OH for 0.5 h with the electrode being polarized at + 0.7 V Vs SCE.

Among the electrodes studied, the 20 wt.% Pt/NCNI-1 (SB) and 20 wt.% Pt/NCNI-1 (EG) catalysts based electrodes showed least stability with a 98-99 % decrease of initial activity at the end of 0.5 h. As expected, the electrode fabricated using 20 wt.% Pt/CNI-1 (SB) possessing the smaller Pt crystallites (4.36 nm) as well as high i_f/i_b ratio showed highest stability. And also, it showed only 68 % loss of activity at the end of 0.5 h. Thus, it is clear that the stability of the electrode is based on the smaller crystallite size of Pt as well as the high CO tolerance (high i_f/i_b ratio value).

CHAPTER 6

SUMMARY AND CONCLUSIONS

Templated microporous carbon (CNI-1) with a S_{BET} (409 m²/g) and Vp (0.80 cm³/g) was prepared from the mordenite (template) and furfural alcohol (carbon precursor) by nanocasting method. Template removal process (HF Treatment) had been optimized for tuning the textural and morphological features of the CNI-1 derivable. The carbon material was found to possess turbostratic graphitic structure. The CNI-1 was employed as support for Pt and the supported catalysts (10 wt.% Pt/CNI-1 (SB), 20 wt.% Pt/CNI-1 (SB) and 20 wt.% Pt/CNI-1 (EG)) produced by sol method were exploited as a possible electrode (anode) for the electro oxidation of methanol in Direct Methanol Fuel Cells applications.

Nitrogen containing templated microporous carbon (NCNI-1) with a S_{BET} (218 m²/g) and Vp (0.56 cm³/g) was prepared from the mordenite (template) and pyrrole (carbon precursor) by nanocasting method. Template removal process (HF Treatment) had been optimized for tuning the textural and morphological features of the NCNI-1 derivable. The carbon material was found to possess turbostratic graphitic structure. The NCNI-1 was employed as support for Pt and the supported catalysts (10 wt.% Pt/NCNI-1 (SB), 20 wt.% Pt/NCNI-1 (SB) and 20 wt.% Pt/NCNI-1 (EG)) produced by sol method were exploited as a possible electrode (anode) for the electro oxidation of methanol in Direct Methanol Fuel Cells applications.

Different methods were tried to optimize the method for the preparation of carbon supported Pt catalysts. Finally, sol method was found to be the best method for the preparation of methanol oxidation catalysts. Different reducing agents (SB and EG) were also used to identify the effect of reducing agents on the dispersion of Pt nanoparticles, methanol oxidation activity and stability. Pt metal on the carbon support was found to be in *fcc* lattice. The lattice constant value of ~ 0.39 nm correlated well with the *fcc* lattice of Pt metal on the carbon support.

The crystallite size of Pt in 10 wt.% Pt/CNI-1 (SB), 20 wt.% Pt/CNI-1 (SB) and 20 wt.% Pt/CNI-1 (EG) catalysts were respectively, 4.3, 4.8 and 6.0 nm. The crystallite size of Pt in 10 wt.% Pt/NCNI-1 (SB), 20 wt.% Pt/NCNI-1 (SB) and 20 wt.% Pt/NCNI-1 (EG) catalysts were respectively, 4.5, 4.0 and 6.2 nm. Thus the crystallite size of Pt which is the critical parameter governing the electrocatalytic property of Pt/C catalysts was found to be dependent on the Pt loading, nature of reducing agent and also the nature of the carbon support employed.

The methanol oxidation reaction carried out on Pt/C catalysts was monitored by cyclic voltammetry. Irrespective of the carbon support and the amount of the active component, two anodic peaks appeared in the cyclic voltammogram, one in the forward scan and the other in the reverse scan respectively attributable to the oxidation of methanol and the removal of the incompletely oxidized carbonaceous species formed in the forward scan.

Among different electrocatalysts evaluated, the 20 wt.% Pt/CNI-1 (SB) exhibited high MSA value (186 mA/mg of Pt) which is an indication of higher electrochemical activity at a relatively lower onset potential value (0.20 V). Only 68 % loss in the initial activity at the end of 0.5 h was observed in the case of 20 wt.% Pt/CNI-1 (SB) compared to 72 and 98 % activity losses observed in the cases of 20 wt. % Pt/AC (SB) and 20 wt.% Pt/NCNI-1 (SB) as indicated from the chronoamperometric studies implying better long term stability of 20 wt.% Pt/CNI-1 (SB).

CNI-1 was identified to be a promising support for electrode application in DMFC. SB reduced Pt catalysts supported on CNI-1 showed higher dispersion of Pt nanoparticles, smaller crystallite size, higher MSA for methanol oxidation, lower onset potential and better stability. But it lacked high CO tolerance capacity. Even nitrogen containing microporous carbon NCNI-1 as a support for Pt catalyst showed higher dispersion of Pt nanoparticles, smaller crystallite size, higher activity, high EAS and high CO tolerance. But Pt/NCNI-1 showed higher onset potential and lesser stability compare to Pt/CNI-1.The 20 wt.% Pt/CNI-1 (SB) was found to possess sufficient electro-active surface area with finely dispersed nanosized Pt particles of < 5 nm, which correlated well with the observed methanol oxidation activity and stability under potentiostatic conditions.

APPENDIX A

A.1 EDX SPECTRA OF ONC

A.1.1 EDX Spectra of CNI-1
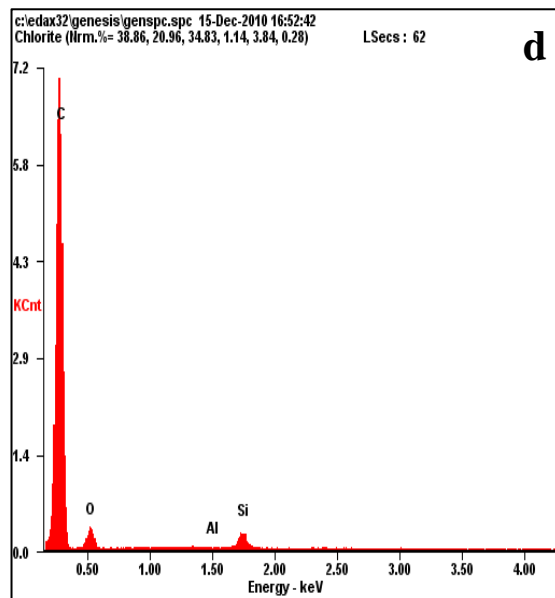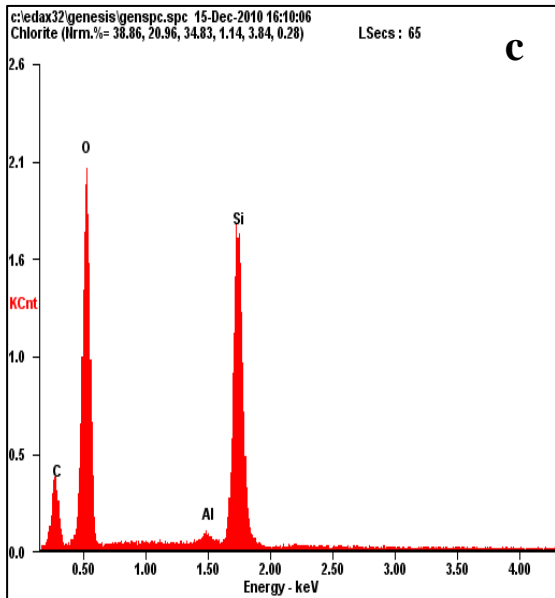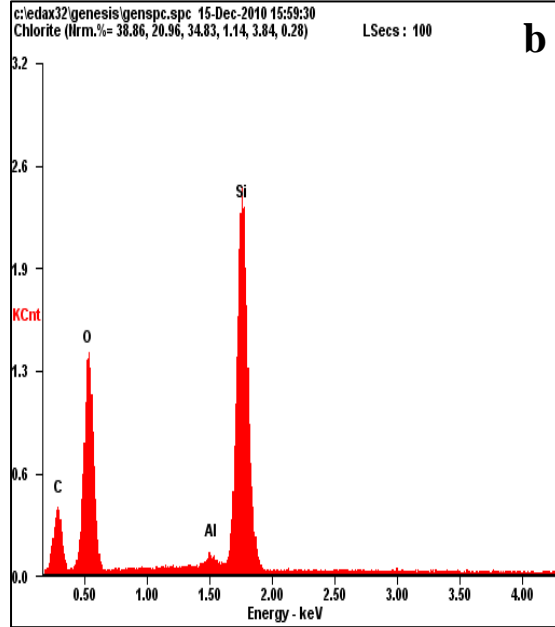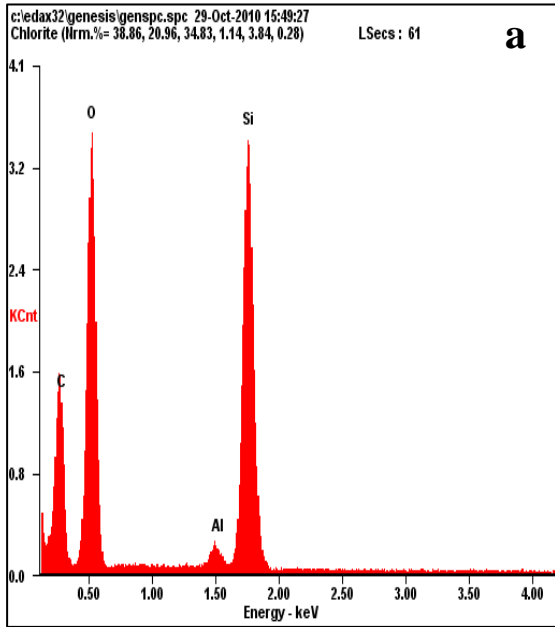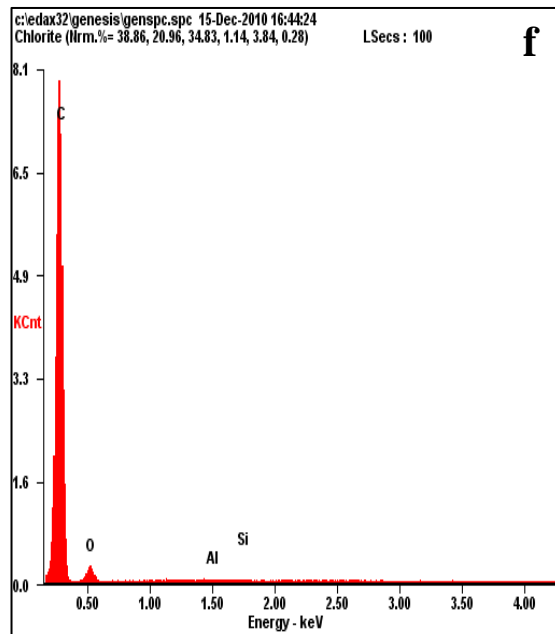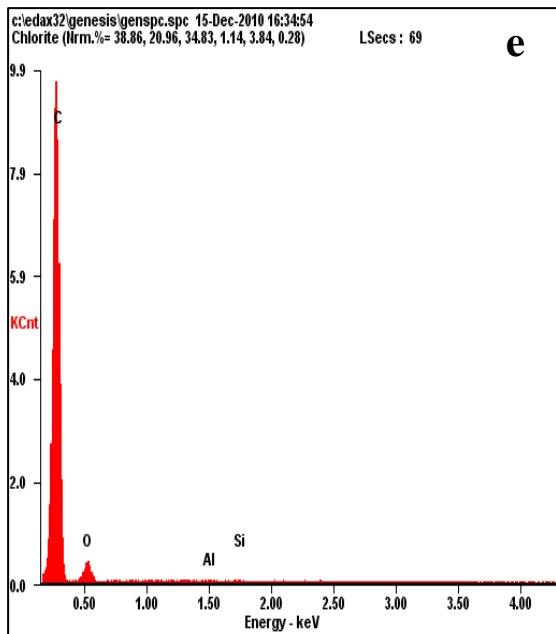
Figure A.1: EDX Spectra of (a) Mordenite; (b) FA/Mordenite composite; (c) Heat treated sample; (d) CNI-1 (2 % HF; 9 h); (e) CNI-1 (5 % HF; 3 h); (f) CNI-1 (5 % HF; 6 h).

A.1.2 EDX Spectra of NCNI-1
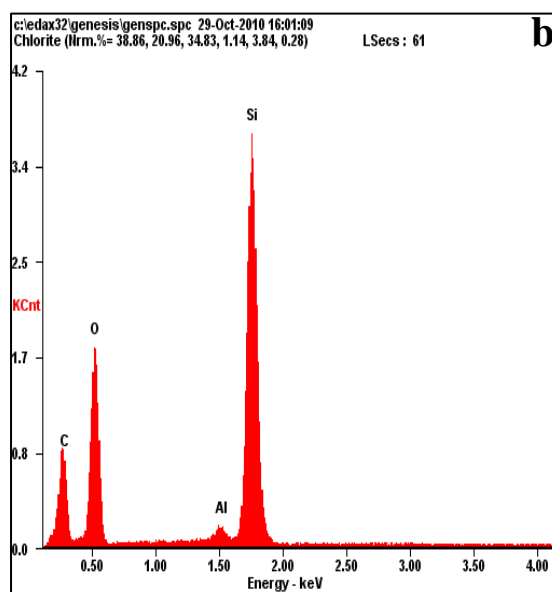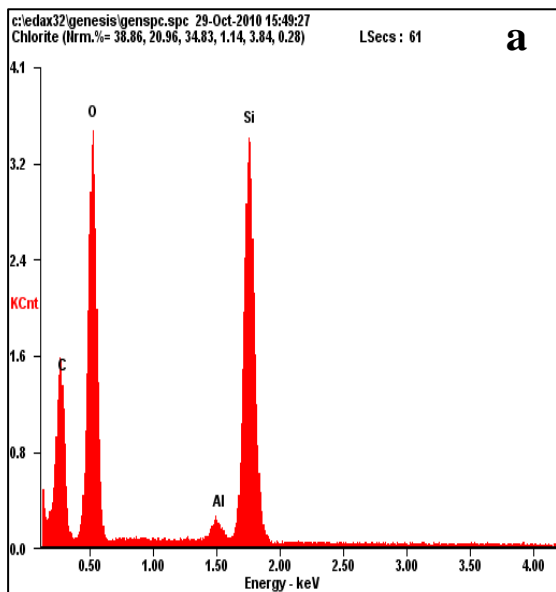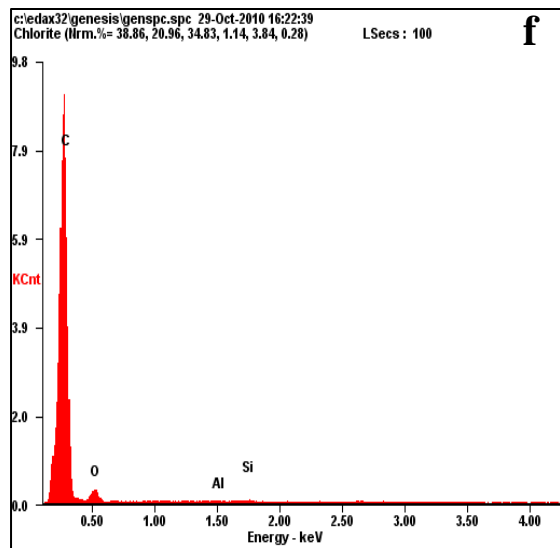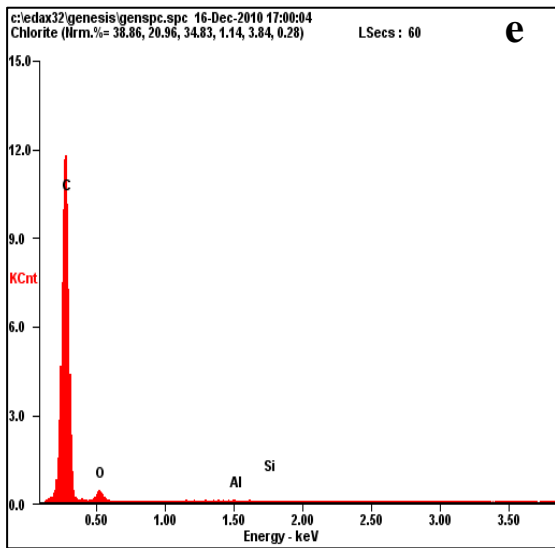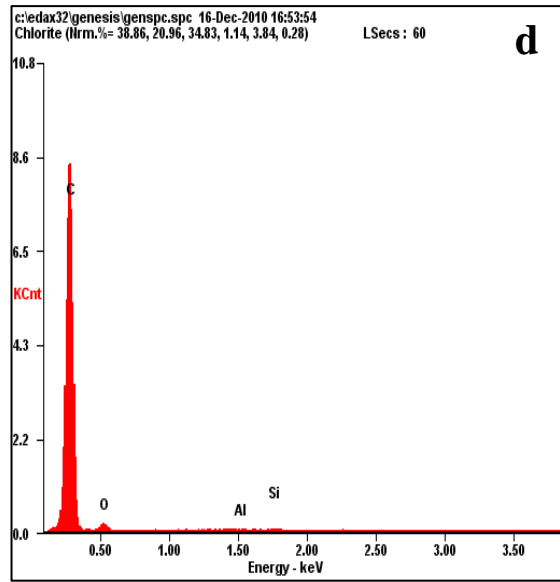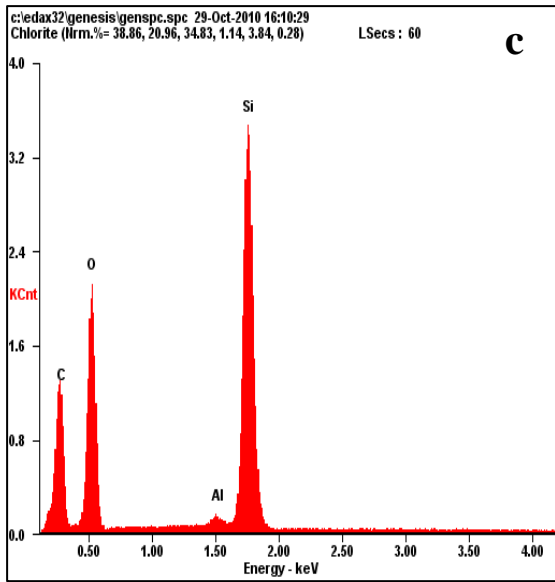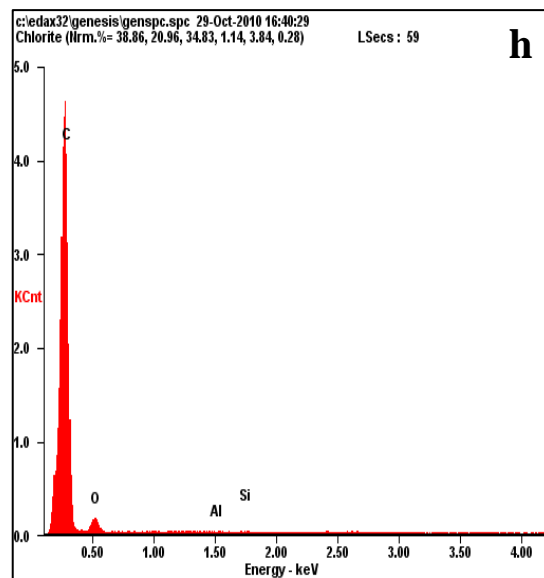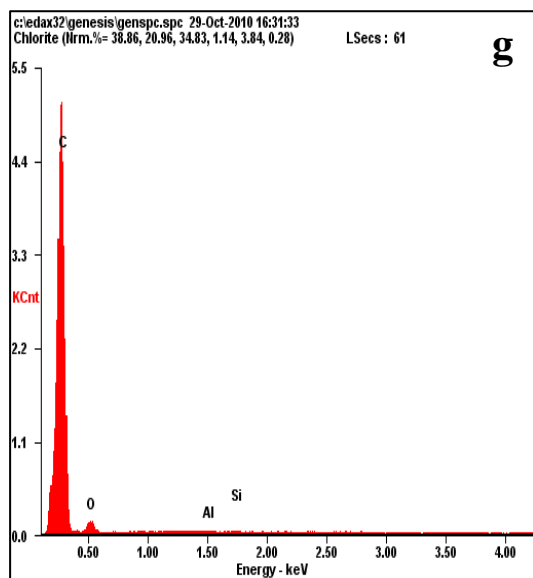
Figure A.2: EDAX of (a) Mordenite; (b) Pyrrole/Mordenite composite; (c) Heat treated sample; (d) NCNI-1 (5 % HF; 1 h); (e) NCNI-1 (5 % HF; 2 h); (f) NCNI-1 (5 % HF; 3 h); (g) NCNI-1 (5 % HF; 6 h); (h) NCNI-1 (5 % HF; 9 h).

APPENDIX B

B.1 PREPARATION OF ONC FROM MORDENITE AND SUCROSE

The micropores in the mordenite template were impregnated with sucrose and sulfuric acid using their aqueous solution. The template after the impregnation was heated at a temperature of 900 °C for 3 h in an inert atmosphere. The sucrose was converted to carbon by such a process using sulfuric acid as the catalyst. Finally, the template was removed by HF treatment (40 %) (Ryoo et al., 1999). The resultant templated microporous carbon material was referred to as CNI-9. Then the prepared CNI-9 was characterized by XRD, BET and SEM.

B.2 CHARACTERIZATION

B.2.1 XRD
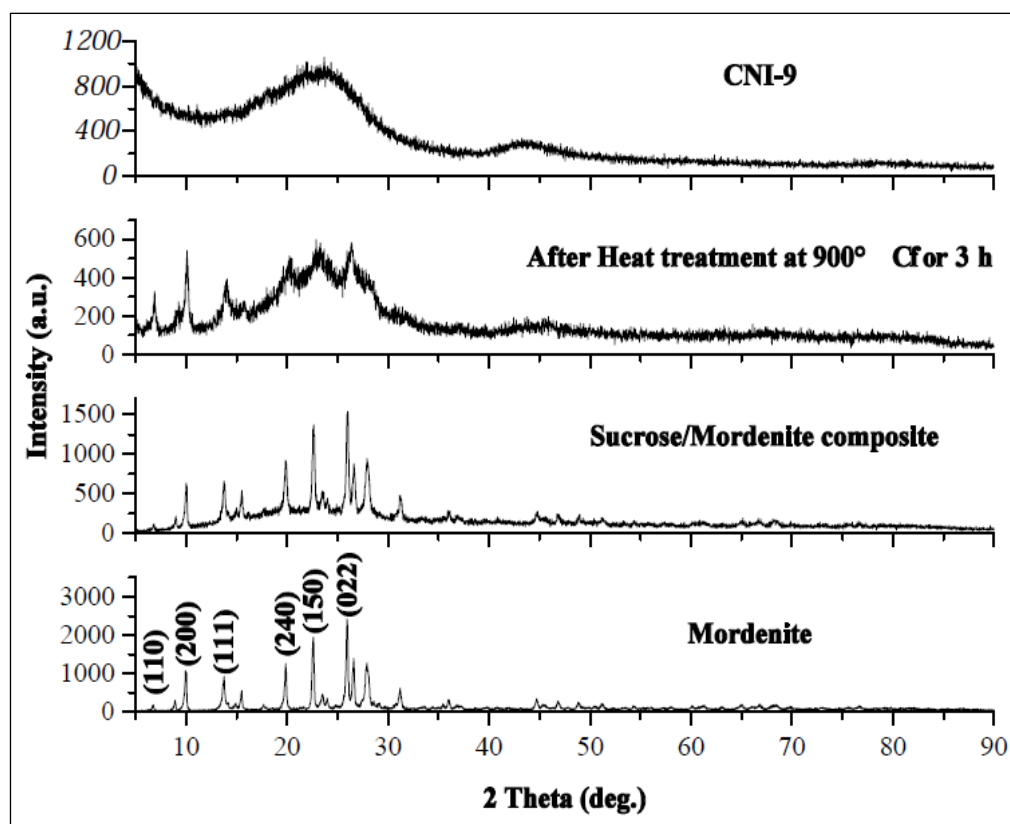
Figure B.1: XRD pattern of CNI-9

XRD patterns of the CNI-9 samples are shown in Fig. B.1. Sucrose /mordenite composite retained the ordered structure of the mordenite. During the heat treatment itself the structure started collapsing. It was evident form the XRD pattern. During the HF treatment, CNI-9 from template can collapse and form an amorphous like structure due to insufficient impregnation of the precursor. Therefore, template removal process has to be optimized to get an ordered carbon structure. In this case, 40 % HF was used for 24 h in order to remove the template. After the HF treatment, amorphous kind of CNI-9 was obtained.

B.2.2 Textural properties
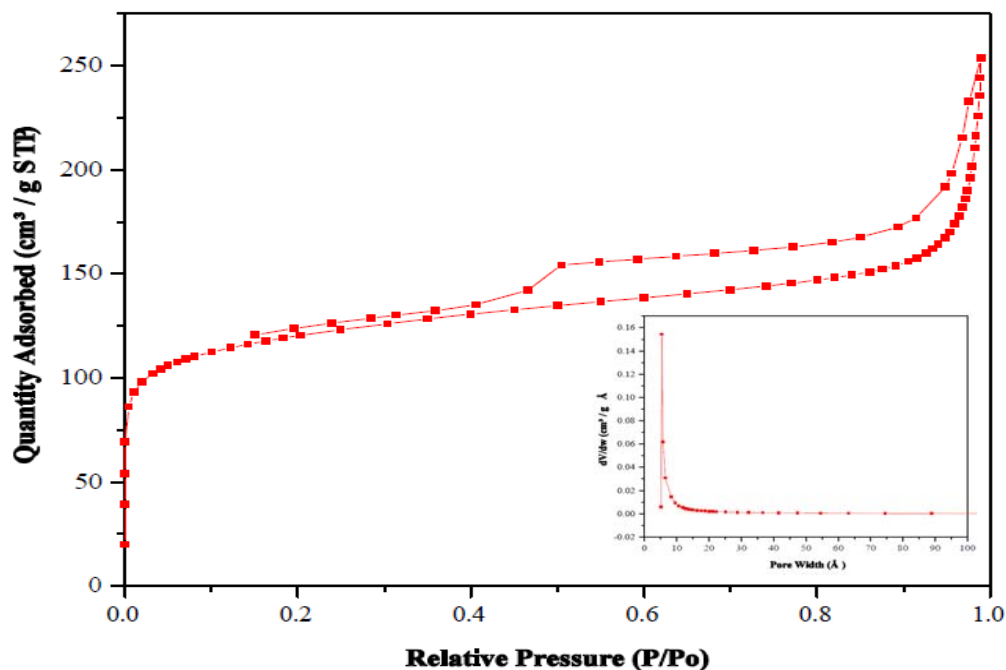
Figure B.2: N_2 sorption isotherm of CNI-9. Inset: Pore size distribution of CNI-9.

Table B.1: Textural properties of CNI-9

ONC	BET surface area (m²/g)	Pore volume (cm³/g)	Avg. Pore size (Å)
CNI-9	440	0.37	5.36

B.2.3 SEM
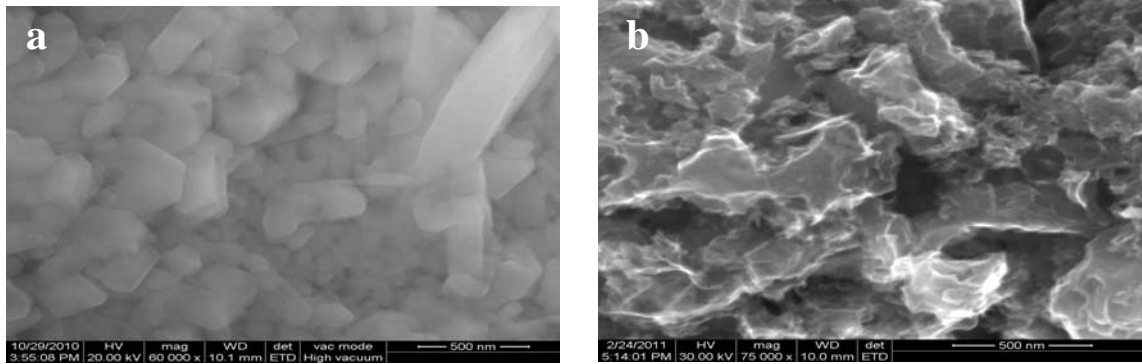
Figure B.3: SEM images of (a) Mordenite; (b) CNI-9.

B.2.4. EDAX
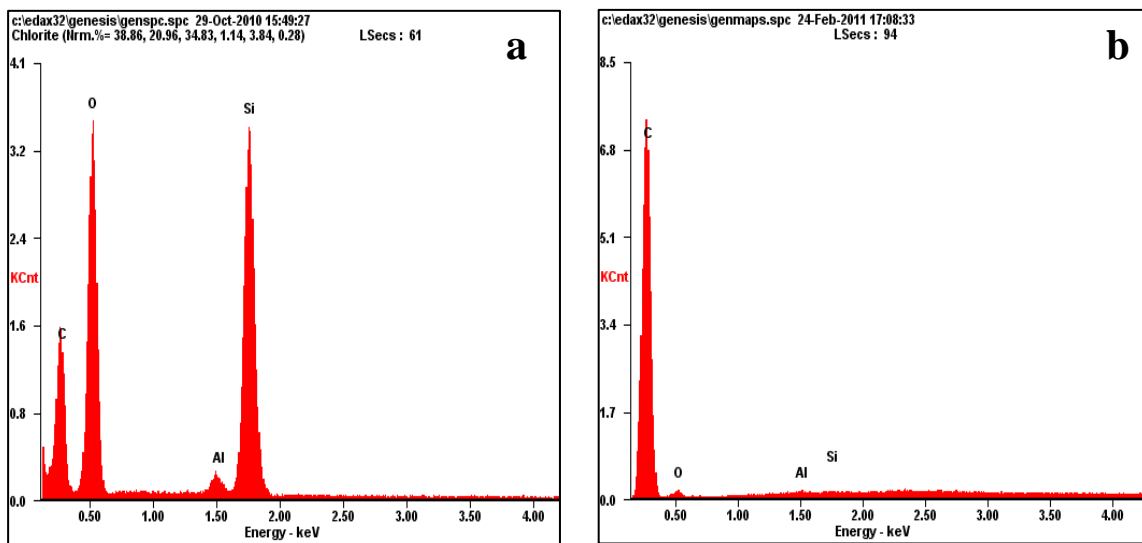
Figure B.4: EDAX spectra of (a) Mordenite; (b) CNI-9.

Table B.2: Elemental analysis results of CNI-9

Sample Names	Composition (Atom %)			
	C	O	Al	Si
Mordenite	39.98	51.78	0.48	7.76
CNI-9	97.18	02.72	0.07	0.03

APPENDIX C

C.1 PREPARATION OF ONC USING ZEOLIYE Y (NaY)

C.1.1 Furfural alcohol as a precursor

1 g of template (NaY) was impregnated with 4 ml of furfural alcohol and stirred for overnight. And then the suspension was filtered and washed with mesitylene to remove the carbon from the external surface of the template. Then the filtered sample was dried at 80 °C for 24 h and polymerized at 150 °C for 8 h. The polymerized sample was heat treated in the N_2 atmosphere for 700 °C for 3 h at the rate of 5 °C/min. After the heat treatment, the acquired sample was HF treated to remove the template and dried at 120 °C (Kyotani et al., 1995). The obtained templated microporous carbon was designated as CNI-2. Then the prepared CNI-2 was characterized by XRD and SEM.

C.1.2 Sucrose as a precursor

The micropores in the Zeolite Y (NaY) template were impregnated with sucrose and sulfuric acid using their aqueous solution. The template after the impregnation was heated at a temperature of 900 °C for 3 h in an inert atmosphere. The sucrose was converted to carbon by such a process using sulfuric acid as the catalyst. Finally, the template was removed by HF treatment (40 %) (Ryoo et al., 1999). The resultant templated microporous carbon material was referred to as CNI-8. Then the prepared CNI-8 was characterized by XRD and SEM.

C.2 CHARACTERIZATION

C.2.1 XRD
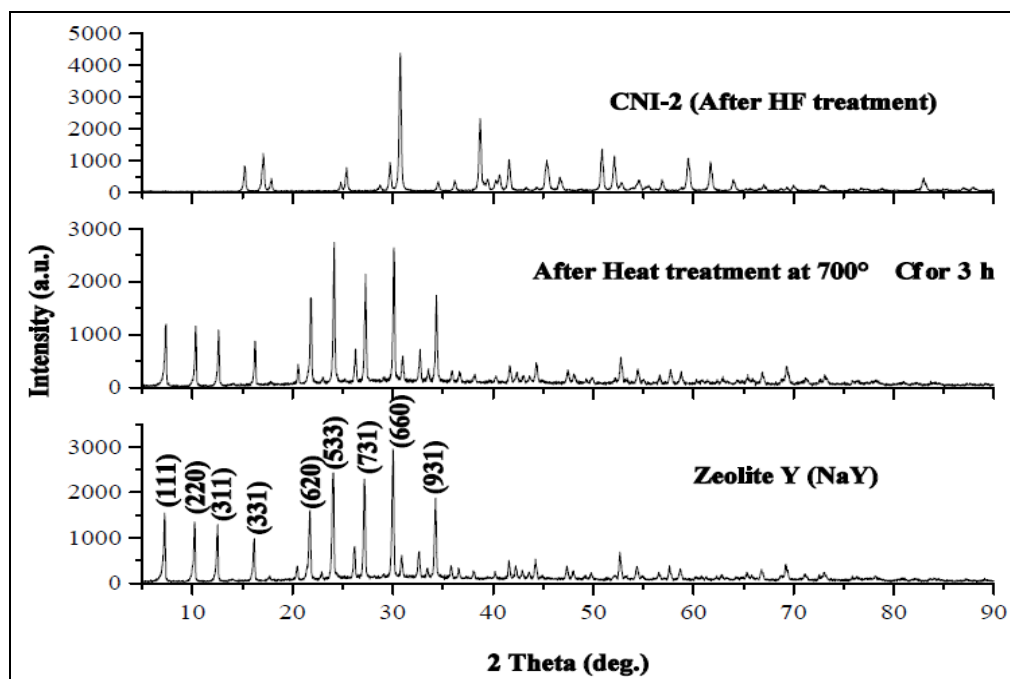
Figure C.1: XRD pattern of CNI-2
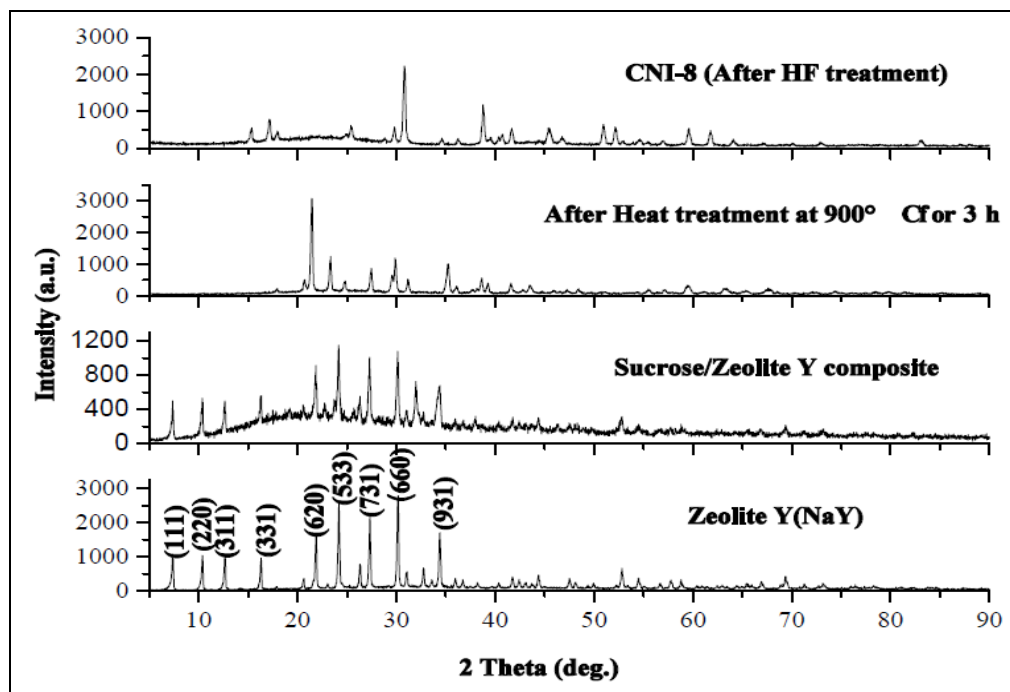
Figure C.2: XRD pattern of CNI-8

C.2.2 SEM

SEM Images of CNI-2
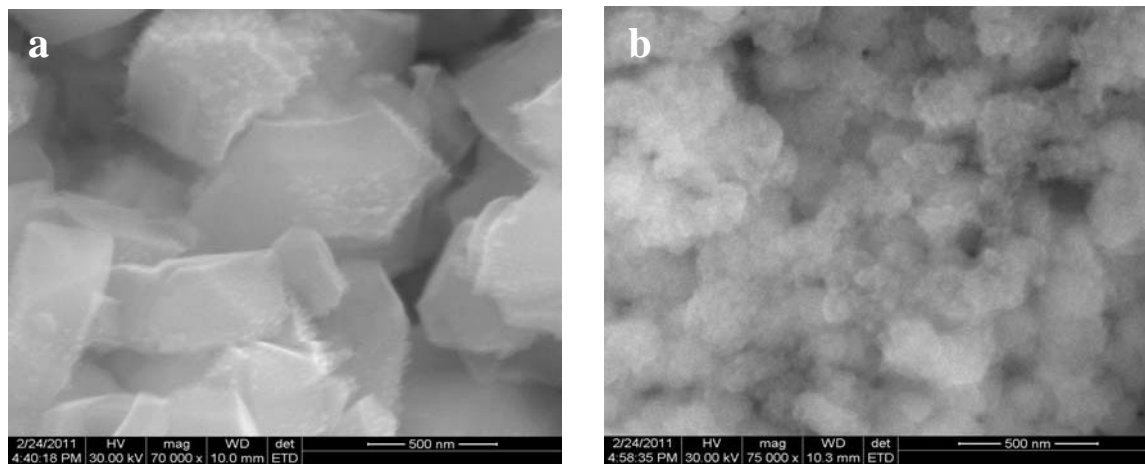
Figure C.3: SEM images of (a) NaY; (b) CNI-2 (After HF treatment).

SEM Images of CNI-8
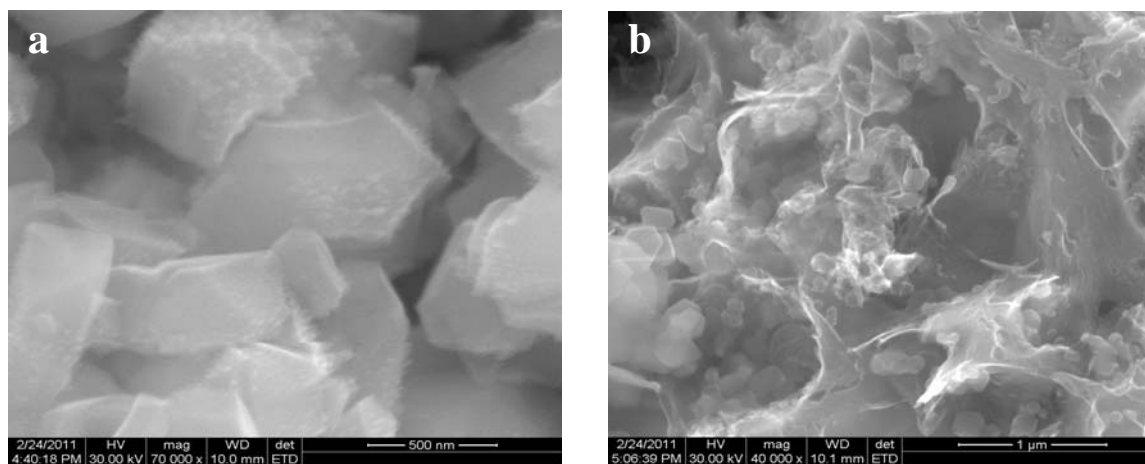
Figure C.4: SEM images of (a) NaY; (b) CNI-8 (After HF treatment).

C.2.3. EDAX

C.2.3.1 EDAX Spectra of CNI-2
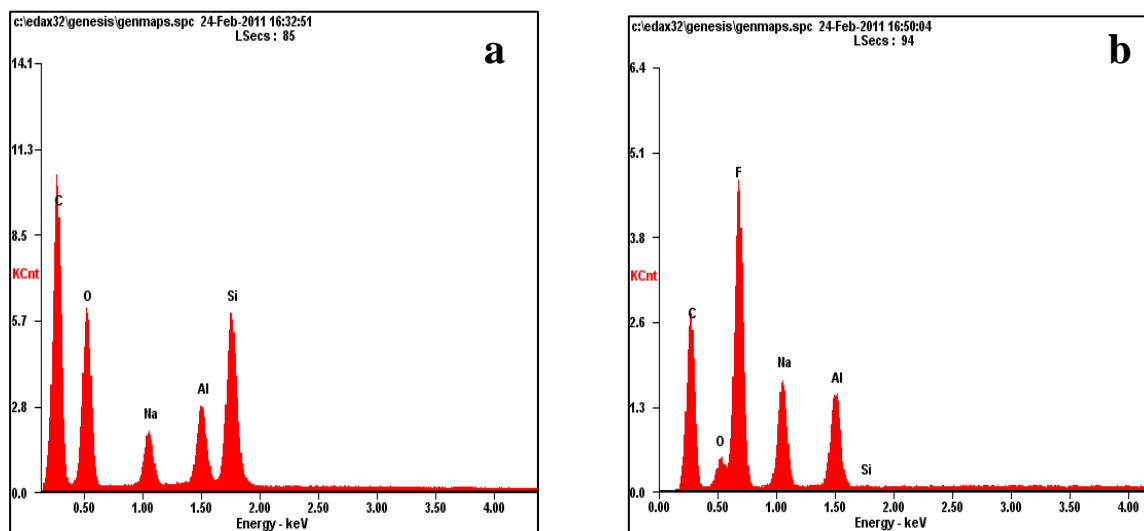
Figure C.5: EDX Spectra of (a) NaY; (b) CNI-2 (After HF treatment).

C.2.3.2 EDAX Spectra of CNI-8
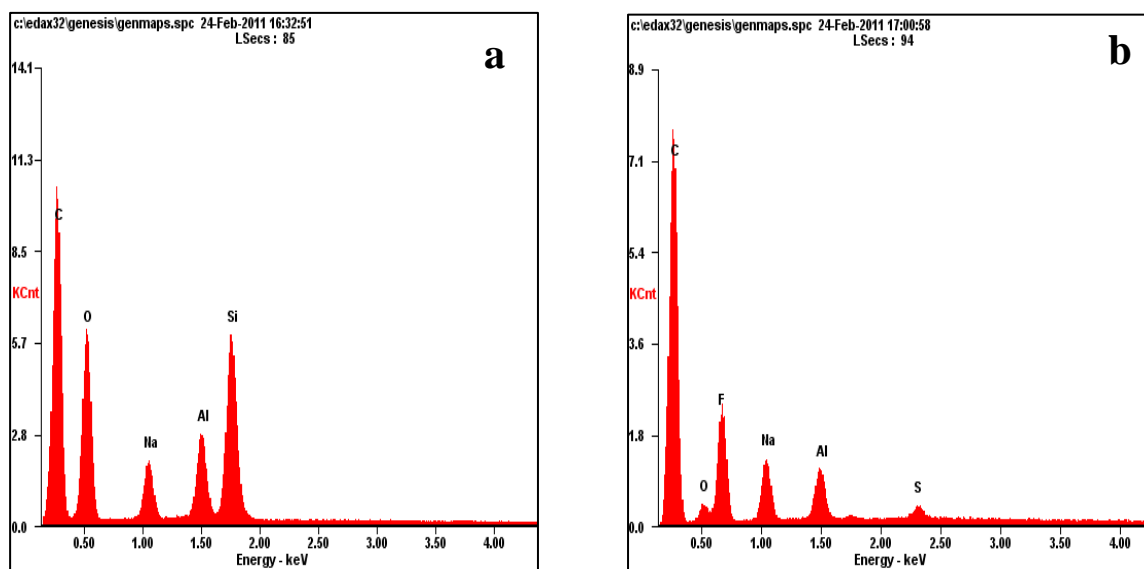
Figure C.6: EDX Spectra of (a) NaY; (b) CNI-8 (After HF treatment).

Table C.1: Elemental analysis results of CNI-2

Sample Names	Composition (Atom %)					
	C	O	F	Na	Al	Si
Zeolite Y (NaY)	70.71	24.68	-	1.61	1.05	1.95
CNI-2 (After HF treatment)	63.65	4.99	24.2	5.01	2.13	0.02

Table C.2: Elemental analysis results of CNI-8

Sample Names	Composition (Atom %)					
	C	O	F	Na	Al	Si
Zeolite Y (NaY)	70.71	24.68	-	01.61	01.05	01.95
CNI-8 (After HF treatment)	83.42	03.46	10.10	02.10	00.79	00.12

APPENDIX D

D.1 Methanol Electro Oxidation – Effect of Scan Rate
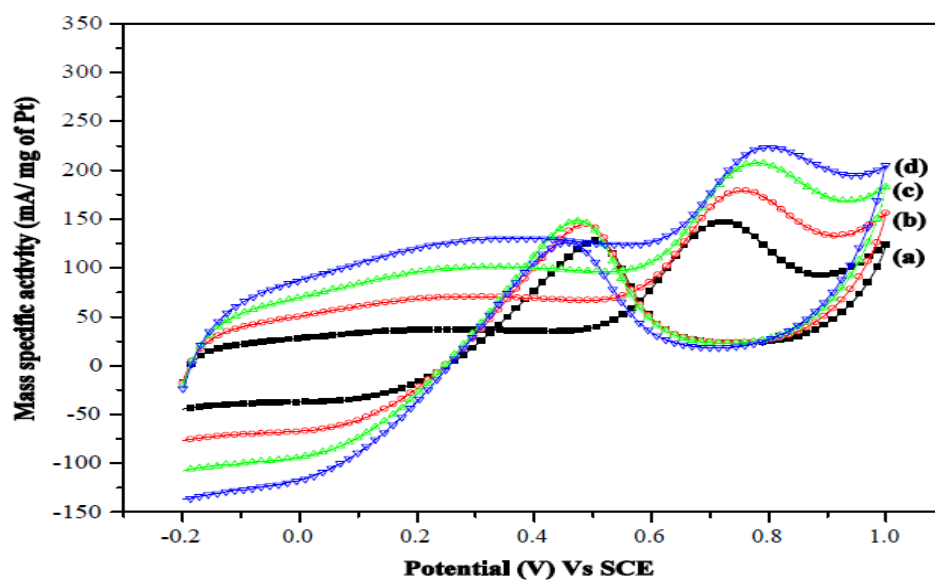
Figure D.1: Cyclic voltammograms of 20 wt.% Pt/NCNI-1 (SB) at different scan rates ((a) 25 mV/s; (b) 50 mV/s; (c) 75 mV/s; (d) 100 mV/s) in 1 M H_2SO_4 and1 M CH_3OH.
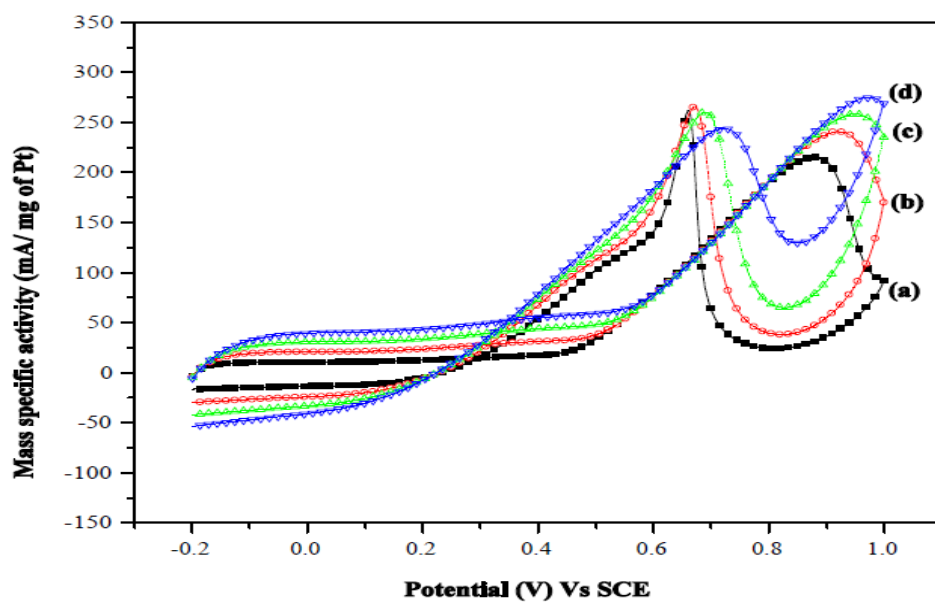
Figure D.2: Cyclic voltammograms of 20 wt.% Pt/AC (SB) at different scan rates ((a) 25 mV/s; (b) 50 mV/s; (c) 75 mV/s; (d) 100 mV/s) in 1 M H_2SO_4 and1 M CH_3OH.
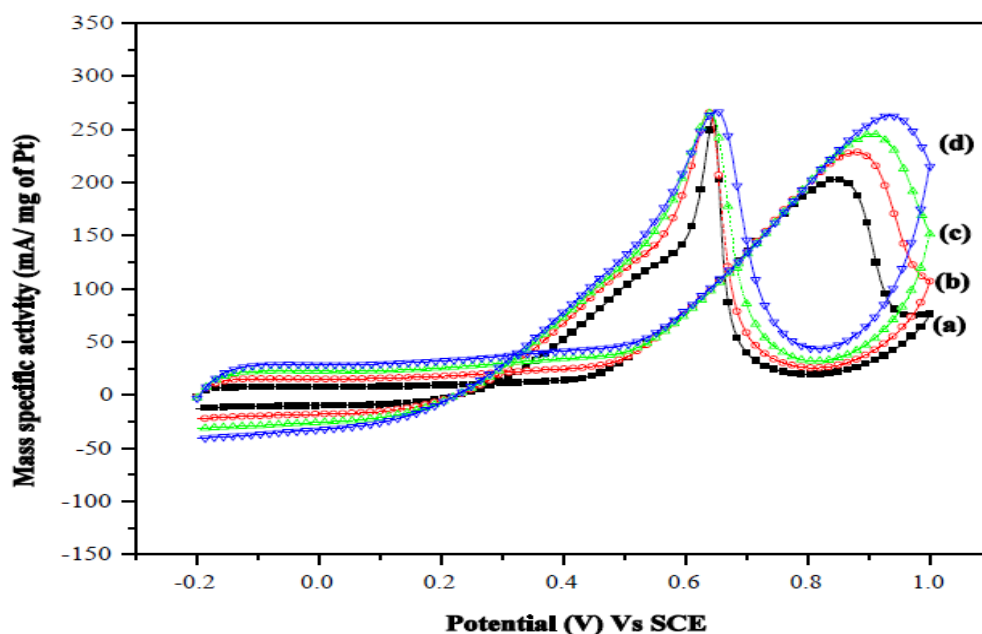
Figure D.3: Cyclic voltammograms of 20 wt.% Pt/CNI-1(EG) at different scan rates ((a) 25 mV/s; (b) 50 mV/s; (c) 75 mV/s; (d) 100 mV/s) in 1 M H_2SO_4 and 1 M CH_3OH.
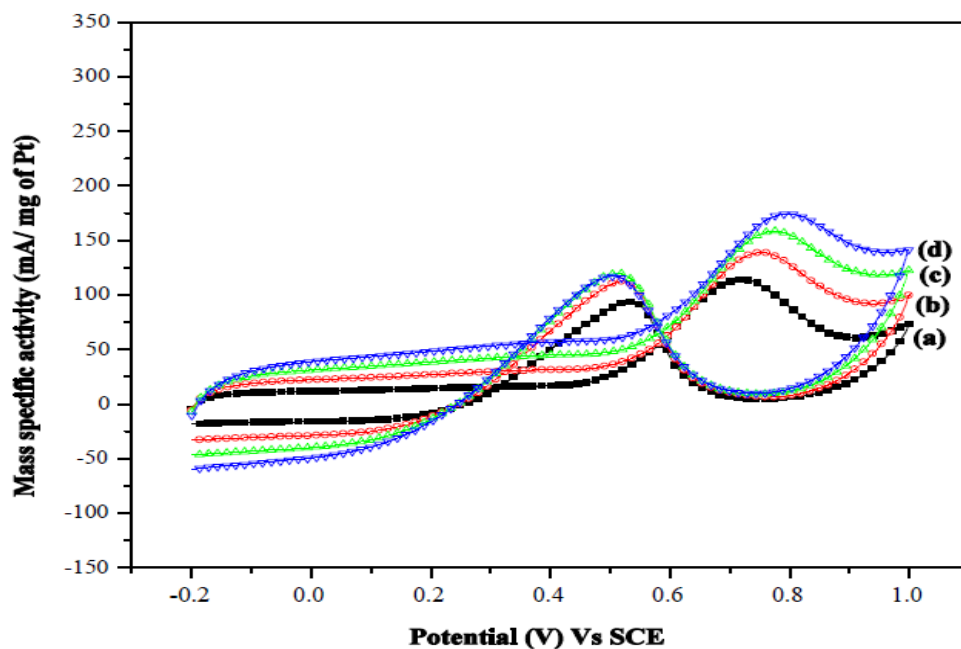
Figure D.4: Cyclic voltammograms of 20 wt.% Pt/NCNI-1(EG) at different scan rates ((a) 25 mV/s; (b) 50 mV/s; (c) 75 mV/s; (d) 100 mV/s) in 1 M H_2SO_4 and 1 M CH_3OH.
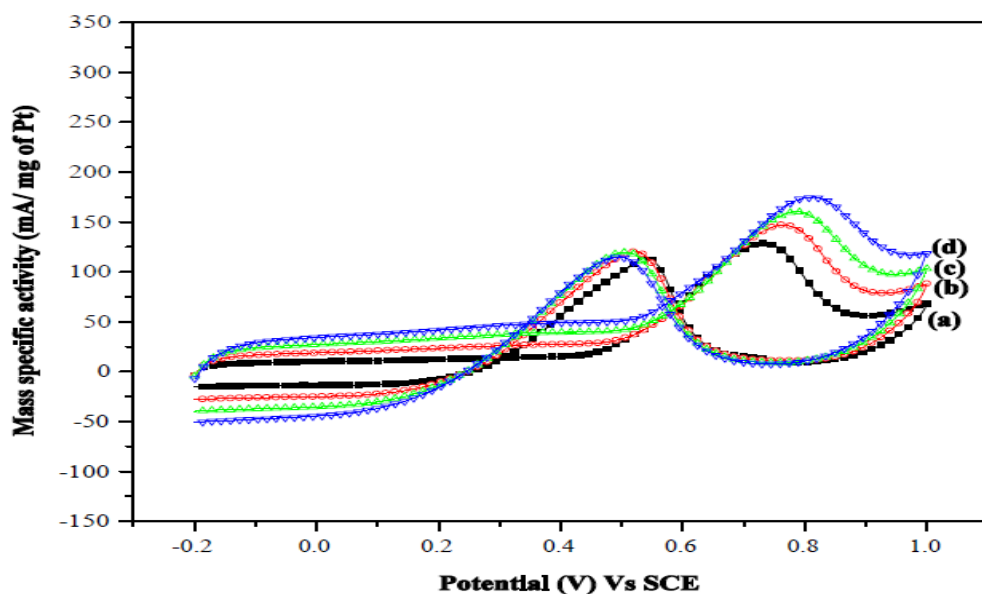
Figure D.5: Cyclic voltammograms of 20 wt.% Pt/AC (EG) at different scan rates ((a) 25 mV/s (b) 50 mV/s (c) 75 mV/s (d) 100 mV/s) in 1 M H_2SO_4 and1 M CH_3OH.
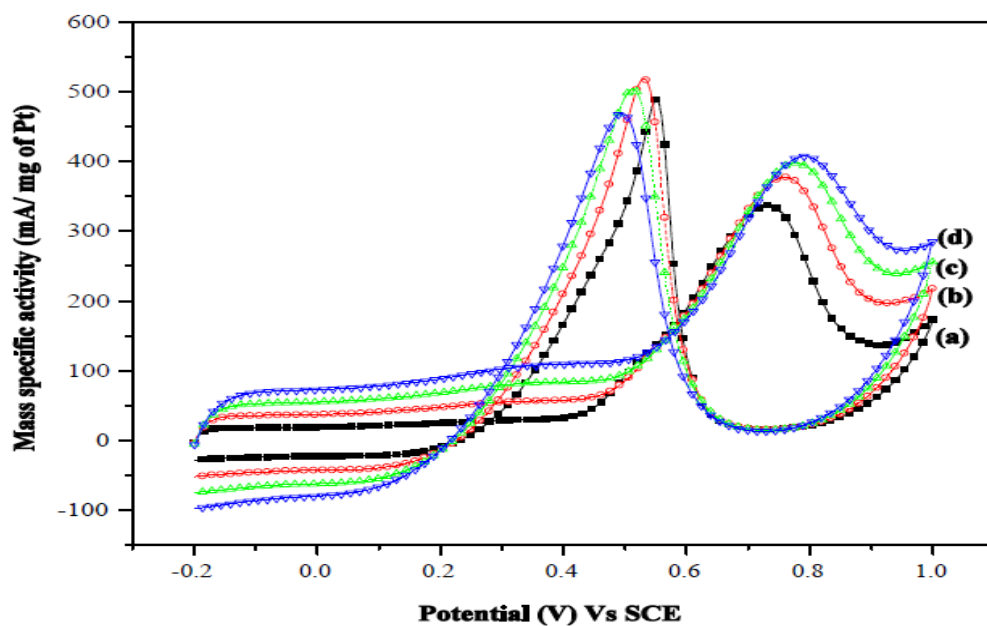
Figure D.6: Cyclic voltammograms of 10 wt.% Pt/CNI-1 (SB) at different scan rates ((a) 25 mV/s (b) 50 mV/s (c) 75 mV/s (d) 100 mV/s) in 1 M H_2SO_4 and1 M CH_3OH.
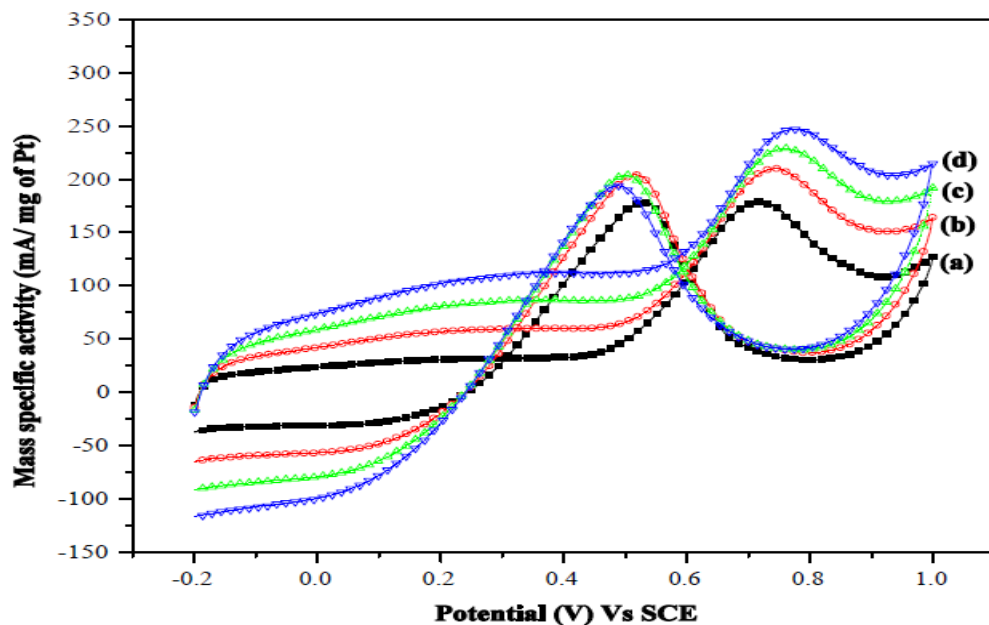
Figure D.7 : Cyclic voltammograms of 10 wt.% Pt/NCNI-1 (SB) at different scan rates ((a) 25 mV/s (b) 50 mV/s (c) 75 mV/s (d) 100 mV/s) in 1 M H_2SO_4 and 1 M CH_3OH.
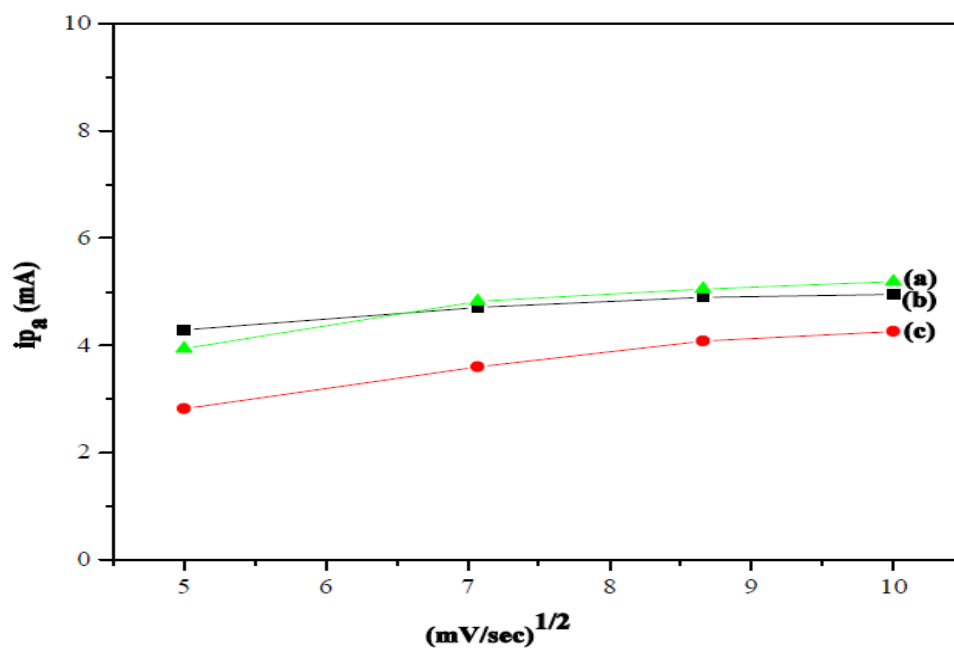
Figure D.8: Dependence of the peak currents on the square root of scan rates of (a) 20 wt.% Pt/AC (SB) (b) 20 wt.% Pt/CNI-1 (SB) and (c) 20 wt.% Pt/NCNI-1 (SB).
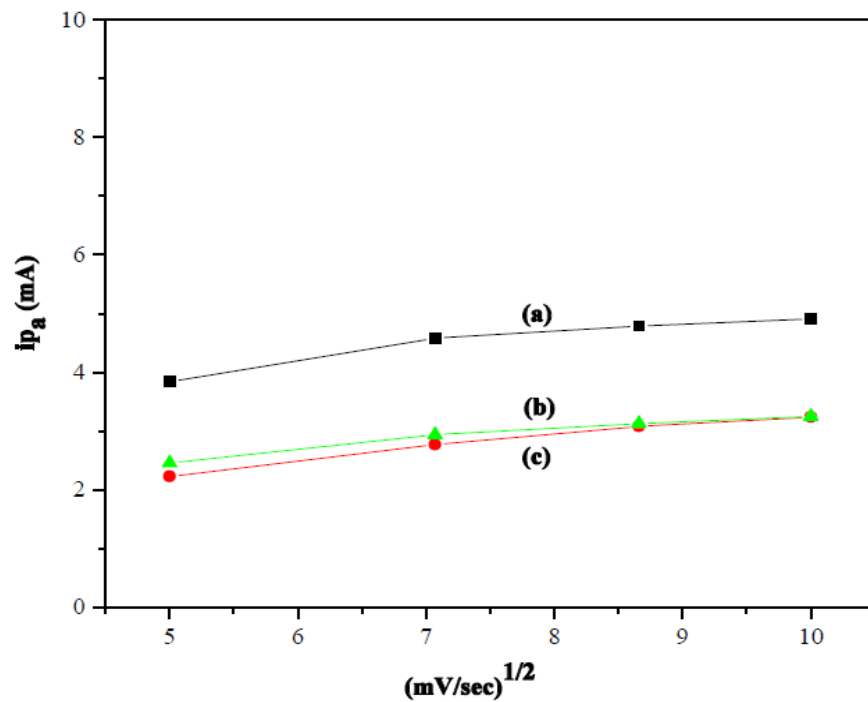
Figure D.9: Dependence of the peak currents on the square root of scan rates of (a) 20 wt.% Pt/CNI-1 (EG) (b) 20 wt.% Pt/AC (EG) and (c) 20 wt.% Pt/NCNI-1 (EG).
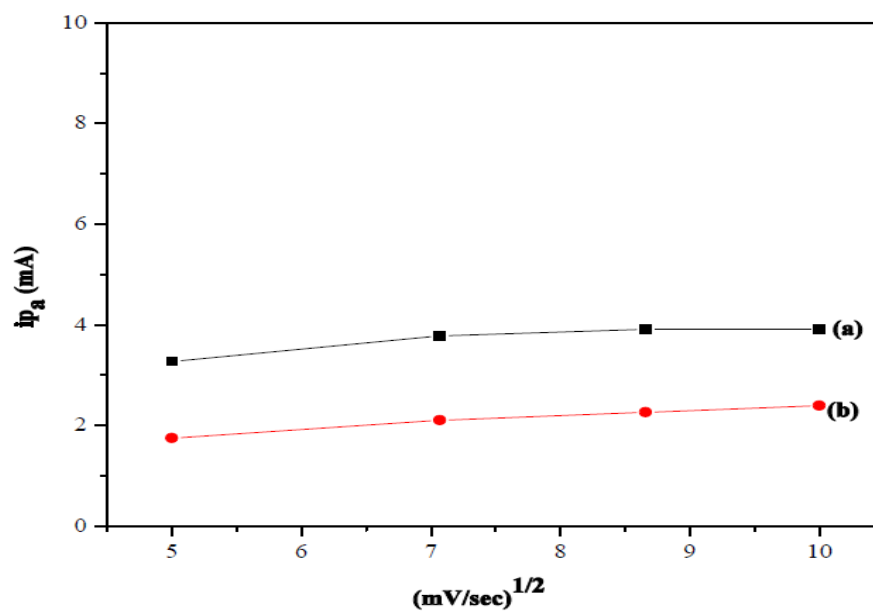
Figure D.10: Dependence of the peak currents on the square root of scan rates of (a) 10 wt.% Pt/CNI-1 (SB) (b) 10 wt.% Pt/NCNI-1 (SB).

APPENDIX E

CNI-1 SUPPORTED Pt, Pd and Pd$_3$Pt ELECTRODES FOR ORR

E.1 INTRODUCTION

The electrochemical reduction of molecular oxygen is important especially for devices such as metal-air batteries, fuel cells and air cathodes in many industrial electrocatalytic processes. Oxygen reduction reaction (ORR) has been studied over the years because of its fundamental complexity, sensitivity to the electrode surface and sluggish kinetics. The sluggish kinetics of ORR under the conditions employed in electrochemical devices is due to the low partial pressure of oxygen in air, slow flow rate of oxygen (i.e., less residence time for oxygen molecules on active sites) under ambient conditions. The main disadvantage in this electrode reaction is the value of exchange current density (j_0) in the region of 10^{-10} A/cm² in acidic medium and 10^{-8} A/cm² at 298 K in alkaline solution, which is lower than the j_0 value of anodic reaction in the electrochemical devices (Bockries and Reddy, 1970). Hence the oxygen reduction reaction usually contributes considerably to the overpotential and therefore results in a low efficiency in the functioning of electrochemical devices using air as oxidant. Understanding and exploitation of electrocatalysis for this reaction is needed more than any other reactions in electrochemical devices.

E.2 ELECTROCATALYSTS FOR OXYGEN REDUCTION

The essential criteria for a better oxygen reduction electrocatalysts are: high electronic conductivity, chemical and structural stability under conditions namely; operating temperature, wide range of oxygen partial pressure and concentration of electrolyte, ability to decompose the intermediate species formed during the reduction process, chemical and thermodynamic compatibility to electrolyte and interconnector materials, tolerant to contaminants and low cost.

Both noble and non-noble metal based electrodes were investigated for oxygen reduction. In the case of noble metal electrocatalysts, platinum and palladium based materials appear to be the best, whereas in the case of non-noble metal electrocatalysts, transition metal chalcogenides and pyrolyzed macrocyclic compounds are most widely studied.

E.2.1 Pt Metal Electrocatalysts

The most promising electrocatalysts for oxygen reduction are based on Pt since they exhibit good activity and chemical stability under operating conditions. The ORR consists of an oxygen diffusion process, adsorption process, charge transfer process, desorption process and back diffusion process. The work function would be one of the key factors of the charge transfer process, because the work function is the minimum energy needed to remove an electron from the material surface. However, the work function of Pt with high catalytic activity for the ORR is higher than the other transition metals (Trasatti, 1971).

In general, oxygen reduction takes place at higher positive potentials. At such high potentials, most of the metals will dissolve and give rise to a similar situation to that prevailing at the cathode i.e., only noble metals and some of their alloys offer possibilities among metallic systems. The most familiar oxygen reduction catalysts are based on noble metals, especially platinum. To date, conventional carbon supported platinum is the efficient electrocatalyst for oxygen reduction. But the cost of the Pt/C electrocatalysts is the main hurdle for the commercialization of electrochemical devices. To reduce the amount of Pt loading at the cathode side, thereby reducing cost, various synthetic approaches are adopted to disperse Pt on suitable support. Among the various support materials, carbon is the most attractive one because of its unique features like good electronic conductivity, chemical stability, surface area, mechanical stability and low cost.

The observations made from the ORR measurements on the carbon supported Pt catalysts are :

(i) Sluggish kinetics of oxygen reduction reaction of Pt. It was observed that the formation of –OH species at + 0.8 V on the Pt surface hinder the oxygen reduction in such a way the kinetics is not facile. The –OH species also causes the less availability of molecular oxygen species and thereby reduce ORR activity.

(ii) Oxygen reduction is a structure sensitive reaction.

(iii) Hydrogen peroxide formation during oxygen reduction on Pt.

ORR Mechanism: In terms of electrocatalysis, oxygen reduction on Pt crystallites occurs by a parallel mechanism with direct four-electron reduction as an essential step. The main steps in the mechanism of oxygen reduction on Pt are shown below (Sidik et al., 2002):

$$O_2 + 2Pt \rightarrow Pt_2O_2 \tag{1}$$

$$Pt_2O_2 + H^+ + e^- \rightarrow Pt2\text{-}O_2H \text{ (rate determining step)} \tag{2}$$

$$Pt_2\text{-}O_2H \rightarrow Pt\text{-}OH + Pt\text{-}O \tag{3}$$

$$Pt\text{-}OH + Pt\text{-}O + H^+ + e^- \rightarrow Pt\text{-}OH + Pt\text{-}OH \tag{4}$$

$$Pt\text{-}OH + Pt\text{-}OH + 2H^+ + 2e^- \rightarrow 2Pt + 2H_2O \tag{5}$$
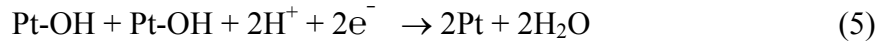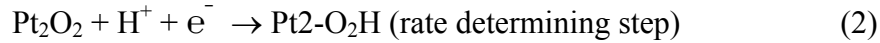
E.2.2 Pd Electrocatalyst

Palladium has a similar valence shell electronic configuration and lattice constant of Pt. It was also reported that the oxygen reduction takes place in the same manner as that of Pt (Sepa et al., 1981). But the less ORR activity than Pt and poor stability of Pd at high potentials prevents its commercialization. To improve the catalytic ORR activity of Pd, various bimetallic Pd alloys such as Pd-Co, Pd-Fe, Pd-Ni, Pd-Ta and Pd-Cr have been investigated. Pd/C, bimetallic Pd_3Pt/C catalysts were prepared by sol method using $NaBH_4$ and ethylene glycol as a reducing agents (Section 5.2.1).

E.3 CHARACTERIZATION

E.3.1 XRD
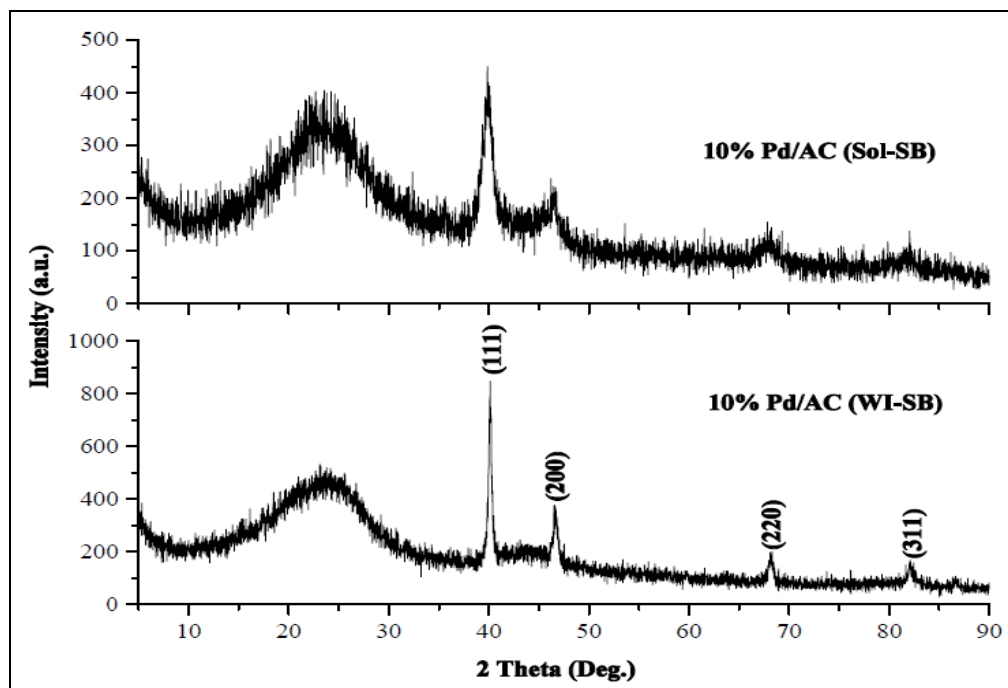
Figure E.1: XRD patterns of 10 wt.% Pd/AC prepared by sol and WI method using SB as a reducing agent.

Fig E.1 Shows XRD patterns of 10 wt.% Pd/AC prepared by different methods. 10 wt.% Pd supported on activated carbon had been done for the optimization process. The broad diffraction peak observed on activated carbon supported Pd catalysts at around 25° was corresponding to the carbon. The diffraction peaks at about 40.1°, 46.7°, 68.1° and 82.1° were from the Pd (1 1 1), (2 0 0), (2 2 0) and (3 1 1) planes, respectively (JCPDS file No. 89-4897). The crystallite sizes of Pd, calculated from the Pd (1 1 1) diffraction peak by means of Scherrer equation, for 10 wt.% Pd/AC prepared by wet impregnation and sol methods were 22.4 and 5.0 nm, respectively (Table E.1).
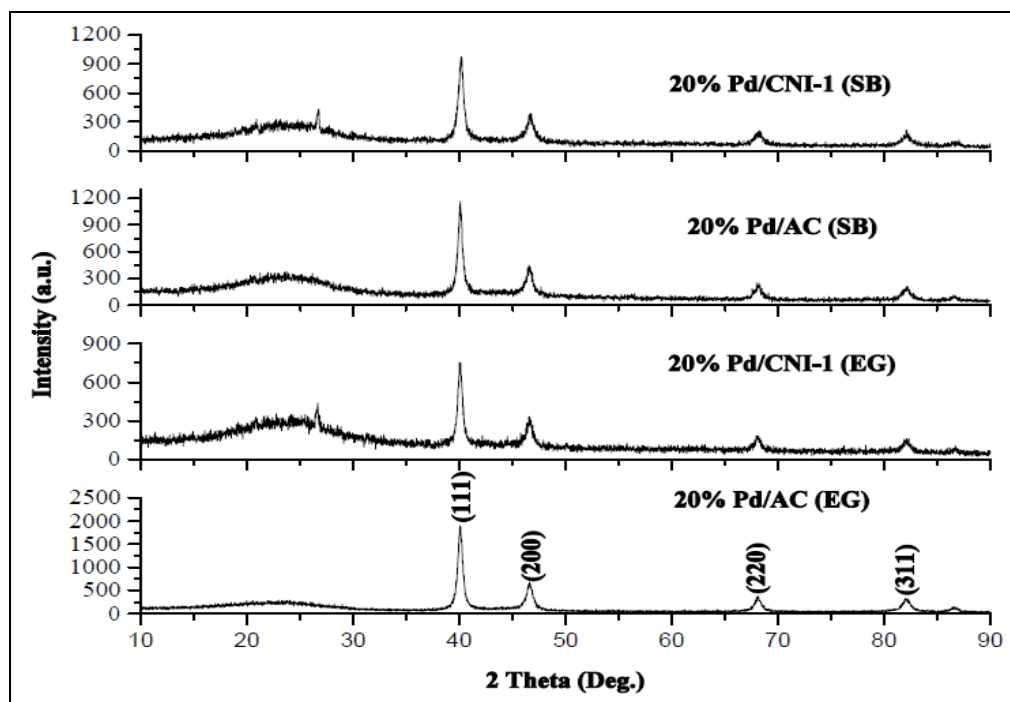
Figure E.2: XRD patterns of 20 wt.% Pd/ C (C: CNI-1/AC) prepared by sol method using different reducing agents (SB and EG).

Fig. E.2 shows XRD patterns of 20 wt.% Pd/C (Carbon: CNI-1 and AC) prepared by sol method using different reducing agents. The broad diffraction peak observed on carbon supported Pd catalysts at around 25° was corresponding to the carbon. The diffraction peaks at about 40.1°, 46.7°, 68.1° and 82.1° were from the Pd (1 1 1), (2 0 0), (2 2 0) and (3 1 1) planes, respectively (JCPDS file No. 87-0647). The crystallite sizes of Pd, calculated from the Pd (1 1 1) diffraction peak by means of Scherrer equation, for 20 wt.% Pd/AC (SB), 20 wt.% Pd/AC (EG), 20 wt.% Pd/CNI-1 (SB) were 20 wt.% Pd/CNI-1 (EG), prepared by sol method were 17.8, 17.0, 15.8 and 17.6 nm, respectively (Table E.2).
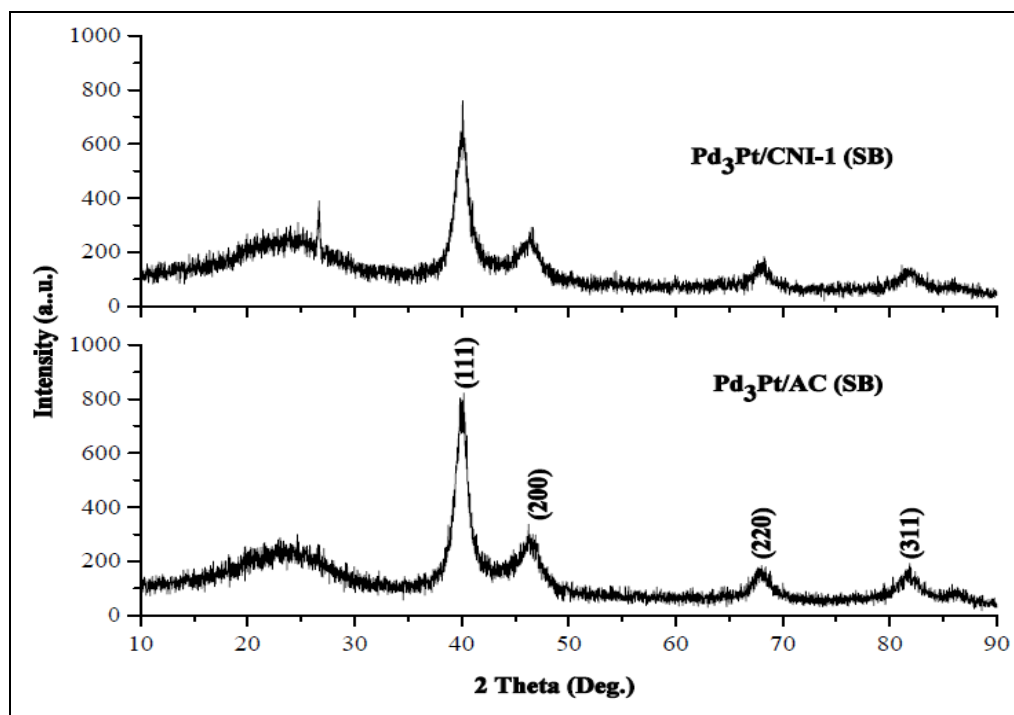
Figure E.3: XRD patterns of Pd₃Pt/C (C: CNI-1/AC) prepared by sol method using SB as a reducing agent.
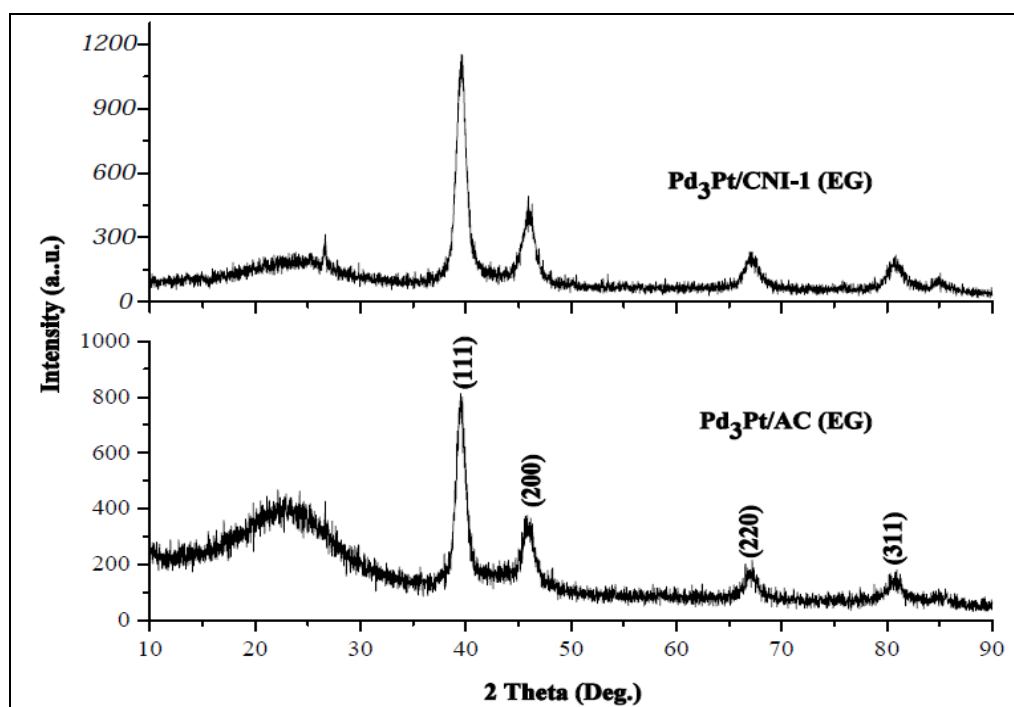
Figure E.4: XRD patterns of Pd₃Pt/C (C: CNI-1/AC) prepared by sol method using EG as a reducing agent.

Fig E.3 and E.4 show XRD patterns of Pd$_3$Pt/C (Carbon: CNI-1 and AC) prepared by using NaBH$_4$ and ethylene glycol as a reducing agent respectively. The broad diffraction peak observed on Pd$_3$Pt/C catalysts at around 25° was corresponding to the carbon. The XRD patterns of the bimetallic catalysts displayed a slight negative shift relative to the bulk Pd at around 2θ = 40.1°, 46.7°, 68.1° and 82.1° which indicates that a number of Pd atoms were displaced by the larger Pt atoms leading to a lattice expansion due to the formation of Pd-Pt alloys (An et al., 2011). The diffraction peaks at around 39.5°, 45.8°, 67.1° and 80.8° are corresponding to Pd$_3$Pt (111), (200), (220) and (311) planes respectively. All the diffraction peaks of Pd$_3$Pt were used to calculate the crystalline lattice parameters and the Pd$_3$Pt (111) peak was used for the calculation of crystallite size by means of Scherrer equation. The calculated crystallite size values of Pd$_3$Pt catalysts were tabulated (Table E.3).

Table E.1: Effect of preparation method on the crystallite size of the activated carbon supported Pd catalysts.

10 wt.% Pd/AC Preparation methods	Reducing Medium	Pd Lattice Constant (nm)	Pd Crystallite Size (nm)
Wet Impregnation	NaBH$_4$	0.3885	22.4
Sol	NaBH$_4$	0.3894	5.0

Table E.2: Effect of reducing agent and palladium loading on the crystallite size of the carbon supported Pd catalysts.

Pd Catalysts	Pd Lattice Constant (nm)	Pd Crystallite Size (nm)
20 wt.% Pd/CNI-1 (SB)	0.3889	15.8
20 wt.% Pd/AC (SB)	0.389	17.8
20 wt.% Pd/CNI-1 (EG)	0.3896	17.6
20 wt.% Pd/AC (EG)	0.3892	17.0

Table E.3: Effect of reducing agent and active metal loading on the crystallite size of the carbon supported Pd$_3$Pt catalysts.

Pd$_3$Pt Catalysts	Pd$_3$Pt Lattice Constant (nm)	Pd$_3$Pt Crystallite Size (nm)
Pd$_3$Pt /CNI-1 (SB)	0.3898	6.4
Pd$_3$Pt /AC (SB)	0.3898	6.9
Pd3Pt /CNI-1 (EG)	0.3942	8.7
Pd$_3$Pt /AC (EG)	0.3945	8.8

E.3.2 Electrochemical reduction of Oxygen

Electrochemical oxygen reduction measurements were performed at room temperature in a three electrode; one compartment cell containing 1 M H$_2$SO$_4$ as the electrolyte. After fabrication, the electrode was immersed in 1 M H$_2$SO$_4$ and purged with N$_2$ gas for 30 min to deaerate the solution. Then the cyclic voltammogram (at the scan rate of 50 mV/s) were recorded between -0.2 V to + 1.2 V Vs SCE. For the oxygen reduction experiments, the electrolyte was saturated with pure oxygen and the cyclic voltammogram (at the scan rate of 50 mV/s) were recorded between - 0.2 V to + 1.2 V Vs SCE. Current densities were normalized to the geometric area of the glossy carbon substrate (0.07 cm^2).
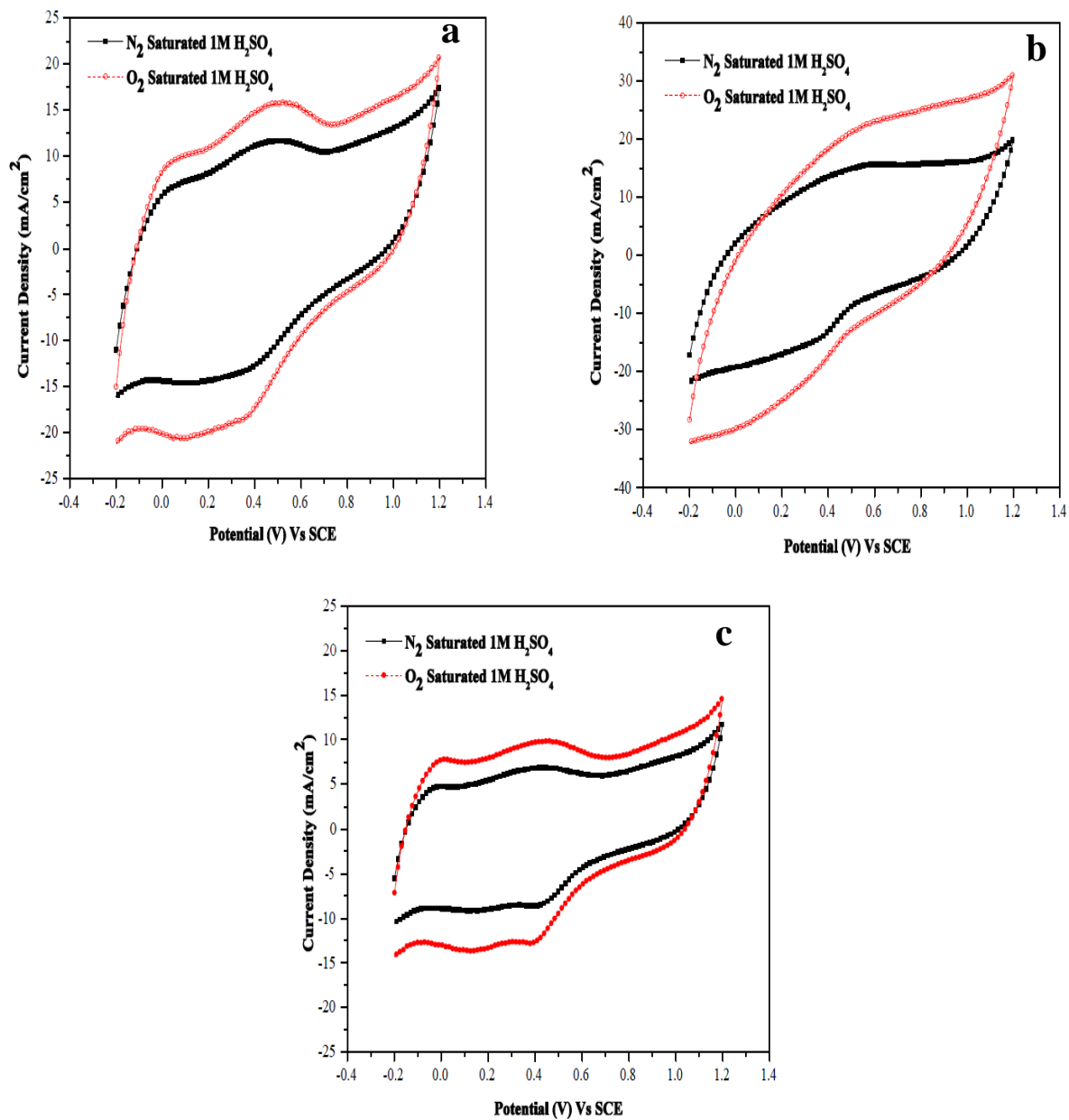
Figure E.5: Cyclic voltammograms (CV) (a) 20 wt.% Pt/ CNI-1 (SB); (b) 20 wt.% Pd/ CNI-1 (SB); (c) Pd_3Pt/ CNI-1 (SB) in N_2 as well as O_2 saturated 1 M H_2SO_4 solution (scan rate of 50: mV/s).

From Fig. E.5, it was evident that the oxygen reduction on all the catalysts was diffusion controlled when the potential was below + 0.4 V region and was under mixed diffusion-kinetic control in the potential region between + 0.4 V and + 1.2 V Vs SCE. For all the catalysts, single oxygen reduction peak was observed in the potential region of + 1.0 to + 0.4 V. The steep increase in peak current at + 0.4 V indicates the facile kinetics of ORR. Oxygen reduction activity was

calculated by taking the difference in activity at + 0.4 V Vs SCE in N_2 and O_2 saturated 1 M H_2SO_4 and given in Table E.4. 20 wt.% Pt/CNI-1 (SB) showed higher ORR activity compare to other two catalysts. That higher activity of the Pt based monometallic catalyst can be attributed to the uniform and smaller particle size as well as to the higher dispersion of the Pt nanoparticles on the carbon support (Fig. 5.5b and Fig. 5.6b).

Table E.4: ORR activity of the prepared monometallic and bimetallic catalysts.

Catalysts	ORR activity at + 0.4 V Vs SCE (mA/cm²)
20 wt.% Pt/CNI-1 (SB)	4.60
20 wt.% Pd/CNI-1 (SB)	4.26
Pd_3Pt/CNI-1 (SB)	4.00

REFERENCES

1. **An, S., J.-H. Park, C.-H. Shin, J. Joo, E. Ramasamy, J. Hwang** and **J. Lee** (2011) Well-dispersed Pd_3Pt_1 alloy nanoparticles in large pore sized mesocellular carbon foam for improved methanol-tolerant oxygen reduction reaction. *Carbon*, **49**, 1108-1117.

2. **Bensebaa, F., N. Patrito, Y. L. Page, P. L'Ecuyer** and **D. Wang** (2004) Tunable platinum–ruthenium nanoparticle properties using microwave synthesis. *J. Mater. Chem.*, **14**, 3378-3384.

3. **Bockries J. O'M.** and **A. K. N. Reddy** *Modern Electrochemistry: Vol. 2.* Plenum Press, New York, 1970.

4. **Bong, S., Y. -R. Kim, I. Kim, S. Woo, S. Uhm, J. Lee** and **H. Kim** (2010) Graphene supported electrocatalysts for methanol oxidation. *Electrochem. commun.*, **12**, 129-131.

5. **Chambers, A., C. Park, R. Terry, K. Baker** and **N. M. Rodriguez** (1998) Hydrogen Storage in Graphite Nanofibers. *J. Phys. Chem. B*, **102**, 4253-4256.

6. **Chen, J., N. Xia, T. Zhou, S. Tan, F. Jiang** and **D. Yuan** (2009). Mesoporous Carbon Spheres: Synthesis, Characterization and Supercapacitance. *Int. J. Electrochem. Sci.*, **4**, 1063-1073.

7. **Chen, S., J. Zhu, X. Wu, Q. Han** and **X. Wang** (2010). Graphene Oxide-MnO_2 Nanocomposites for Supercapacitors. *Nano*, **4**, 2822-2830.

8. **Cullity, B. D.** *Elements of X-Ray Diffraction*. Addison-Wesley Publishing Company, Inc., 1978.

9. **Dicks, A. L.** (2006). The role of carbon in fuel cells. *J. Power Sources*, **156**, 128-141.

10. **Evans, R. C.** *An Introduction to Crystal Chemistry (2nd Edition)*, Cambridge University Press, 1964.

11. **Fan, Y. Y., B. Liao, M. Liu, Y. L. Wei, M. Q. Lu** and **H. M. Cheng** (1999) Hydrogen uptake in vapor-grown carbon nanofibers. *Carbon*, **37**, 1649-1652.

12. **Guo, J. W., T. S. Zhao, J. Prabhuram, R. Chen** and **C. W. Wong** (2006) Development of PtRu-CeO2/C anode electrocatalyst for direct methanol fuel cells. *J. Power Sources*, **156**, 345-354.

13. **Hamnett, A.** (1997). Mechanism and electrocatalysis in the direct methanol fuel cell. *Catal.Today*, **38**, 445-457.

14. **Hirscher, M., M. Becher, M. Haluska, A. Quintel, V. Skakalova, Y. M. Choi, U. D.- Weglikowska, S. Roth, I. Stepanek, P. Bernier, A. Leonhardt** and **J. Fink** (2002) Hydrogen storage in carbon nanostructures. *J. Alloys and Compounds*, **330-332**, 654-658.

15. **Hufner, S.** and **G. K. Wertheim** (1975) Core-line asymmetries in the X-ray photoemission spectra of metals. *Phy. Rev. B*, **11**, 678-683.

16. **Ji, X., K. Y. Lee, R. Holden, L. Zhang, J. Zhang, G. A. Botton, M. Couillard** and **L. F. Nazar** (2010). Nanocrystalline intermetallics on mesoporous carbon for direct formic acid fuel cell anodes. *Nature Chemistry*, **2**, 286-293.

17. **Jun, S., S .H. Joo, R. Ryoo, M. Kruk, M. Jaroniec, Z. Liu, T. Ohsuna** and **O. Terasaki** (2000) Synthesis of New, Nanoporous Carbon with Hexagonally Ordered Mesostructure. *J. Am. Chem. Soc.*, **122**, 10712-10713.

18. **F. Kapteijn, J.A. Moulijn, S. Matzner** and **H.P. Boehm** (1999) The development of nitrogen functionality in model chars during gasification in CO_2 and O2. *Carbon,* **37**, 1143-1150.

19. **Kim, K. H.** and **K. B. Kim** (2006) Synthesis of Mesoporous metal oxide/carbon nanotube composite electrode using Hard template method for Supercapacitors. ECS 210th meeting, Abstract0130.

20. **Kim, T. W., R. Ryoo, K. P. Gierszal, M. Jaroniec, L. A. Solovyov, Y. Sakamoto** and **O. Terasaki** (2005). Characterization of mesoporous carbons synthesized with SBA-16 silica template**. *J. Mater. Chem.*, **15**, 1560-1571.

21. **Kyotani, T., T. Nagai, S. Inoue** and **A. Tomita** (1997) Formation of New Type Of Porous Carbon by Carbonization in Zeolite Nanochannels. *Chem. Mater.*, **9**, 609–615.

22. **Kyotani, T., N. Sonobe** and **A.Tomita** (1988) Formation of highly orientated graphite from polyacrylonitrile by using a two-dimensional space between montmorillonite lamellae. *Nature*, **331**, 331.

23. **Kyotani, T., L. Tsai** and **A. Tomita** (1995) Formation of Ultrafine Carbon Tubes by using an Anodic Aluminum Oxide Film as a template. *Chem Mater.*, **7**,1427-1428.

24. **Kyotani, T., L. Tsai** and **A. Tomita** (1996). Preparation of Ultrafine Carbon Tubes in Nanochannels of an Anodic Aluminum Oxide Film. *Chem. Mater.*, **8**, 2109-2113.

25. **Kuppan, B., B. Viswanathan** and **P. Selvam** (2011) Platinum Supported Ordered Nanoporous Carbon (NCCR-41) as promising Electrocatalyst for Methanol Fuel Cell Application. *World congress on Engineering and Technology*, Shanghai, October, 28-30.

26. **Lee, J., J. Kim** and **T. Hyeon** (2006) Recent Progress in the Synthesis of Porous Carbon Materials. *Adv. Mater.*, **18**, 2073-2094.

27. **Lee, J., S. Yoon, T. Hyeon, S. M. Oh** and **K. B. Kim** (1999) Synthesis of a new mesoporous carbon and its application to electrochemical double-layer capacitors.*Chem. Commun.*, 2177- 2178.

28. **Lee, J., S. Yoon, S. M. Oh, C. H. Shin** and **T. Hyeon** (2000) Development of a New Mesoporous Carbon Using an HMS Aluminosilicate Template. *Adv. Mater.*, **12**, 359-362.

29. **Lei, Z., S. Bai, Y. Xiao, L. Dang, L. An, G. Zhang** and **Q. Xu** (2008) CMK-5 Mesoporous Carbon Synthesized via Chemical Vapor Deposition of Ferrocene as Catalyst support for Methanol Oxidation. *J. Phys. Chem. C*, **112**, 722-731.

30. **Li, X., G. Chen, J. Xie, L. Zhang, D. Xia** and **Z. Wu (2010)** An Electrocatalyst For Methanol Oxidation in DMFC-PtBi (XC-72) with Pt solid-solution structure. *J. Electrochem. Soc.*, **157**, B580-B584.

31. **Li, L.** and **Y. Xing** (2007) Pt-Ru Nanoparticles Supported on Carbon Nanotubes as Methanol Fuel Cell Catalysts. *J. Phys. Chem. C*, **111**, 2803-2808.

32. **Lei, Z., L. An, L. Dang, M. Zhao, J. Shi, S. Bai** and **Y. Cao** (2009) Highly dispersed platinum supported on nitrogen – containing ordered mesoporous carbon for methanol electrooxidation. *Microporous Mesoporous Mater.*, **119**, 30-38.

33. **Liu, Z., X. Y. Ling, J. Y. Lee, X. Su** and **L. M. Gan** (2003) Nanosized Pt and PtRu colloids as precursors for direct methanol fuel cell catalysts. *J. Mater. Chem.*, **13**, 3049-3052.

34. **Liu, B., H. Shioyama, T. Akita** and **Q. Xu** (2008) Metal-Organic Framework as a Template for Porous Carbon Synthesis. *J. Am. Chem. Soc.*,**130**, 5390-5391.

35. **Liu, H., C. Song, L. Zhang, J. Zhang, H. Wang,** and **D. P. Wilkinson** (2006). A review of anode catalysis in the direct methanol fuel cell. *J. Power Sources*,   **155**, 95-110.

36. **Liu, Z., X. Y. Ling, X. Su** and **J. Y. Lee** (2004) Carbon – supported Pt and PtRu nanoparticles as catalysts for a direct methanol fuel cell. *J. Phys. Chem. B.,* **108**, 8234-8240.

37. **Lu, A.-H,** and **F. Schuth** (2006). Nanocasting: A Versatile Strategy for Creating Nanostructured Porous Materials. *Adv. Mater.*, **18**, 1793-1805.

38. **Lu, A.-H, D. Zhao** and **Y. Wan** *Nanocasting: A Versatile Strategy for Creating Nanostructured Porous Materials*, RSC Publishing (2010).

39. **Luo, J., P. N. Njoki, Y. Lin, D. Mott, L. Wang** and **C.-J. Zhong** (2006). Characterization of Carbon –Supported AuPt Nanoparticles for Electrocatalytic Methanol Oxidation Reaction. *Langmuir*, **22**, 2892-2898.

40. **Ma, Z., T. Kyotani, Z. Liu, O. Terasaki** and **A. Tomita** (2001). Very High Surface Area Microporous Carbon with a Three-Dimensional Nano-Array Structure: Synthesis and Its Molecular Structure. *Chem. Mater.*, **13,** 4413-4415.

41. **Ma, Z., T. Kyotani** and **A. Tomita** (2000) Preparation of a high surface area microporous carbon having the structural regularity of Y Zeolite. *Chem. Commun.*, 2365–2366.

42. **Meng, Y., D. Gu, F. Zhang, Y. Shi, L .Cheng, D. Feng, Z. Wu, Z. Chen, Y. Wan, A. Stein** and **D. Zhao** (2006). A Family of Highly Ordered Mesoporous Polymer Resin and Carbon Structures from Organic-Organic Self- Assembly. *Chem. Mater.*, **18**, 4447–4464.

43. **Parsons, R.** and **T. VanderNoot** (1988) The oxidation of small organic molecules A survey of recent fuel cell related research. *J. Electroanal. Chem.*, **257**, 9-45.

44. **Pozio, A., M. De Francesco, A. Cemmi, F. Cardellini** and **L. Giorgi** (2002) Comparison of high surface Pt/C catalysts by cyclic voltammetry. *J. Power Sources*, **105**, 13–19.

45. **Ramani, V.** (2006) *The Electrochem. Soc. Interface*, 41-44.

46. **Ralph, T.R., G.A. Hards, J.E. Keating, S.A. Campbell, D.P. Wilkinson, M.Davis, J. St-Pierre** and **M.C. Johnson** (1997) Low cost electrodes for proton exchange membrane fuel cells. *J. Electrochem. Soc.*, **144**, 3845–3857.

47. **Ryoo, R., S. H. Joo** and **S. Jun** (1999) Synthesis of Highly Ordered Carbon Molecular Sieves via Template-Mediated Structural Transformation. *J. Phys. Chem. B*, **103**, 7743-7746.

48. **Rzepka, M.** and **P. Lamp** (1998). Physisorption of Hydrogen on Microporous Carbon and Carbon Nanotubes. *J. Phys. Chem. B*, **102**, 10894-10898.

49. **Solla-Gullón, J., F. J. Vidal-Iglesias, V. Montiel** and **A. Aldaz** (2004) Electrochemical characterization of platinum–ruthenium nanoparticles prepared by water-in-oil microemulsion. *Electrochimica Acta*, **49**, 5079-5088.

50. **Salgado, J. R. C., F. Alcaide, G.Álvarez, L.Calvillo, M.J. Lázaro** and **E. Pastor (2010).** Pt–Ru electrocatalysts supported on ordered mesoporous carbon for direct methanol fuel cell. *J. Power Sources*, **195**, 4022-4029.

51. **Sepa, D. B., M. V. Vojnovic** and **A. Damjanovic** (1981) Reaction intermediates as a controlling factor in the kinetics and mechanism of oxygen reduction at platinum electrodes. *Electrochim. Acta*, **26**, 781-793.

52. **Serp, P.** and **J. L. Figueiredo** *Carbon Materials for Catalysis*. A John Wiley & Sons, Inc., Publication, New York, 2009.

53. **Sidik, R. A.** and **A. B. Anderson (2002)** Density functional theory study of O_2 electroreduction when bounded to a Pt dual site. *J. Electroanal. Chem.*, **528**, 69-76.

54. **Sobkowski, J., K. Franaszczuk** and **K. Dobrowolska** (1992) Effect of anions and pH on the adsorption and oxidation of methanol on a platinum electrode. *J.Electroanal. Chem.*, **330**, 529-540.

55. **Trasatti, S.** (1971) Work fuction,electronegativity, and electrochemical behaviour of metals: II. Potentials of zero charge and electrochemical work functions. *J. Electroanal. Chem.*, **33**, 351-378.

56. **Viswanathan, B.** and **M. Aulice Scibioh** *Fuel Cell - Principles and Applications*. Universities Press (India) Private Limited, 2006.

57. **Wang, H., Q. Gao** and **J. Hu** (2009) High Hydrogen Storage Capacity of Porous Carbons Prepared by Using Activated Carbon. *J. Am. Chem. Soc.*, **131**, 7016-7022.

58. **Wang, X., B. Xu, X. Liu, J. Guo** and **H. Ichinose** (2006) Synthesis of Fe-included onion-like Fullerenes by chemical vapor deposition. *Diamond and Related Materials*, **15**, 147-150.

59. **Wang, H. J., H. Yu, F. Peng** and **P. Lv** (2006) Methanol electrocatalytic oxidation on highly dispersed Pt/sulfomated - carbon nanotube catalysts.*Electrochem. Commun.*, **8**, 499-504.

60. **Wu, G.** and **B. Q. Xu** (2007) Carbon nanotube supported Pt electrodes for methanol oxidation: A comparison between multi- and single-walled carbon nanotubes. *J. Power Sources*, **174**, 148-158.

61. **Xia, D., G. Chen, Z. Wang, J. Zhang, S (Rob). Hui, D. Ghosh** and **H. Wang** (2006) Synthesis of Ordered Intermetallic PtBi2 Nanoparticles for Methanol-Tolerant Catalyst in Oxygen Electroreduction. *Chem. Mater.*, **18**, 5746-5749.

62. **Xia, Y., Z. Yang** and **R. Mokaya** (2010) Templated nanoscale porous carbons. *Nanoscale*, **2**, 639-659.

63. **Xiong, L.** and **A. Manthiram** (2005) Catalytic activity of Pt–Ru alloys synthesized by a microemulsion method in direct methanol fuel cells. *Solid State Ionics*, **176**, 385-392.

64. **Xu, B., X. Yang, X. Wang, J. Guo** and **X. Liu** (2006) A novel catalyst support for DMFC: Onion-like fullerenes. *J. Power Sources*, **162**, 160-164.

65. **Xue, X., T. Lu, C. Liu** and **W. Xing** (2005) Simple and controllable synthesis of highly dispersed Pt-Ru/C catalysts by a two-step spray pyrolysis process. *Chem. Commun.*, 1601-1603.

66. **Yuan, D.S., J. Zeng, J. Chen** and **Y. Liu** (2009) Highly Ordered Mesoporous Carbon Synthesized via in situ Template for Supercapacitors. *Int. J. Electrochem. Sci.*, **4**, 562-570.

67. **Zeng, J., F. Su, J.Y. Lee, X. S. Zhao, J. Chen** and **X. Jiang** (2007) Method for preparing highly dispersed Pt catalysts on mesoporous carbon support. *J. Materials Sci.*, **42**, 7191-7197.